Journal of Nanotechnology

Nanomaterials for Energy Production and Storage

Guest Editors: Vaishali R. Shinde, Won Bae Kim, Shrikrishna D. Sartale, and Tanaji P. Gujar

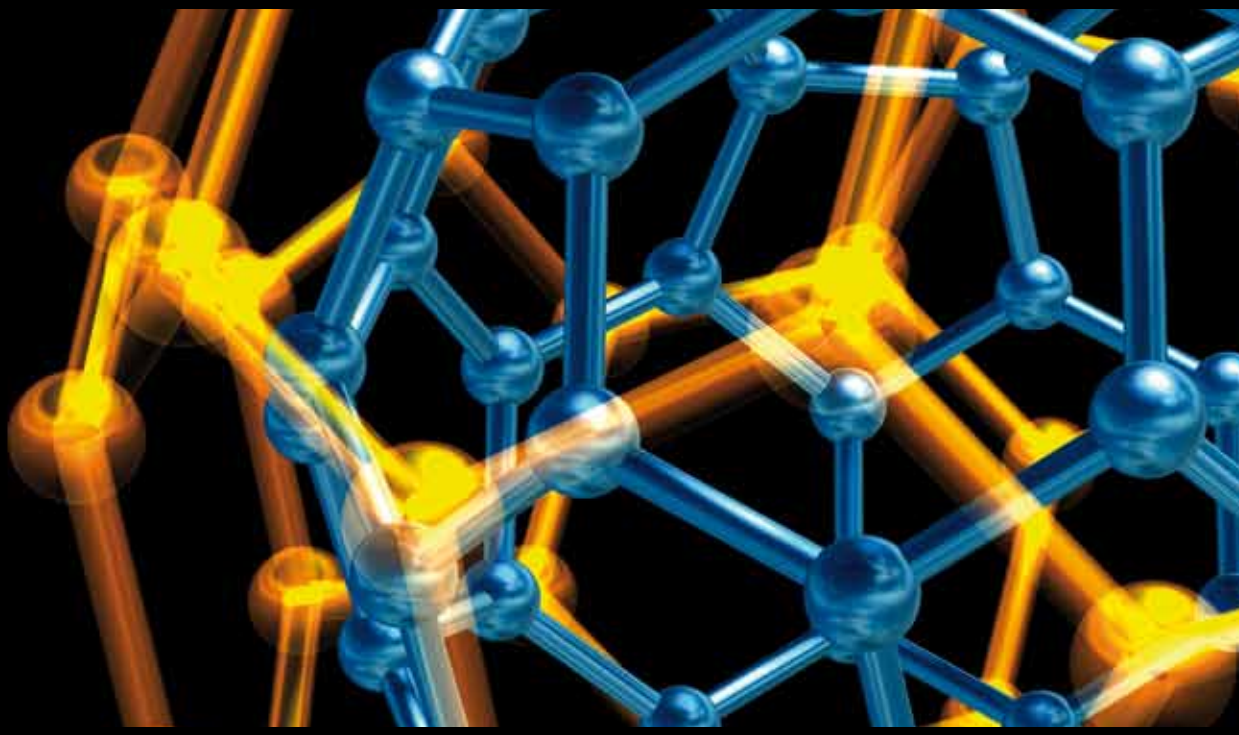

Nanomaterials for Energy Production and Storage

Journal of Nanotechnology

Nanomaterials for Energy Production and Storage

Guest Editors: Vaishali R. Shinde, Won Bae Kim, Shrikrishna D. Sartale, and Tanaji P. Gujar

Copyright © 2012 Hindawi Publishing Corporation. All rights reserved.

This is a special issue published in "Journal of Nanotechnology." All articles are open access articles distributed under the Creative Commons Attribution License, which permits unrestricted use, distribution, and reproduction in any medium, provided the original work is properly cited.

Editorial Board

Simon Joseph Antony, UK
Yoshio Bando, Japan
B. Bhushan, USA
Felix A. Buot, USA
Carlos R. Cabrera, Puerto Rico
John A. Capobianco, Canada
Franco Cerrina, USA
Gan Moog Chow, Singapore
Jeffery L. Coffer, USA
Dmitriy A. Dikin, USA
Dimitris Drikakis, UK
H. D. Espinosa, USA
John S. Foord, UK
E. Goldys, Australia
Lambertus Hesselink, USA
Joseph Irudayaraj, USA
Niraj K. Jha, USA
Miguel Jose-Yacaman, USA
Valery Khabashesku, USA
Yoke Khin Yap, USA
Sakhrat Khizroev, USA
Andrei Kolmakov, USA
Charles M. Lieber, USA
Charles M. Lukehart, USA
A. Salam H. Makhlouf, Germany
Constantinos Mavroidis, USA
Vincent Meunier, USA
Paolo Milani, Italy
Oded Millo, Israel
Oussama Moutanabbir, Canada
M. Grant Norton, USA
R. Lee Penn, USA
S. N. Piramanayagam, Singapore
A. M. Rao, USA
Paresh Chandra Ray, USA
Benjaram M. Reddy, India
Federico Rosei, Canada
Mehmet Sarikaya, USA
Jorge M. Seminario, USA
V. Shalaev, USA
Mahi R. Singh, Canada
Bobby G. Sumpter, USA
Xiao Wei Sun, Singapore
Weihong Tan, USA
O. K. Tan, Singapore
Thomas Thundat, USA
Boris I. Yakobson, USA
Nan Yao, USA
Chuan Jian Zhong, USA

Contents

Nanomaterials for Energy Production and Storage, Vaishali R. Shinde, Won Bae Kim, Shrikrishna D. Sartale, and Tanaji P. Gujar
Volume 2012, Article ID 696310, 2 pages

Catalytic Chemical Vapor Deposition Synthesis of Carbon Aerogels of High-Surface Area and Porosity, Armando Peña, Julio Puerta, Aimé Guerrero, Edgar Cañizales, and Joaquín L. Brito
Volume 2012, Article ID 708626, 5 pages

Highly Stable and Active Pt/Nb-TiO_2 Carbon-Free Electrocatalyst for Proton Exchange Membrane Fuel Cells, Shuhui Sun, Gaixia Zhang, Xueliang Sun, Mei Cai, and Martin Ruthkosky
Volume 2012, Article ID 389505, 8 pages

Titanium as a Potential Addition for High-Capacity Hydrogen Storage Medium, Filippo Zuliani, Leonardo Bernasconi, and Evert Jan Baerends
Volume 2012, Article ID 831872, 9 pages

Reforming of Ethanol to Produce Hydrogen over PtRuMg/ZrO_2 Catalyst, Josh Y. Z. Chiou, Chi-Han Wang, Shih-Yi Yang, Jia-Lin Bi, Chia-Chieh Shen, and Chen-Bin Wang
Volume 2012, Article ID 573287, 6 pages

Nanotechnology Role for the Production of Clean Fuel E-85 and Petrochemical Raw Materials, Iskander K. Basily, Amira L. Shafik, Ali A. Sarhan, and Mona B. Mohamed
Volume 2012, Article ID 439531, 5 pages

Two-Electron Reaction without Structural Phase Transition in Nanoporous Cathode Material, Tomoyuki Matsuda and Yutaka Moritomo
Volume 2012, Article ID 568147, 8 pages

Hindawi Publishing Corporation
Journal of Nanotechnology
Volume 2012, Article ID 696310, 2 pages
doi:10.1155/2012/696310

Editorial

Nanomaterials for Energy Production and Storage

Vaishali R. Shinde,[1] Won Bae Kim,[2] Shrikrishna D. Sartale,[3] and Tanaji P. Gujar[4]

[1] *International Center for Young Scientists (ICYS), National Institute for Materials Science (NIMS), 1-2-1 Sengen, Ibaraki, Tsukuba 305-0047, Japan*
[2] *Advanced Materials Research Laboratory, School of Materials Science and Engineering, Gwangju Institute of Science and Technology, (GIST), Gwangju 500-712, Republic of Korea*
[3] *Department of Physics, University of Pune, Pune 411 007, India*
[4] *Department of Physics and Institute for Functional Nanomaterials, University of Puerto Rico, San Juan, PR 00931-3343, USA*

Correspondence should be addressed to Vaishali R. Shinde, shinde_vr2003@yahoo.com

Received 17 December 2012; Accepted 17 December 2012

Copyright © 2012 Vaishali R. Shinde et al. This is an open access article distributed under the Creative Commons Attribution License, which permits unrestricted use, distribution, and reproduction in any medium, provided the original work is properly cited.

With the increasing world population and burst of portable electronic devices, automobile and other industries, the consumption of energy in many forms has been intensively escalated. However, the world energy sources are being consumed fast and this has put the world in a ditch of energy crisis. On the other hand, the availability of sustainable energy is crucial for the economic growth and industrialization, thus, sufficient and inexpensive energy is the most important demand of today. So this is the time to conserve the nonrenewable energy sources as well as to find the alternative sources of energy production and storage. In response to the needs of modern society and emerging ecological concerns, the new, low-cost, and environmentally friendly energy conversion and storage systems should be investigated, and research and development of this field should be rapidly accelerated. Nanomaterials, with tailored characteristics at the nanometer scale, offer unique properties or combinations of properties and will play a vital role in the development of new energy technologies for energy production and storage.

In this special issue, we have selected out of received the relevant research articles and covered the broad field from worldwide scientists. In this issue we publish several research articles that are addressing these fields.

S. Sun et al. have introduced a carbon-free electrocatalyst based on Pt/Nb-TiO_2 for proton exchange membrane fuel cells (PEMFC) applications, where a facile surfactant-free wet-chemical method was used to grow single-crystalline Pt nanoparticles (NP) on mesoporous Nb-doped TiO_2 hollow spheres in aqueous solution. The use of Nb-TiO_2 hollow spheres as substrate has been proved to provide a new type of cost-effective support with high corrosion resistance for Pt-NP. Interestingly, the growth of Pt-NP on Nb-TiO_2 support could be controlled by manipulating the mass ratios between the Pt precursor and the Nb-TiO_2 support. The Pt-NP/Nb-TiO_2 catalysts have been demonstrated to enhance activity and stability compared with the commercial E-TEK Pt/C catalyst.

I. K. Basily et al. have presented a role of nanotechnology for the production of clean fuel E-85 and petrochemical raw materials. The aim of this experiment was to obtain unsaturated hydrocarbons from petroleum residues with the help of different types of nanocatalyst and to optimize the pyrolysis parameters of the two-stage reactor. The studies on the effectiveness of catalysts such as CaO and gold nanocatalyst supported on CaO for the yield and product distribution have been carried out. In this work it has been concluded that the Au nanocatalyst with rods shape gives the maximum yield of ethylene (which can be converted easily to ethyl alcohols which is used as E-85 clean fuel) from petroleum residues.

Li-ion batteries are one of the efficient energy storage devices that have established a strong market position especially for portable electronic devices. In this context, T. Matsuda and Y. Moritomo have demonstrated two-electron-reaction without structural phase transition in nanoporous cathode material. They have studied the charge/discharge properties, valence states, and structural properties of a nanoporous cathode material $Li_xMn[Fe(CN)_6]_{0.83} \cdot 3.5H_2O$. Thin film of $Li_xMn[Fe(CN)_6]_{0.83} \cdot 3.5H_2O$ was obtained by

substitution of Na from $Na_{1.32}Mn[Fe(CN)_6]_{0.83} \cdot 3.5H_2O$ which was synthesized electrochemically on an indium tin oxide (ITO) transparent electrode. From the presented data it was clearly illustrated that the two-electron reaction without structural phase transition is responsible for the high charge capacity and the good cyclability observed in $Li_xMn[Fe(CN)_6]_{0.83} \cdot 3.5H_2O$.

J. Y. Z. Chiou et al. have presented hydrogen production by reforming of ethanol over the $PtRuMg/ZrO_2$ catalyst. They have modified the $PtRu/ZrO_2$ catalyst with Mg and studied the oxidative steam reforming of ethanol (OSRE) and the steam reforming of ethanol (SRE) to realize the hydrogen production at a temperature lower than 300°C with higher ethanol conversion, hydrogen yield, and lower CO distribution. The results show that the OSRE reaction requires a higher temperature (~390°C) to achieve 100% ethanol conversion than the SRE reaction (~250°C). They have concluded that $PtRuMg/ZrO_2$ catalyst is suitable for SRE reaction considering the catalytic stability against the coke deposition.

Carbon aerogels, the nanostructured porous materials with reasonable high surface area and electric conductivity, are the potential candidate for electrochemical energy storage. A. Peña et al. have presented synthesis of carbon aerogels by catalytic chemical vapor deposition method (CCVD) using ferrocene as a source both of catalytic material (Fe) and of carbon. Using the CCVD method they have obtained carbon aerogels with surface areas and pore volumes of 780 m^2/g (SBET) and of 0.55 cm^3/g (VBJH), respectively. According to their analysis, the large surface area is due to mesopores formed by the aggregation of carbon nanostructures. These porous Carbon aerogels present the promising features for applications in the physisorption of gases, for example, in the storage of molecular hydrogen for fuel cell applications.

Whilst storage of hydrogen is an important issue, the titanium decorated with organic compounds offers promising features for high-capacity hydrogen storage. F. Zuliani et al. have studied the adsorption of hydrogen molecules on a titanium atom supported by a benzene molecule using generalized gradient corrected Density Functional Theory (DFT) and elucidated the catalytic role of the Ti atom in the dissociation of the H_2 molecule. The authors have analyzed the orbital interactions responsible for the H_2 binding to Ti and for the dissociation of one H_2 molecule. Their results reveal that up to four H_2 molecules can coordinate to the metal ion center, with adsorption patterns similar to those observed in Ti-SWNTs and no more than one molecule dissociating in the process. With the detail studies and observation they have proposed Ti on carbon supports as a new and efficient material for hydrogen storage.

Vaishali R. Shinde
Won Bae Kim
Shrikrishna D. Sartale
Tanaji P. Gujar

Hindawi Publishing Corporation
Journal of Nanotechnology
Volume 2012, Article ID 708626, 5 pages
doi:10.1155/2012/708626

Research Article

Catalytic Chemical Vapor Deposition Synthesis of Carbon Aerogels of High-Surface Area and Porosity

Armando Peña,[1] Julio Puerta,[1,2] Aimé Guerrero,[3] Edgar Cañizales,[4] and Joaquín L. Brito[5]

[1] *Laboratorio de Física de Plasma y Nanotecnología, Universidad Simón Bolívar, Apartado 89000, Caracas 1080, Venezuela*
[2] *Departamento de Física, Universidad Simón Bolívar, Apartado 89000, Caracas 1080, Venezuela*
[3] *Departamento de Ciencias de los Materiales, Universidad Simón Bolívar, Apartado 89000, Caracas 1080, Venezuela*
[4] *PDVSA-Intevep, Los Teques, Apartado 76343, Caracas 1070-A, Venezuela*
[5] *Centro de Química, Instituto Venezolano de Investigaciones Científicas, Apartado 20632, Caracas 1020, Venezuela*

Correspondence should be addressed to Julio Puerta, jpuerta@usb.ve

Received 16 March 2012; Revised 28 August 2012; Accepted 28 August 2012

Academic Editor: Tanaji P. Gujar

Copyright © 2012 Armando Peña et al. This is an open access article distributed under the Creative Commons Attribution License, which permits unrestricted use, distribution, and reproduction in any medium, provided the original work is properly cited.

In this work carbon aerogels were synthesized by catalytic chemical vapor deposition method (CCVD). Ferrocene were employed as a source both of catalytic material (Fe) and of carbon. Gaseous hydrogen and argon were used as reductant and carrier gas, respectively. The products of reaction were collected over alumina. The morphology and textural properties of the soot produced in the reaction chamber were investigated using Scanning Electron Microscopy, High-Resolution Transmission Electron Microscopy, X-ray photoelectron spectroscopy, and N_2 physisorption (BET and BHJ methods). After the evaluation of the porous structure of the synthesized products, $780 \pm 20\ m^2/g$ of S_{BET} and $0.55 \pm 0.02\ cm^3/g$ of V_{BJH} were found. The presence of iron carbide and the partial oxidation of carbon nanostructures were revealed by XPS.

1. Introduction

The fabrication of carbon nanostructures with characteristic morphologies will determine further applications such as field emitters, gas storage (H_2 for fuel cells), sensors, and biosensors, and so forth [1]. The high capacity of adsorption, chemical inertia, and the easy regenerability that have the carbon nanostructures make them potential useful adsorbents [2].

Carbon aerogels are nanostructured porous materials consisting in a network of carbonaceous particles of uniform nanosized dimensions, with superficial areas that commonly are found between 400 and $1100\ m^2/g$ and an electric conductivity of approximately 1000 A/cm. They are highly demanded in scientific technology: the most important applications of these carbonaceous structures are as electrodes and supercapacitors, where they serve as support for metal nanoparticles [3, 4].

Carbon aerogels are usually synthesized by high-temperature pyrolysis of organic aerogels, which in turn are prepared by polymerization of two monomers (e.g., resorcinol-formaldehyde) using sol-gel methods and processing the resulting material under supercritical conditions [5, 6]. This type of synthesis involves several steps under very diverse conditions. Thus, a simpler preparation way would be an important advance in the synthesis of this kind of materials. Chemical Vapor Deposition (CVD) from hydrocarbon gaseous compounds or carbon monoxide is a relatively simple synthesis method that has been employed for the growth of carbon nanostructures [7]. When using metallic nanoparticles as catalytic sites for the growth of such carbon nanomaterials, it has been described as Catalytic CVD (CCVD) [8]. In particular, it has been proposed as a method for growing carbon nanotubes and filaments within the porous structure of conventionally prepared carbon aerogels [9, 10].

In this context, the objective of this work is to apply the technique of CCVD, employing a single organometallic compound, ferrocene [$Fe(C_5H_5)_2$], as source of both the catalyst and of carbon and a continuous flow reaction system with two separated heating zones.

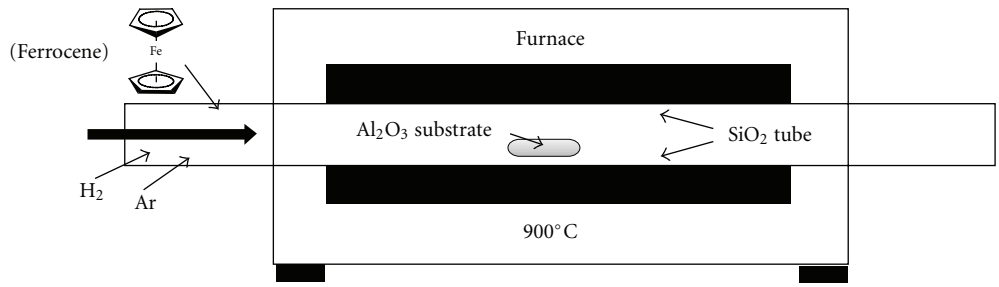

Figure 1: CVD reactor scheme employed the synthesis of the carbon aerogels.

2. Experimental Setup

In order to synthesize the aerogels, ferrocene was used as a simultaneous source of catalytic material (Fe) and filler material (C). Gaseous hydrogen was employed as reductant, while argon was an inert carrier gas. The reaction products were collected onto either alumina or silica substrates.

A reaction chamber similar to that described previously [11] was employed. The ferrocene was sublimated in a preheating chamber, which temperature was set at 150°C and was transported to the cracking reactor by a flow of H_2 and Ar. In total, 150 mg of ferrocene was evaporated, in two consecutive steps of 100 mg and 50 mg, with 10 min in between. The pyrolysis temperature in the cracking furnace was 900°C, and the total gas flow was 10 mL/min with a composition of 1 : 1 v/v of Ar : H_2.

In order to eliminate Fe from the products, concentrated HCl and sonication were used. The resulting materials were characterized using Scanning Electronic Microscopy (SEM) with a JEOL scanning microscope, model JSM-6390, 30 KV; High Resolution Transmission Electronic Microscopy (HRTEM) with a JEOL transmission microscopy, model JEM-2100, 200 KV; X-ray Photoelectron Spectroscopy (XPS) with a Thermo Scientific VG-Escalab 220i-XL; N_2 physisorption with a Micrometrics Surface Analyzer, model ASAP 2000, using the BET and BJH methods for the textural analysis. In Figure 1 a schematic drawing of the CVD homemade reactor and experimental conditions is presented.

3. Results and Discussion

In Figure 2(a), three SEM micrographies of the synthesized carbon aerogel at different magnifications are shown, in which a network of carbon nanotubes and nanospheres can be observed. At the lower magnification, nanotubes foam clusters deposited on a SiO_2 substrate can be observed, while in the 5000x and 10000x micrographies the network of carbon nanotubes coated with nanospheres of carbon nanoparticles is clearly appreciated. The composition of these structures was determined by means of a chemical analysis by EDX in the same microscope, finding only C, Fe and O in weight percentages of 72.10; 26.84; 1.06%, respectively (see Figure 2(b)). The presence of oxygen could be attributed to surface oxidation of Fe nanoparticles due to exposition to the atmosphere when samples are removed from the CVD reactor. Carbon aerogel grew evenly across the surface of SiO_2.

In Figure 3, four HRTEM micrographies of the synthesized carbon aerogel are shown in which it can be seen a network of carbonaceous structures, such as nanotubes and nanospheres (see micrographs (a) and (b)). In the micrographs (c) and (d), consecutive increases of (b) are shown, where it can be seen on average 40 nm diameter carbon nanospheres.

XPS tests revealed the presence of iron carbide and partial oxidation of carbon nanostructures. XPS spectra of carbon aerogels in the C 1*s* and Fe *2p* regions are presented in Figures 4(a) and 4(b), respectively. In the first one, we see three peaks with binding energies (BEs) of 286, 284, and 280 eV, corresponding to the *sp*3 C–C bonds of tetrahedral structures, C–C *sp*2 of graphitic structures, and Fe_3C, respectively [12–14]. The peak of iron carbide is displaced to a lower BE as compared to other reports (283 eV [13, 15]), this large shift of about 3 eV can be attributed to interactions with the magnetic field of nanoparticles of Fe or inefficient electrical connection that may exist between Fe and C atoms [14, 16]. A fourth peak that appears around 278 eV in the C 1*s* region, which is denoted by the symbol ψ, can be attributed to the fullerene carbon filaments [17].

In the Fe $2p$ region there are three peaks with BEs of 712, 720, and 726 eV. The 712 and 726 signals correspond to the $2p_{3/2}$ and $2p_{1/2}$ Fe^{3+} species, respectively, while the intermediate signal is due to a satellite of the same species [18].

In Figure 5, the N_2 adsorption isotherm at 77 K of the synthesized carbon aerogel can be observed. It is of type IV in the IUPAC/Brunauer-Emmett-Teller classifications, typical of mesoporous materials [19]. Given the very low increase of physisorbed volume below P/P_0 0.05, it can be deduced that the microporous volume is negligible in this sample. In the high-pressure region it appears a H_3 hysteresis loop at a relative pressure higher than 0.8. This indicates the existence of extraparticle large mesopores which could be formed between interconnected carbon nanoparticles [20]. After evaluating the pore structure of synthesized products by BET and BJH procedures, it is found a BET surface area, S_{BET}, of $780 \pm 20\,m^2/g$ and BJH pore volume, V_{BJH}, of $0.55 \pm 0.02\,cm^3/g$. The measured surface area is quite large for a non-microporous material.

Ferrocene has been frequently employed as a precursor of iron catalysts for the CVD synthesis of carbon nanotubes

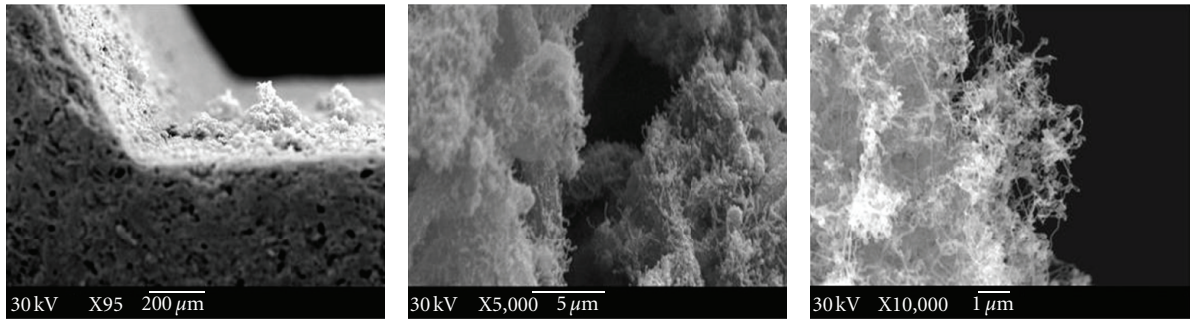

(a)

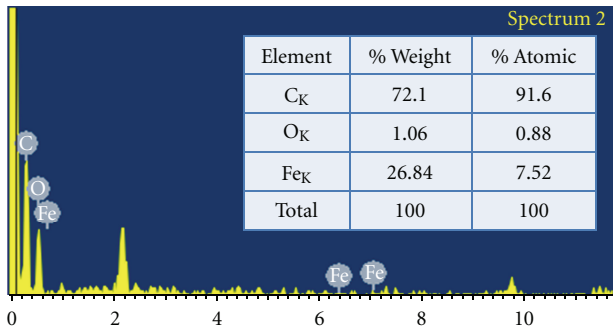

Element	% Weight	% Atomic
C_K	72.1	91.6
O_K	1.06	0.88
Fe_K	26.84	7.52
Total	100	100

Full scale 110 cts cursor: 0.084 (1020 cts)

(b)

Figure 2: (a) SEM micrographies of carbon aerogels on SiO_2, at 95x, 5000x, and 10000x. (b) EDX spectrum of carbon aerogels. K_α characteristics peaks are observed for C, O, and Fe.

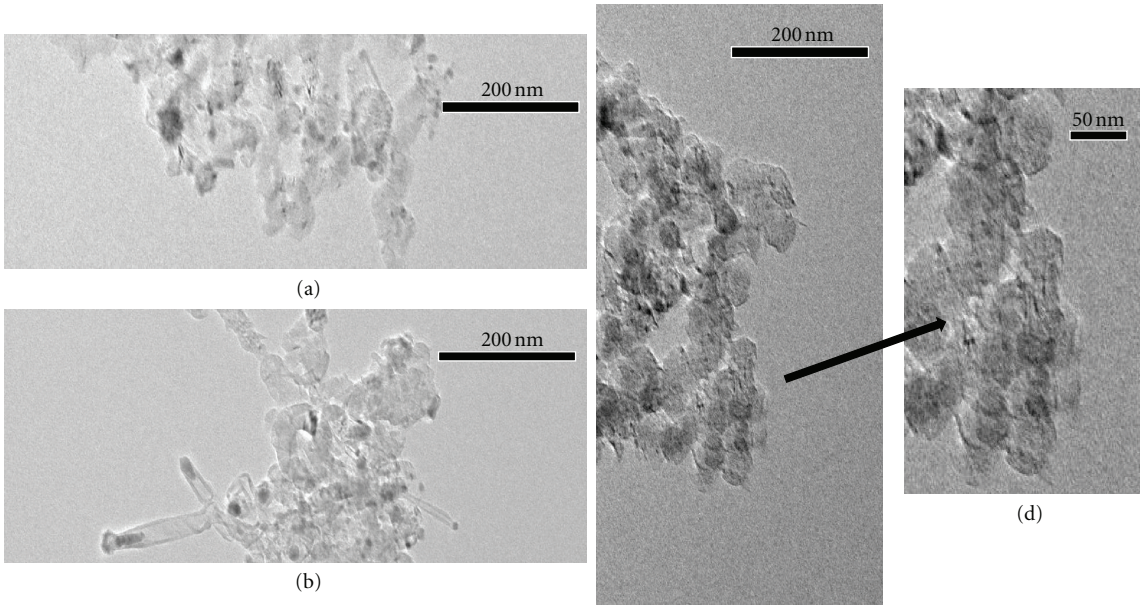

(a)

(b)

(c)

(d)

Figure 3: HRTEM micrographs of carbon aerogels. The displayed scale bars are (a, b, c) 200 nm and (d) 50 nm.

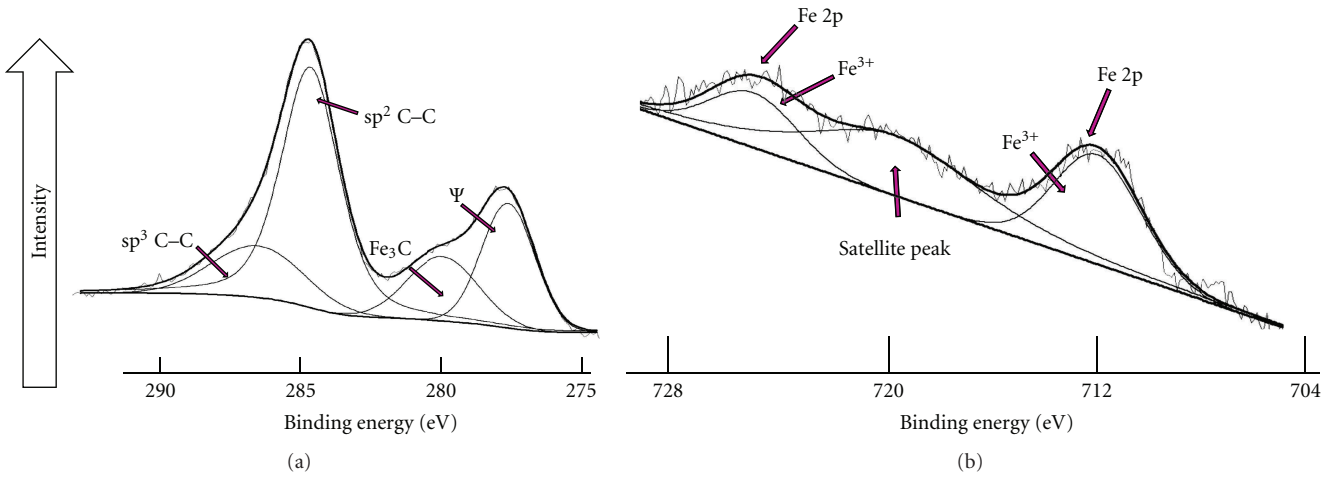

Figure 4: XPS spectra of carbon aerogels: (a) C 1*s* region, and (b) Fe *2p* region.

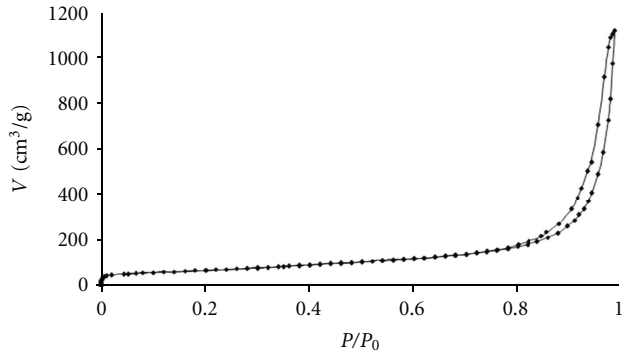

Figure 5: N_2 adsorption isotherm type IV (77 K) of Carbon Aerogels.

[21, 22], normally used as carbon source organic gases or vapors (hydrocarbons, alcohols, etc.). It has been much less employed for carbon nanotube preparation as the sole source of catalyst and carbon [23]. In the present work it is proposed a simple CCVD methodology for the synthesis of carbon aerogels uses ferrocene as source of both Fe catalyst and of carbon filler material. The proposed method is simpler than the usually employed synthesis through organic aerogels, which involves several steps under conditions varying in an ample range. A key procedure in the methodology reported is the division in two consecutive steps of the evaporation of the ferrocene, with a short time in between the two evaporation steps. This way, a two-phase system is generated, with imperfections in carbon nanotubes, which couple with nanocapsules of carbon nanotubes produced in the second step, finally leading to the carbon aerogels.

4. Conclusions

Using the CCVD method and ferrocene as the starting material, carbon aerogels with surface areas and pore volumes of $780 \pm 20\,m^2/g$ (S_{BET}) and of $0.55 \pm 0.02\,cm^3/g$ (V_{BJH}), respectively, are obtained. The large surface area is not due to microspores but to mesopores formed by the aggregation of carbon nanostructures. These porous properties are promising features for applications in the physisorption of gases, for example, in the storage of molecular hydrogen for fuel cell applications. The XPS tests revealed the presence of iron carbide and the partial oxidation of carbon nanostructures.

Acknowledgments

The authors thank PDVSA-INTEVEP for HRTEM assays, Surface Physicochemistry Laboratory at IVIC for XPS measurements, and Carbon Laboratory at USB for N_2 physisorption measurements.

References

[1] D. Mann, "Synthesis of carbon nanotubes," in *Carbon Nanotubes: Properties and Applications*, M. J. O'Connell, Ed., Taylor & Francis, Boca Raton, Fla, USA, 2006.

[2] F. Hennrich, C. Chan, V. Moore, M. Rolandi, and M. O'Connell, "The element carbon," in *Carbon Nanotubes Properties and Applications*, M. J. O'Connell, Ed., Taylor & Francis, Boca Raton, Fla, USA, 2006.

[3] C. J. Gabelich, T. D. Tran, and I. H. Suffet, "Electrosorption of inorganic salts from aqueous solution using carbon aerogels," *Environmental Science and Technology*, vol. 36, no. 13, pp. 3010–3019, 2002.

[4] J. M. Miller and B. Dunn, "Morphology and electrochemistry of ruthenium/carbon aerogel nanostructures," *Langmuir*, vol. 15, no. 3, pp. 799–806, 1999.

[5] H. Y. Tian, C. E. Buckley, S. Mulè, M. Paskevicius, and B. B. Dhal, "Preparation, microstructure and hydrogen sorption properties of nanoporous carbon aerogels under ambient drying," *Nanotechnology*, vol. 19, no. 47, Article ID 475605, 2008.

[6] A. M. Shariff, D. M. Beshir, M. A. Bustam, and S. Maitra, "Some studies on the synthesis and characterization of carbon aerogel," *Transactions of the Indian Ceramic Society*, vol. 69, no. 2, pp. 1–4, 2010.

[7] M. Kumar and Y. Ando, "Chemical vapor deposition of carbon nanotubes: a review on growth mechanism and mass production," *Journal of Nanoscience and Nanotechnology*, vol. 10, no. 6, pp. 3739–3758, 2010.

[8] Ç. Öncel and Y. Yürüm, "Carbon nanotube synthesis via the catalytic CVD method: a review on the effect of reaction parameters," *Fullerenes Nanotubes and Carbon Nanostructures*, vol. 14, no. 1, pp. 17–37, 2006.

[9] R. Fu, M. S. Dresselhaus, G. Dresselhaus et al., "The growth of carbon nanostructures on cobalt-doped carbon aerogels," *Journal of Non-Crystalline Solids*, vol. 318, no. 3, pp. 223–232, 2003.

[10] S. A. Steiner III, T. F. Baumann, J. Kong, J. H. Satcher Jr, and M. S. Dresselhaus, "Iron-doped carbon aerogels: novel porous substrates for direct growth of carbon nanotubes," *Langmuir*, vol. 23, no. 9, pp. 5161–5166, 2007.

[11] S. Huang, L. Dai, and A. W. H. Mau, "Patterned growth and contact transfer of well-aligned carbon nanotube films," *Journal of Physical Chemistry B*, vol. 103, no. 21, pp. 4223–4227, 1999.

[12] Y. M. Shulga, T. C. Tien, C. C. Huang et al., "XPS study of fluorinated carbon multi-walled nanotubes," *Journal of Electron Spectroscopy and Related Phenomena*, vol. 160, no. 1–3, pp. 22–28, 2007.

[13] K. Y. Yang, X. Wei, Y. Zheng, W. T. Zhang, and X. Wang, "Synthesis and characteristics of Fe_3C nanoparticles embedded in amorphous carbon matrix," *Chemical Research in Chinese Universities*, vol. 26, no. 3, pp. 348–351, 2010.

[14] K. Y. Chun, S. K. Choi, H. J. Kang, C. Y. Park, and C. J. Lee, "Highly dispersed multi-walled carbon nanotubes in ethanol using potassium doping," *Carbon*, vol. 44, no. 8, pp. 1491–1495, 2006.

[15] http://www.lasurface.com/, 2012.

[16] Y. Sun, X. Ding, Z. Zheng, X. Cheng, X. Hu, and Y. Peng, "Magnetic separation of polymer hybrid iron oxide nanoparticles triggered by temperature," *Chemical Communications*, no. 26, pp. 2765–2767, 2006.

[17] V. C. H. Kroll, P. Delichure, and C. Mirodatos, "Methane reforming reaction with carbon dioxide over a Ni/SiO_2 catalyst: the nature of the active phase," *Kinetics and Catalysis*, vol. 37, no. 5, pp. 698–705, 1996.

[18] A. De Stefanis, S. Kaciulis, and L. Pandolfi, "Preparation and characterization of Fe-MCM-41 catalysts employed in the degradation of plastic materials," *Microporous and Mesoporous Materials*, vol. 99, no. 1-2, pp. 140–148, 2007.

[19] S. J. Gregg and K. S. W. Sing, "The physical adsorption of gases by mesoporous solids: the type IV isoteherm," in *Adsorption, Surface Area and Porosity*, SegundaEdición, Madrid, Spain, Academic Press, New York, NY, USA, 1982.

[20] Q. H. Yang, P. X. Hou, S. Bai, M. Z. Wang, and H. M. Cheng, "Adsorption and capillarity of nitrogen in aggregated multi-walled carbon nanotubes," *Chemical Physics Letters*, vol. 345, no. 1-2, pp. 18–24, 2001.

[21] H. W. Zhu, C. L. Xu, D. H. Wu, B. Q. Wei, R. Vajtai, and P. M. Ajayan, "Direct synthesis of long single-walled carbon nanotube strands," *Science*, vol. 296, no. 5569, pp. 884–886, 2002.

[22] A. Moisala, A. G. Nasibulin, D. P. Brown, H. Jiang, L. Khriachtchev, and E. I. Kauppinen, "Single-walled carbon nanotube synthesis using ferrocene and iron pentacarbonyl in a laminar flow reactor," *Chemical Engineering Science*, vol. 61, no. 13, pp. 4393–4402, 2006.

[23] A. Barreiro, S. Hampel, M. H. Rümmeli et al., "Thermal decomposition of ferrocene as a method for production of single-walled carbon nanotubes without additional carbon sources," *Journal of Physical Chemistry B*, vol. 110, no. 42, pp. 20973–20977, 2006.

Hindawi Publishing Corporation
Journal of Nanotechnology
Volume 2012, Article ID 389505, 8 pages
doi:10.1155/2012/389505

Research Article

Highly Stable and Active Pt/Nb-TiO_2 Carbon-Free Electrocatalyst for Proton Exchange Membrane Fuel Cells

Shuhui Sun,[1,2,3] Gaixia Zhang,[1,2,3] Xueliang Sun,[2] Mei Cai,[1] and Martin Ruthkosky[1]

[1] *General Motors Global Research and Development Center, Warren, MI 48090-9055, USA*
[2] *Department of Mechanical and Materials Engineering, The University of Western Ontario, London, ON, Canada N6A 5B9*
[3] *Institut National de la Recherche Scientifique-Énergie, Matériaux et Télécommunications, Université du Québec, Varennes, QC, Canada J3X 1S2*

Correspondence should be addressed to Xueliang Sun, xsun@eng.uwo.ca and Mei Cai, mei.cai@gm.com

Received 13 March 2012; Accepted 30 May 2012

Academic Editor: Tanaji P. Gujar

Copyright © 2012 Shuhui Sun et al. This is an open access article distributed under the Creative Commons Attribution License, which permits unrestricted use, distribution, and reproduction in any medium, provided the original work is properly cited.

The current materials used in proton exchange membrane fuel cells (PEMFCs) are not sufficiently durable for commercial deployment. One of the major challenges lies in the development of an inexpensive, efficient, and highly durable and active electrocatalyst. Here a new type of carbon-free Pt/Nb-TiO_2 electrocatalyst has been reported. Mesoporous Nb-TiO_2 hollow spheres were synthesized by the sol-gel method using polystyrene (PS) sphere templates. Pt nanoparticles (NPs) were then deposited onto mesoporous Nb-TiO_2 hollow spheres via a simple wet-chemical route in aqueous solution, without the need for surfactants or potentiostats. The growth densities of Pt NPs on Nb-TiO_2 supports could be easily modulated by simply adjusting the experimental parameters. Electrochemical studies of Pt/Nb-TiO_2 show much enhanced activity and stability than commercial E-TEK Pt/C catalyst. PtNP/Nb-TiO_2 is a promising new cathode catalyst for PEMFC applications.

1. Introduction

Proton exchange membrane fuel cells (PEMFCs) have been attracting much attention as an alternative clean energy source because of their high efficiency, high power density, and low pollution [1]. However, there are still challenges, such as, low catalytic activity, low durability, and high cost, which are hindering the commercialization of PEMFCs [2]. For automotive applications, PEMFCs must be durable enough for ~5,000 driving hours (i.e., 10 years) in vehicles [2]. The loss of platinum (Pt) electrochemical surface area (ECSA) over time due to carbon support corrosion and Pt dissolution/aggregation/Oswald ripening is considered one of the major contributors to the degradation of fuel cell performance [3]. Usually, carbon black (Vulcan XC-72) is used as Pt catalyst support in PEMFCs. However, carbon black is known to undergo electrochemical oxidation under a fuel cell operating environment, especially at potentials above 0.9 V (1), leading to a loss of Pt and fuel cell performance degradation [4, 5]:

$$C + 2H_2O \longrightarrow CO_2 + 4H^+ + 4e^-. \quad (1)$$

Therefore, it is necessary to explore noncarbon catalyst support materials with the current fuel cell operating strategy. Some metal oxides have been studied by different research groups as alternative catalyst support materials, such as, substoichiometric titanium oxide [6, 7], indium tin oxide [8], niobium-doped titania [9], tungsten oxide [10, 11], and tin oxide [12]. Among these, niobium-doped titania (Nb-TiO_2) [9, 13–15] is a particularly promising candidate. TiO_2 is notable for its photocatalytic and strong metal support interaction (SMSI) properties [16, 17]. TiO_2 is also readily available, cheap, and nontoxic [18]. The use of Nb doping has been found to significantly improve the electrical conductivity of TiO_2, which allows its use in electrocatalytic reactions [14]. In this study, we present a simple wet-chemical route to

grow Pt nanoparticles (NPs) on mesoporous Nb-TiO_2 hollow spheres, with controlled Pt loadings, in environmentally friendly aqueous solution. PtNPs/Nb-TiO_2 catalysts exhibit higher catalytic activity for ORR and better stability than the benchmark E-TEK commercial Pt/C catalysts.

2. Materials and Methods

2.1. Chemicals. Hexadecyltrimethylammoniumbromide (HATB), titanium (IV) isopropoxide (TTIP), niobium (V) ethoxide (8 mol %), ethanol, HNO_3, hexachloroplatinic acid ($H_2PtCl_6 \cdot 6H_2O$, 99.95%), and formic acid (HCOOH, 98%) were purchased from Sigma-Aldrich. Aqueous latex (mean diameter 200 nm) suspension (10 wt%) was purchased from Duke Scientific. All chemicals were used as received without further purifications. All solutions were prepared with ultrapure water purified with the Millipore water system (18.2 MΩ·cm resistivity @25°C).

2.2. Preparation of Mesostructured Nb-TiO_2 Support. The mesostructured Nb-TiO_2 support was prepared according to the method described in [15]. Briefly, 0.015 g of HATB, 14.7 mL of aqueous latex suspension, and 105 mL of ethanol were added in a PTFE beaker, and then the solution was stirred vigorously for 30 min while HNO_3 was added to adjust the pH to 3. A second solution was prepared by adding the precursors, 6.9 mL of TTIP and 0.5 mL niobium (V) ethoxide to 100 mL of ethanol. The second solution was added to the stirred latex-surfactant mixture using a peristaltic pump at a rate of 1 mL/min. The resulting suspension was processed using a Buchi B-290 spray drier to produce a fine white powder, consisting of the Nb-TiO_2 and latex template, which was followed by heat treatment at 500°C for 2 h under argon in order to remove the latex template. To obtain rutile phase [19], the as-synthesized Nb-TiO_2 powder were heated at 1050°C under hydrogen.

2.3. Preparation of PtNPs/Mesostructured Nb-TiO_2 Composite. The Pt nanoparticles were synthesized by the formic acid method as described in the literature [20–22]. The as-prepared mesostructured Nb-TiO_2 was used as the supporting substrate for Pt deposition. For the deposition of 40 wt% Pt on Nb-TiO_2, 22 mg of $H_2PtCl_6 \cdot 6H_2O$ (7.5 mg Pt) and 1 mL of HCOOH are added to 20 mL of water. Nb-TiO_2 (11.25 mg) was then dispersed in the above solution by mild ultrasonication for 30 min. After this initial dispersion, the solution is heated to 80°C and kept at this temperature for 30 min. After the reaction is completed, the product was washed thoroughly with deionized water and then dried in a vacuum oven at 60°C.

2.4. Physical Characterization. The morphologies and microstructures of the as-prepared samples were examined by scanning electron microscope (SEM, Hitachi S-4800) operated at 5 kV, and transmission electron microscopy (TEM, JEOL JEM-2100) operated at 200 kV. X-ray diffraction (XRD) patterns were recorded on a Bruker D8 Advance diffractometer equipped with a Cu Kα radiation source. X-ray photoelectron spectroscopic (XPS) analysis was carried out in a VG ESCALAB 220iXL, using monochromated Al Kα source (1486.6 eV), at a base pressure of 2×10^{-9} mbar. High-resolution spectra were obtained at a perpendicular take-off angle, using a pass energy of 20 eV and steps of 0.05 eV. All the binding energies were calibrated by referring to the C1s line at 284.8 eV from adventitious carbon. After Shirley background removal, the component peaks were separated using the public domain XPS Peak program version 4.1 [23].

2.5. Electrode Preparation. The electrochemical measurements were conducted at room temperature in a standard three-electrode cell using a glassy carbon (GC) rotating disk electrode (RDE) setup with a voltalab model PGZ100 potentiostat (Radiometer Analytical) and rotation control (MSR, Pine Instruments). A Pt wire served as the counter electrode, with a saturated calomel electrode (SCE) as the reference which was separated from the working electrode compartment by a closed electrolyte bridge. All potentials in this study, however, are referenced to the reversible hydrogen electrode (RHE). The working electrode was prepared with a procedure similar to the one reported previously [8]. Typically, 5 mg catalyst was sonically mixed with 5 mL H_2O/isopropanol/Nafion (5/1/0.0017 in volume ratio) for 12 min to make a suspension. GC disk electrodes (5 mm diameter, 0.196 cm^2, Pine Research Instrument) served as the substrate and were polished to a mirror finish. An aliquot of catalyst suspension was pipetted onto the carbon substrate, resulting in approximate Pt loadings of 13 μgPt cm^{-2} for all catalysts. The catalyst films were dried under flowing nitrogen (N_2) at room temperature.

2.6. Electrochemical Measurements. The working electrode, in an argon (Ar) purged 0.1 M $HClO_4$ solution at room temperature, was first cycled 200 times between 0 and 1.1 V at a 1 V/s scan rate in order to produce a clean electrode surface. The cyclic voltammetry (CV) measurements were conducted by cycling the potential between 0 and 1.1 V, with a scan rate of 20 mV/s. The electrochemical surface areas (ECSA) were calculated from the hydrogen adsorption peak of the CV. The oxygen reduction reaction (ORR) experiments were performed in oxygen-saturated 0.1 M $HClO_4$ solution at room temperature. The RDE rotating rate was 1600 rpm and sweep rate was 5 mV/s. Current densities were normalized in reference to the geometric area of the GC RDE electrode (0.196 cm^2). The CV measurements for accelerated durability tests (ADT) were conducted by potential cycling between 0.60 and 1.40 V in a N_2 purged 0.1 M $HClO_4$ solution at room temperature, with a scan rate of 50 mV/s. In each case, ADT testing consisted of 30,000 cycles.

3. Results and Discussion

Figure 1(a) is an SEM image of the as-synthesized Nb-TiO_2 nanostructures that clearly shows the hollow structures. The typical Nb-TiO_2 spheres have diameters of 100–150 nm, which is the rutile phase confirmed by XRD analysis (JCPDS,

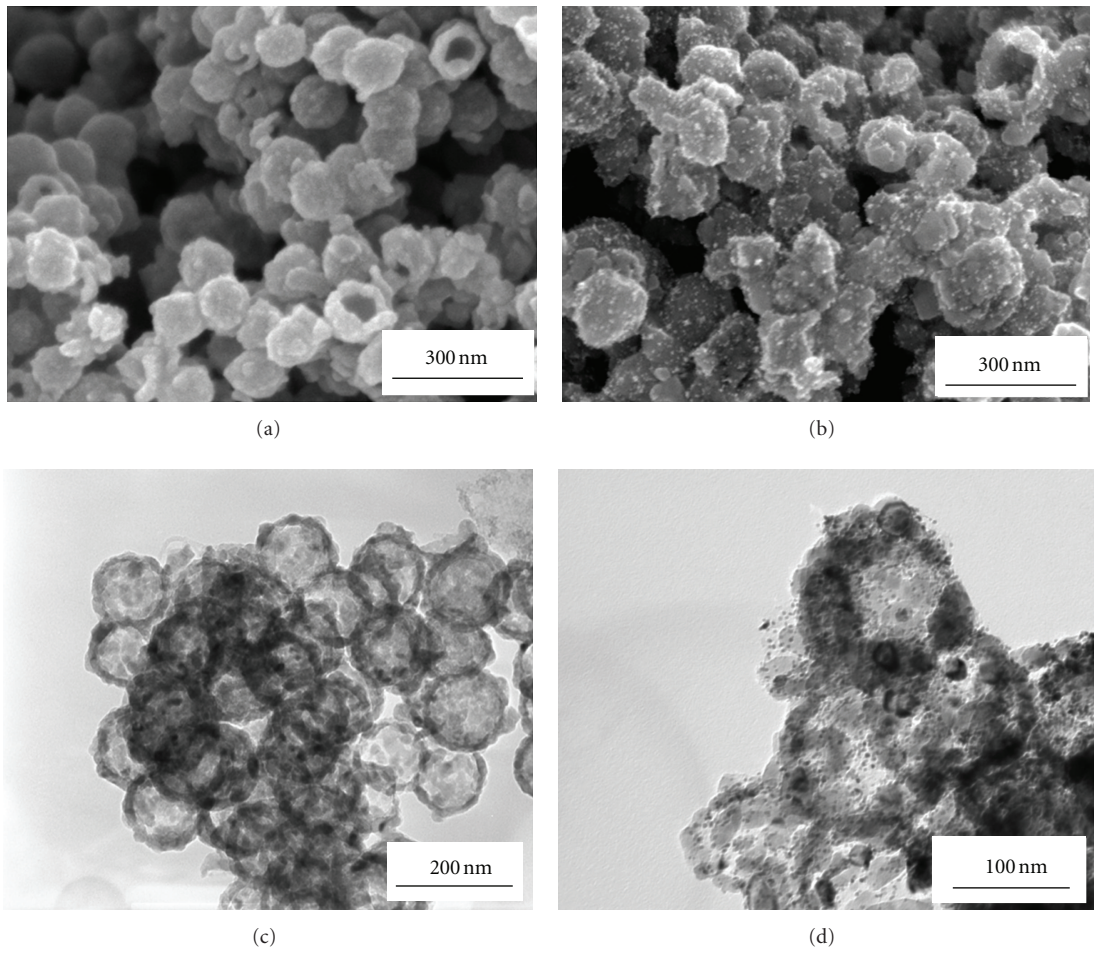

Figure 1: SEM (a) and TEM (c) images pristine hollow Nb-TiO_2 nanostructures. SEM (b) and TEM (d) images Pt nanoparticles deposited on hollow Nb-TiO_2 nanostructures.

no. 21-1276, Figure S1, see Supplementary Material available online at doi:10.1155/2012/389505). The TEM image in Figure 1(c), further confirms that the shape of Nb-TiO_2 nanostructures with mesoporous shells are spherical and fairly uniform in size. Furthermore, each mesoporous shell is composed of small, 10–20 nm nanoparticles. Figures 1(b) and 1(d) show the SEM and TEM images, respectively, of Pt NP/Nb-TiO_2 composite with 20 wt% Pt loading. These images clearly display the homogeneous Pt deposition throughout the Nb-TiO_2 support. The average sizes of Pt nanoparticles on Nb-TiO_2 were obtained by measuring 100 randomly chosen nanoparticles under higher magnification TEM observation (Figure 2(a)). It is clearly seen that Pt nanoparticles with narrow size distribution have the mean size of 4 nm. The selected area electron diffraction (SAED) patterns reveal the single crystallinity of both Pt nanoparticles and the Nb-TiO_2 support. High-resolution TEM (HRTEM) analysis (Figure 2(b)) further confirms the highly crystalline features of the support as well as Pt nanoparticles. The fringes with lattice spacing of 0.23 nm can be indexed as the (111) plane of face-centered-cubic (fcc) Pt, and the angle between two (111) planes also matches well with the fcc Pt. The lattice spacing of 0.25 nm can be indexed to (101) plane of rutile TiO_2.

The Pt loading can be readily tuned by simply changing the mass ratio of the precursor and support, while keeping the ratio between Pt precursor and HCOOH constant. Figure 3(a) shows a TEM image of the product resulting from a mass ratio of H_2PtCl_6 precursor to substrate (Nb-TiO_2) of 1 : 9, corresponding to 10 wt% Pt. At a higher mass ratio of 2 : 3, corresponding to 40 wt% Pt, the density of the Pt nanoparticles increases with some aggregation; however, their size remains consistent at approximately 4 nm.

X-ray photoelectron spectroscopy (XPS) was employed to study the chemical composition and status of the product. Figure 4 shows the Pt 4f, Ti2p, Nb3d, and O1s high-resolution XPS spectra taken from Pt/Nb-TiO_2 composites with different Pt loading levels (10, 20, and 40 wt% Pt), which were calibrated by placing the principal C 1s peak at 284.8 eV. Obviously, continued weakening of the Ti2p signaled at 459.0 and 464.8 eV, Nb3d signaled at 207.6 and 210.3 eV, and O1s signaled at 532 eV is accompanied by the continued strengthening of the Pt 4f signals at 71.1 and 74.4 eV with increasing Pt content [24]. These results suggest that the surface of

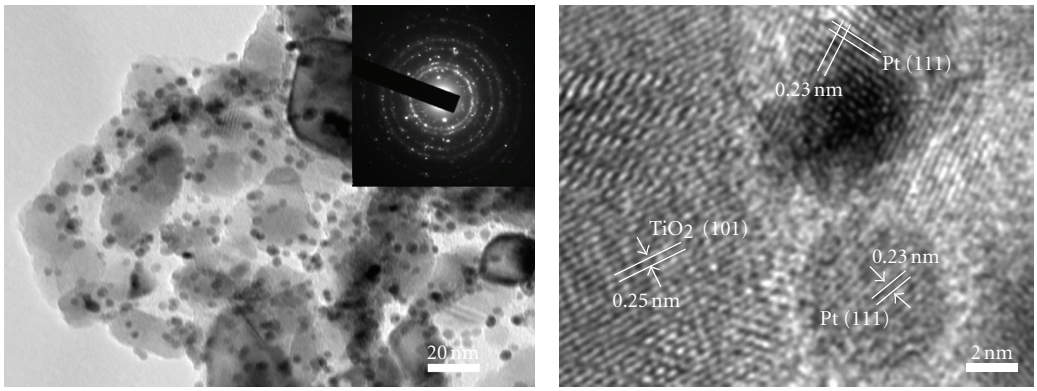

(a) (b)

Figure 2: (a) TEM and (b) HRTEM images of Pt nanoparticles deposited on hollow Nb-TiO_2 nanosphere supports with 20 wt% Pt loading. Pt NPs are single crystal, 4 nm in average size and uniformly dispersed on the surface of hollow Nb-TiO_2 nanosphere supports.

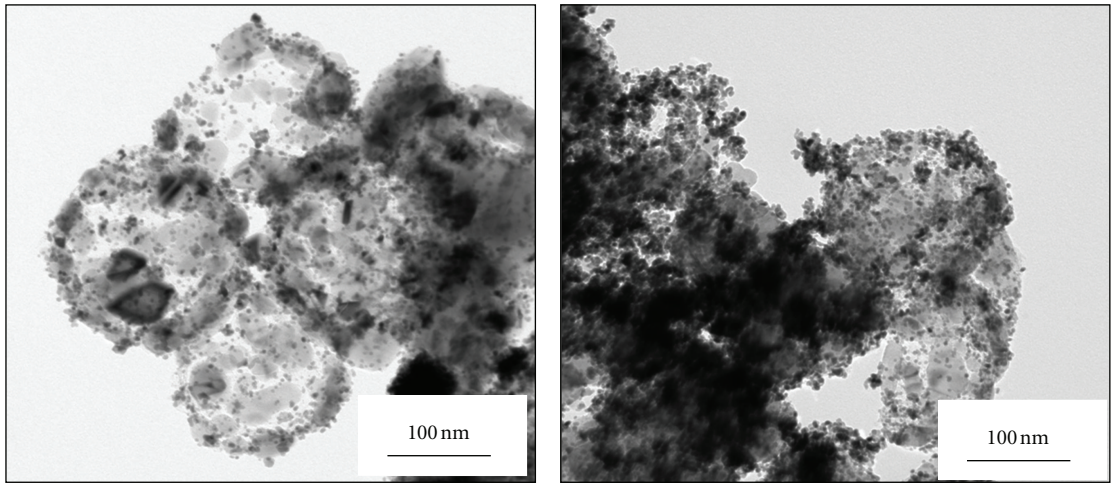

(a) (b)

Figure 3: TEM images of Pt nanoparticles deposited on hollow Nb-TiO_2 nanosphere supports with different Pt loadings. (a) 10 wt% and (b) 40 wt%.

the Nb-TiO_2 spheres becomes more covered with Pt nanoparticles that shield the Nb-TiO_2 surface from the XPS detection. The deconvolution of the Pt spectrum (inset in Figure 4(a)) shows only one doublet assigned as Pt 4f7/2 and Pt 4f5/2, which further confirms that the nanoparticles are pure metallic Pt. We obtained a relative atomic concentration ratio O : Ti of 2 for the products from the experimental XPS peak areas, which further confirms that the support is TiO_2 with 8 at% Nb doping.

To study the electrochemical properties of the Pt NP/Nb-TiO_2 composites, electrochemical measurements were conducted with a glassy carbon electrode (GCE) modified by Pt NPs/Nb-TiO_2 composites, with Pt loadings of 10, 20, and 40 wt%, respectively. For comparison, a GCE supporting a commercial Pt/C catalyst (E-TEK) with 30 wt% Pt loading was also tested. Figure 5(a) shows the cyclic voltammograms (CVs) of these fours catalysts recorded at room temperature in Ar-saturated 0.1 M $HClO_4$ solution at a scan rate of 20 mVs^{-1}. For all electrodes, the Pt loadings were kept at approximately 13.0 $\mu gPt/cm^2$. The CVs show strong peaks characteristic of hydrogen adsorption/desorption peaks below ~0.4 V and Pt oxidation/reduction peaks beyond ~0.6 V, and no considerable change in the shape is seen among these catalysts. The electrochemical surface areas (ECSAs) of Pt catalysts were determined by measuring the charge collected in the hydrogen (H) adsorption/desorption region after double-layer correction and assuming a value of 210 $\mu C/cm^2$ for the adsorption of a monolayer of hydrogen [20]. The obtained ECSAs for the four catalysts are listed in Table 1. We can see that commercial Pt/C catalyst (E-TEK) shows the largest electrochemical surface area (ECSA) with 57 m^2/gPt. The 40 wt% Pt/Nb-TiO_2 has ECSA value of 47 m^2/gPt, followed by the 10 wt% and 20 wt% Pt/Nb-TiO_2 which have ECSA values of 40 m^2/gPt and 37 m^2/gPt, respectively. Interestingly, while there is no observed trend in Pt ECSA with the increasing Pt loading on Nb-TiO_2, it can

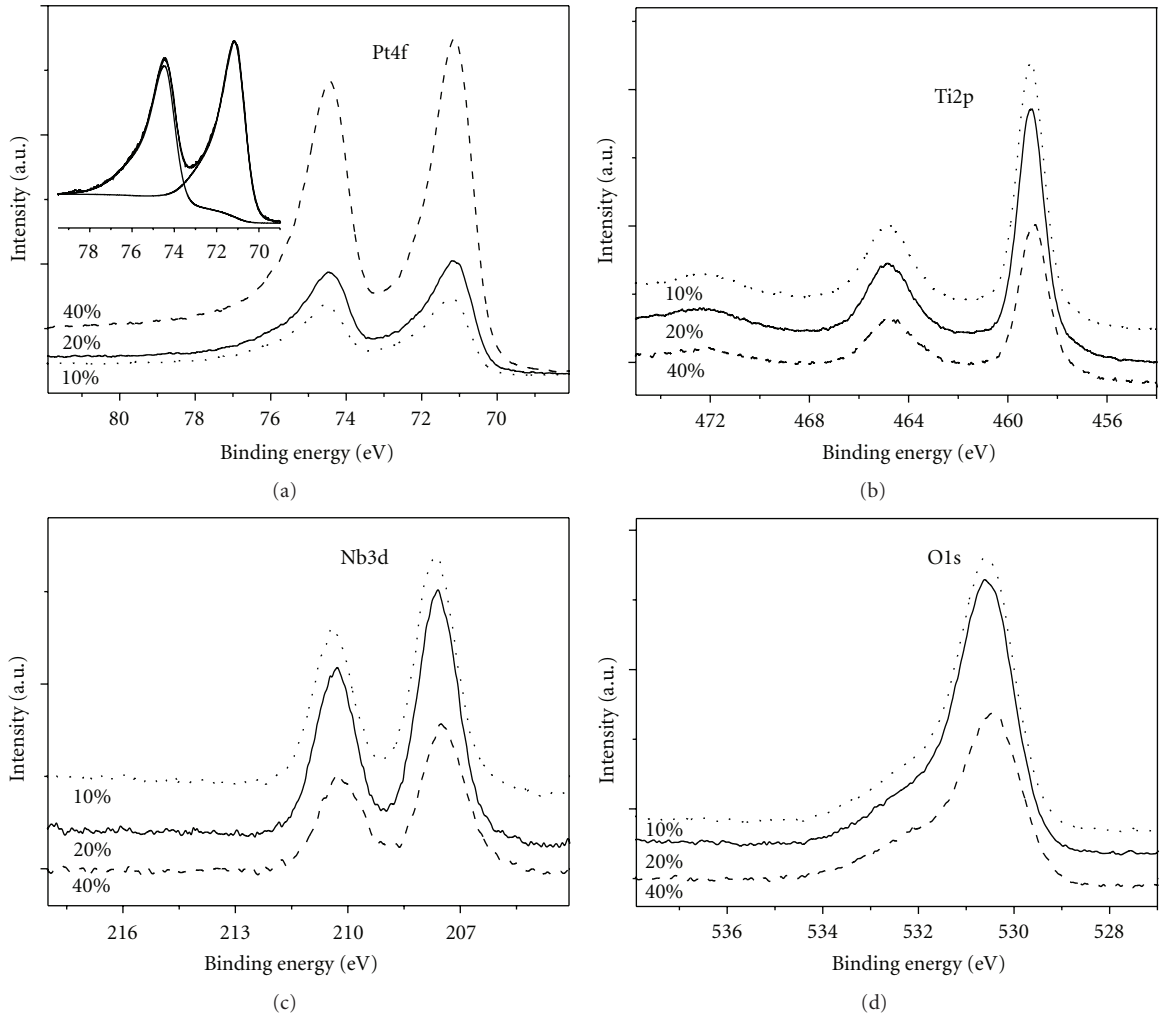

FIGURE 4: High-resolution XPS spectra of (a) Pt 4f; (b) Ti2p; (c) Nb3d; (d) O1S. Inset in (a) shows the corresponding deconvolution of Pt 4f spectrum.

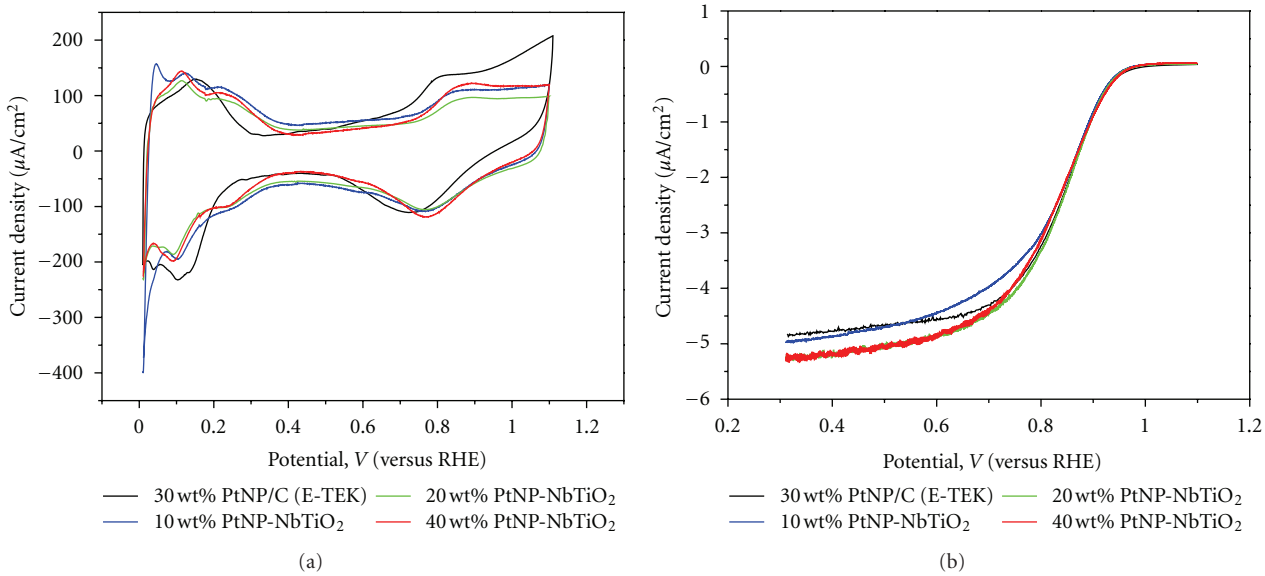

FIGURE 5: (a) CV curves and (b) polarization curves for O_2 reduction on commercial ETEK Pt/C catalyst and Nb-doped TiO_2 with different Pt NP loadings in a 0.1 M $HClO_4$ solution on a disk electrode.

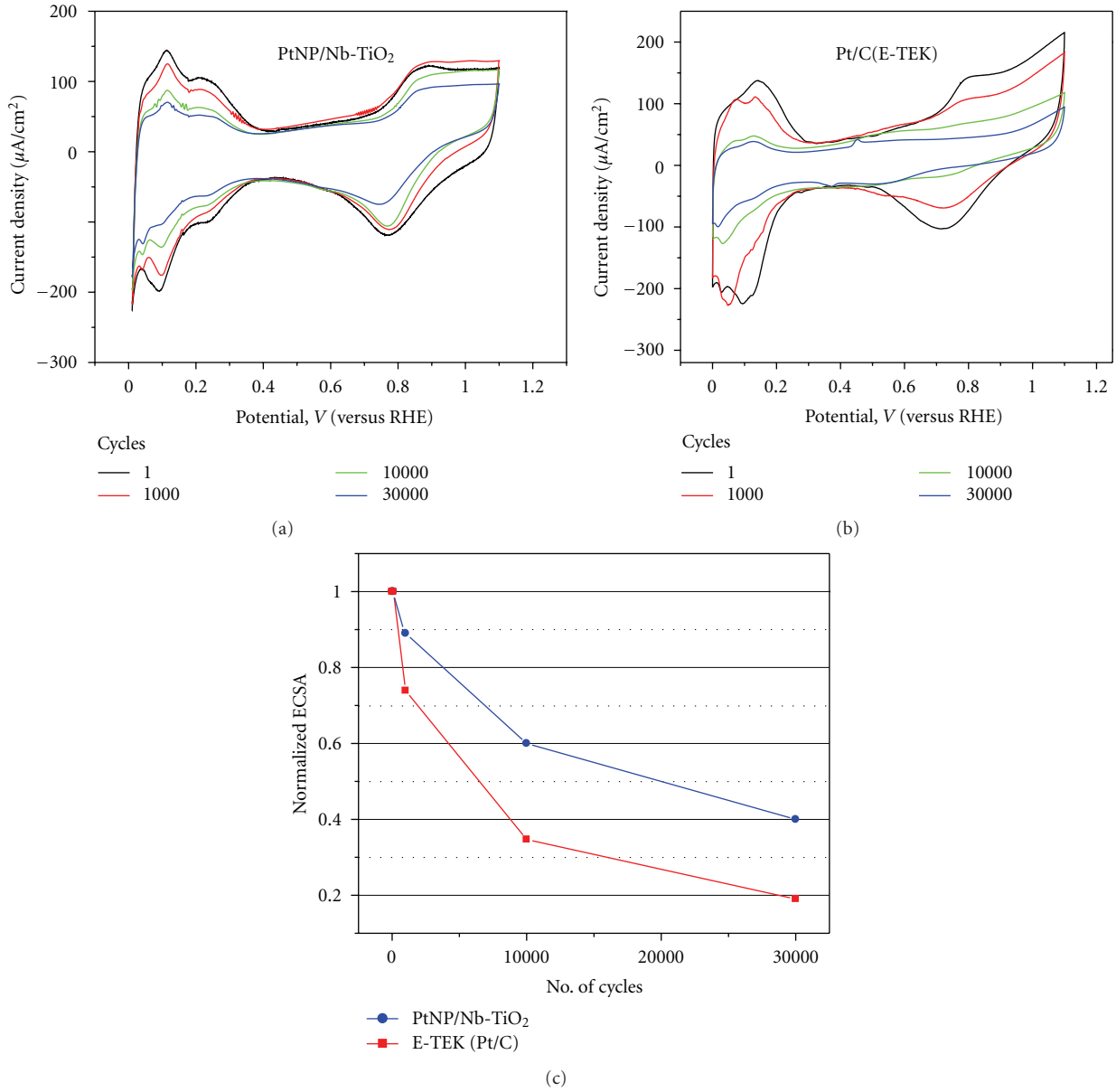

Figure 6: Cyclic voltammograms recorded on (a) PtNP/Nb-TiO_2 and (b) ETEK PtNP/C electrodes in 0.1 M $HClO_4$ solution at room temperature during ADT. (c) ECSAs as a function of cycling numbers on PtNP/Nb-TiO_2 and ETEK PtNP/C electrodes.

be suggested that by this Pt deposition method, similar Pt particle size can be produced even at higher Pt loading on the metal oxide substrate.

Figure 5(b) shows the rotating disk measurements, at 1600 rpm, for the ORR on three Pt/Nb-TiO_2 catalysts, along with the commercial Pt/C catalyst (ETEK) for comparison. The corresponding electrochemical parameters are listed in Table 1. From the figure, the ORR on all catalysts is diffusion controlled when the potential is less than 0.7 V and is under mixed diffusion-kinetic control in the potential region between 0.7 and 0.85 V. From Table 1, we can see that, as compared to the E-TEK Pt/C catalyst, 10 wt% PtNPs/$NbTiO_2$ composite shows the best performance with 15% and 63% higher mass and specific activities, respectively. Furthermore, overall comparison of the ORR activities indicates that all the homemade PtNPs/Nb-TiO_2 composites exhibit higher mass and specific activities than those of the commercial E-TEK Pt/C catalyst. This improvement in activity is significant considering 100 m^2/g BET surface area [15] which is 2/5 of that of Vulcan XC carbon support of commercial Pt/C catalyst. The enhancement in the ORR activity might be due to the homogeneous distribution of small Pt nanoparticles and the mesoporous surface structure of the TiO_2 hollow spheres.

The durability of the catalysts was determined in an accelerated durability test (ADT) by continuously applying linear potential sweeps from 0.60 to 1.4 V (versus RHE), causing surface oxidation/reduction of Pt and the oxidation

Table 1: Comparison of mass and specific activities for ORR and Pt electrochemical surface area of the different catalysts. All these three Pt NP/TiO_2 catalysts show better mass and specific activity than those of the state-of-the-art commercial Pt/C catalyst.

Catalyst	Mass activity at 0.9 V A/mg Pt	Electrochemical-specific surface area m^2/g	Specific activity at 0.9 V $\mu A/cm^2$ Pt
PtNP/C (E-TEK) 30 wt% Pt	0.080	57	140
PtNP-$NbTiO_2$ 10 wt% Pt	0.092	40	228
PtNP-$NbTiO_2$ 20 wt% Pt	0.082	37	223
PtNP-$NbTiO_2$ 40 wt% Pt	0.082	47	175

of support. The surface reaction involves the formation of PtOH and PtO derived from the oxidation of water that causes the dissolution of Pt via the Pt^{2+} oxidation state [25, 26]. The test was conducted by applying potential sweeps at scan rate of 50 mV/s in a N_2 saturated, 0.1 M $HClO_4$ solution at room temperature. For comparison, commercial E-TEK Pt/C (30 wt% Pt) catalyst with a similar Pt loading as that in Pt/Nb-TiO_2 (40 wt% Pt) was subjected to the same potential cycling conditions. It is generally believed that the performance degradation of the electrodes in PEMFC is mainly due to the ECSAs decrease of the catalysts. After 30,000 cycles, changes in the Pt ECSA were determined. As shown in Figures 6(a) and 6(b), cyclic voltammetry was used to determine the Pt surface area of Pt/Nb-TiO_2 and Pt/C electrodes by measuring the H adsorption before and after potential cycling. Figure 6(c) shows that, for Pt/Nb-TiO_2, ~40% of the original Pt surface area remained after 30,000 cycles potential cycling, which is 2.1 times higher than the ~19% remaining for the commercial E-TEK Pt/C catalyst. These results reveal that the Pt on Nb-TiO_2 support is more electrochemically stable. The enhanced stability might be attributed to: (a) the higher corrosion resistance of Nb-TiO_2 support compared to carbon in acidic environments, (b) a strong Pt-metal oxide support interaction inhibiting the sintering of the Pt [16, 17].

4. Conclusions

In summary, we have demonstrated a facile wet-chemical method to grow single-crystalline Pt nanoparticles on mesoporous Nb-doped TiO_2 hollow spheres in aqueous solution, without using any surfactant. The use of Nb-TiO_2 hollow spheres as substrate provides a new type of cost-effective support with high corrosion resistance for growing Pt nanoparticles. The growth density of Pt nanoparticles on Nb-TiO_2 support could be controlled by manipulating the mass ratios between the Pt precursor and the Nb-TiO_2 support. PtNP/Nb-TiO_2 catalysts show enhanced activity and stability compared with the commercial E-TEK Pt/C catalyst.

Acknowledgments

This research was supported by General Motors of Canada, Natural Sciences and Engineering Research Council of Canada (NSERC), Canada Research Chair (CRC) Program, Canada Foundation for Innovation (CFI), and Ontario Early Researcher Award and the University of Western Ontario. S. Sun is grateful to the NSERC CGS scholarship and G. Zhang thanks the NSERC postdoctoral fellowship. The authors thank the help and discussion with Drs. P. Mani, M. Balogh, I. Butta, M. Militello, C. Wong, and X. Xiao.

References

[1] M. Marezio and P. D. Dernier, "The crystal structure of Ti_4O_7, a member of the homologous series Ti_nO_{2n-1}," *Journal of Solid State Chemistry*, vol. 3, no. 3, pp. 430–348, 1971.

[2] R. Borup, J. Meyers, B. Pivovar et al., "Scientific aspects of polymer electrolyte fuel cell durability and degradation," *Chemical Reviews*, vol. 107, no. 10, pp. 3904–3951, 2007.

[3] D. A. Stevens and J. R. Dahn, "Thermal degradation of the support in carbon-supported platinum electrocatalysts for PEM fuel cells," *Carbon*, vol. 43, no. 1, pp. 179–188, 2005.

[4] Y. Shao, G. Yin, and Y. Gao, "Understanding and approaches for the durability issues of Pt-based catalysts for PEM fuel cell," *Journal of Power Sources*, vol. 171, no. 2, pp. 558–566, 2007.

[5] M. S. Saha, R. Li, and X. Sun, "High loading and monodispersed Pt nanoparticles on multiwalled carbon nanotubes for high performance proton exchange membrane fuel cells," *Journal of Power Sources*, vol. 177, no. 2, pp. 314–322, 2008.

[6] T. Ioroi, H. Senoh, S. I. Yamazaki, Z. Siroma, N. Fujiwara, and K. Yasuda, "Stability of corrosion-resistant Magńli-phase Ti_4O_7-supported PEMFC catalysts at high potentials," *Journal of the Electrochemical Society*, vol. 155, no. 4, pp. B321–B326, 2008.

[7] T. Ioroi, Z. Siroma, N. Fujiwara, S. I. Yamazaki, and K. Yasuda, "Sub-stoichiometric titanium oxide-supported platinum electrocatalyst for polymer electrolyte fuel cells," *Electrochemistry Communications*, vol. 7, no. 2, pp. 183–188, 2005.

[8] H. Chhina, S. Campbell, and O. Kesler, "An oxidation-resistant indium tin oxide catalyst support for proton exchange membrane fuel cells," *Journal of Power Sources*, vol. 161, no. 2, pp. 893–900, 2006.

[9] G. Chen, S. R. Bare, and T. E. Mallouk, "Development of supported bifunctional electrocatalysts for unitized regenerative fuel cells," *Journal of the Electrochemical Society*, vol. 149, no. 8, pp. A1092–A1099, 2002.

[10] H. Chhina, S. Campbell, and O. Kesler, "Ex situ evaluation of tungsten oxide as a catalyst support for PEMFCs," *Journal of the Electrochemical Society*, vol. 154, no. 6, pp. B533–B539, 2007.

[11] M. S. Saha, M. N. Banis, Y. Zhang et al., "Tungsten oxide nanowires grown on carbon paper as Pt electrocatalyst support for high performance proton exchange membrane fuel cells," *Journal of Power Sources*, vol. 192, no. 2, pp. 330–335, 2009.

[12] M. S. Saha, R. Li, M. Cai, and X. Sun, "High electrocatalytic activity of platinum nanoparticles on SnO2 nanowire-based electrodes," *Electrochemical and Solid-State Letters*, vol. 10, no. 8, pp. B130–B133, 2007.

[13] M. D. Koninck, P. Manseau, and B. Marsan, "Preparation and characterization of Nb-doped TiO_2 nanoparticles used as a conductive support for bifunctional $CuCo_2O_4$ electrocatalyst," *Journal of Electroanalytical Chemistry*, vol. 611, no. 1-2, pp. 67–79, 2007.

[14] K. W. Park and K. S. Seol, "Nb-TiO_2 supported Pt cathode catalyst for polymer electrolyte membrane fuel cells," *Electrochemistry Communications*, vol. 9, no. 9, pp. 2256–2260, 2007.

[15] M. Cai, Y. Lu, Z. Wu et al., "Making electrocatalyst supports for fuel cells," US patent, Application number: 12/716360, 2010.

[16] H. Chhina, D. Susac, S. Campbell, and O. Kesler, "Transmission electron microscope observation of Pt deposited on Nb-doped titania," *Electrochemical and Solid-State Letters*, vol. 12, no. 6, pp. B97–B100, 2009.

[17] S. J. Tauster, S. C. Fung, and R. L. Garten, "Strong metal-support interactions. Group 8 noble metals supported on TiO_2," *Journal of the American Chemical Society*, vol. 100, no. 1, pp. 170–175, 1978.

[18] F. Leroux, P. J. Dewar, M. Intissar, G. Ouvrard, and L. F. Nazar, "Study of the formation of mesoporous titania via a template approach and of subsequent Li insertion," *Journal of Materials Chemistry*, vol. 12, no. 11, pp. 3245–3253, 2002.

[19] E. Traversa, M. L. Di Vona, S. Licoccia et al., "Sol-gel processed TiO_2-based nano-sized powders for use in thick-film gas sensors for atmospheric pollutant monitoring," *Journal of Sol-Gel Science and Technology*, vol. 22, no. 1-2, pp. 167–179, 2001.

[20] S. H. Sun, D. Q. Yang, D. Villers, G. X. Zhang, E. Sacher, and J. P. Dodelet, "Template- and surfactant-free room temperature synthesis of self-assembled 3D Pt nanoflowers from single-crystal nanowires," *Advanced Materials*, vol. 20, no. 3, pp. 571–574, 2008.

[21] D. Q. Yang, S. Sun, J. P. Dodelet, and E. Sacher, "A facile route for the self-organized high-density decoration of Pt nanoparticles on carbon nanotubes," *Journal of Physical Chemistry C*, vol. 112, no. 31, pp. 11717–11721, 2008.

[22] D. Q. Yang, S. H. Sun, H. Meng, J. P. Dodelet, and E. Sacher, "Formation of a porous platinum nanoparticle froth for electrochemical applications, produced without templates, surfactants, or stabilizers," *Chemistry of Materials*, vol. 20, no. 14, pp. 4677–4681, 2008.

[23] http://www.phy.cuhk.edu.hk/~surface/XPSPEAK/.

[24] F. Moulder, W. F. Stickle, P. E. Sobol, and K. D. Bomben, *Handbook of X-Ray Photoelectron Spectroscopy*, Perkin-Elmer, Eden Prairie, Eden Prairie, Minn, USA, 1992, Edited by J. Chastain.

[25] R. Woods, *Electroanalytical Chemistry*, Marcel Dekker, New York, NY, USA, 1976, Edited by A. J. Bard.

[26] J. Zhang, K. Sasaki, E. Sutter, and R. R. Adzic, "Stabilization of platinum oxygen-reduction electrocatalysts using gold clusters," *Science*, vol. 315, no. 5809, pp. 220–222, 2007.

Hindawi Publishing Corporation
Journal of Nanotechnology
Volume 2012, Article ID 831872, 9 pages
doi:10.1155/2012/831872

Research Article

Titanium as a Potential Addition for High-Capacity Hydrogen Storage Medium

Filippo Zuliani,[1,2] Leonardo Bernasconi,[1,3] and Evert Jan Baerends[1,4,5]

[1] *Theoretische Chemie, Vrije Universiteit Amsterdam, De Boelelaan 1083, 1081 HV Amsterdam, The Netherlands*
[2] *Tata Steel Research, Development and Technology, Tata Steel Europe, 1970 CA Ijmuidem, The Netherlands*
[3] *Science and Technology Facilities Council Rutherford Appleton Laboratory, Harwell Science and Innovation Campus, Didcot, Oxfordshire OX11 0QX, UK*
[4] *WCU Program, Department of Chemistry, Pohang University of Science and Technology, Pohang, Republic of Korea*
[5] *Chemistry Department, Faculty of Science, King Abdulaziz University, Jeddah 21589, Saudi Arabia*

Correspondence should be addressed to Filippo Zuliani, fzuliani74@gmail.com

Received 7 March 2012; Accepted 1 May 2012

Academic Editor: Won Baek Kim

Copyright © 2012 Filippo Zuliani et al. This is an open access article distributed under the Creative Commons Attribution License, which permits unrestricted use, distribution, and reproduction in any medium, provided the original work is properly cited.

We study the adsorption of hydrogen molecules on a titanium atom supported by a benzene molecule using generalized gradient corrected Density Functional Theory (DFT). This simple system is found to bear important analogies with titanium adsorption sites in (8, 0) titanium-coated single-walled carbon nanotubes (SWNTs) (T. Yildirim and S. Ciraci, 2005) In particular, we show that up to four H_2 molecules can coordinate to the metal ion center, with adsorption patterns similar to those observed in Ti-SWNTs and no more than one molecule dissociating in the process. We analyze in detail the orbital interactions responsible for Ti-benzene binding and for the electron transfer responsible for the H_2 dissociation. We find the latter to involve a transition from a triplet to a singlet ground state as the hydrogen molecule approaches the adsorption site, similar to what has been observed in Ti-SWNTs. The total Ti-H_2-binding energy for the first dissociative addition is somewhat inferior (~0.4 eV) to the value estimated for adsorption on Ti-SWNTs. We analyze in detail the orbital interactions responsible for the H_2 binding.

1. Introduction

Developing safe, cost-effective, and practical means of storing hydrogen is crucial for the advancement of hydrogen and fuel-cell technologies [1–3]. In this context, titanium-decorated organic compounds have received attention for their potential use as high-capacity hydrogen storage materials [4–9]. More in specific, studies based on generalized gradient DFT and first-principle molecular dynamics simulations have indicated that a single-titanium atom supported on an insulating (8, 0) SWNT can bind up to four hydrogen molecules [10]. Since high titanium coverages on SWNTs are achievable in experimental conditions, these materials could provide means to reach, or even exceed, the minimum hydrogen storage capacity required for technological applications.

Adsorption of one H_2 molecule to a titanium site was found to proceed with a vanishing activation energy and to involve interactions between carbon atoms, titanium, and the hydrogen molecule which are essentially short ranged and localized at the absorption site. It was proposed that the mechanism responsible for the H_2 bonding involves d orbitals of the Ti atom, the antibonding σ_u of a H_2 molecule, and p orbital at carbon sites.

In this paper we present a DFT study that elucidates the catalytic role played by the Ti atom in the dissociation of the H_2 molecule and in the bonding mechanism of the Ti atom and the four hydrogen molecules, characterized as "an unusual combination of chemisorption and physisorption" [10]. According to the results presented here, the same number of hydrogen molecules can be stored in essentially the same configuration introducing a different support for the Ti catalyst, the benzene molecule. The benzene molecule thus offers a hexagonal ring as support for Ti which is electronically very similar to the (8, 0) SWNT, so that bonding of H_2 molecules can be studied in detail using well-established molecular energy decomposition techniques and programs [11].

The paper is organized as follows. Details about the calculations are given in Section 2. The adsorption and dissociation of a H_2 molecule on benzene-supported titanium is analyzed in Section 3.1, and the possible addition patterns for two and four molecule additions are studied in Section 3.3. Our results are briefly summarized in Section 4.

2. Computational Details

Calculations have been performed using the Amsterdam Density Functional program (ADF) [12–14]. The molecular orbitals (MOs) were expanded in large uncontracted sets of Slater-type orbitals containing diffuse functions of TZ2P quality. A small frozen core (1s for C, 1s–2p for Ti) was used in the present calculations. Equilibrium structures were optimized using analytical gradient techniques, with geometries and energies calculated at the OLYP [15, 16] level of theory. Our choice for the functional is motivated by its superior performance for the relative energies of different spin states of various transition-metal complexes in the gas phase, in particular when high-spin states are involved [17–19]. Interactions between H_2 molecules and the C_6H_6-Ti complexes were analyzed using the molecular fragment method that is a standard tool in energy decomposition methods for interactions between molecules, as detailed in Reference [11]. We use here primarily the description of the orbitals of the overall system expressed as linear combinations of fragment orbitals. The obvious fragments here are Ti, benzene and H_2 molecules. The orbitals of these fragments are obtained (in the exact geometry they have in the total system) in separate calculations. These orbitals are then used as basis functions in the overall calculation. This affords an analysis of the overall orbitals in terms of percentages of the contributing fragment orbitals.

3. Results and Discussion

3.1. Orbital Interactions and Bonding in C_6H_6-Ti. The structure of the C_6H_6-Ti complex has been theoretically [20–27] and experimentally [28] studied on the basis of DFT calculations and laser evaporation methods. Experimental evidence indicates the ground state to be a triplet in a planar C_{6v} configuration. We show in Figure 1 the orbital interaction diagram of the benzene molecule and the Ti atom obtained at the OLYP level of theory for the optimized triplet C_{6v} configuration. In this analysis, the C_6H_6-Ti (C_{6v}) compound was divided in two fragments: the isolated Ti atom and the benzene support, their geometries fixed to the relaxed interacting configuration. From now on, we will take the xy-plane as the plane parallel to C_6H_6. When interacting with the planar C_6H_6, the 3d set of the metal atomic orbitals (AOs) are split into three levels of E_2, A_1, and E_1 symmetry, the $3da_1$ (d_{z^2}) orbital, two $3e_2$ (d_{xy} and Ti-$3d_{x^2-y^2}$), and two $3e_1^*$ (d_{xz} and d_{yz}) orbitals, respectively. The important bonding interaction is between the benzene π orbitals of E_1 symmetry and the Ti-$3d_{xz,yz}$ orbitals, which is understandable considering the relatively large overlap between these favorably oriented orbitals. This leads to significant stabilization of the bonding combination and destabilization of the antibonding combination. There is a weaker interaction between the π orbitals of E_2 symmetry and the Ti-$3d_{xy}$ and Ti-$3d_{x^2-y^2}$ orbitals, which are parallel to the benzene plane and little interaction of the $3d_{z^2}$ with the much lower lying C_6H_6-π orbital of A_1 symmetry. The $3da_1$ (Ti-$3d_{z^2}$) AO is somewhat stabilized by the small hybridization with the 4s and 4p of the same symmetry. The orbital pattern for the d orbitals is reminiscent of the one for sandwich complexes, but a peculiarity of the C_6H_6-Ti system is the presence of a low-lying 4s orbital, hardly displaced from its atomic position [26, 29]. This is related to Ti being coordinatively very unsaturated; in highly coordinated (hexa- or penta-coordinated) metal complexes the 4s is invariably very much destabilized by the orthogonality requirement on the occupied ligand orbitals.

The four d electrons of Ti are available to go into the C_6H_6Ti-de_2 and -da_1 orbitals. Because there is only a small gap between these orbitals, the "high-spin" configuration $(e_2)^3$ $(da_1)^1$ results, leading to a triplet ground state of E_2 symmetry. This is Jahn-Teller distorted, so that the degeneracy of the e_2 MO is lifted. Our OLYP calculations predict a triplet-C_{2v} configuration as ground state of the C_6H_6-Ti compound, with the quintet-C_{6v} $(e_2)^2$ $(da_1)^1$ $(4s)^1$ and triplet-C_{6v} $(e_2)^3$ $(da_1)^1$ $(4s)^0$ configurations lying higher in energy by 0.372 and 0.242 eV, respectively. Previously, both triplet-C_{2v} [20, 24, 26] and quintet-C_{6v} [21–23, 25, 27, 28] states have been theoretically predicted as possible ground states. However, a quintet-C_{6v} ground state was predicted only by the B3LYP method, and previous studies on the reaction products formed between group 5 transition metals (V, Nb, Ta) and benzene revealed the B3LYP method to calculate the correct ground state only for the C_6H_6-Nb complex [29]. It was already suggested that triplet-C_{2v} is the real ground state of the C_6H_6-Ti complex [26] at DFT-PBW91 level of theory, and our OLYP evidence leads us to agree with such suggestions. Conclusive evidence from experimental data on the ground state of the C_6H_6-Ti complex is, however, still lacking.

As a consequence of the Jahn-Teller distortion, the planar C_{6v} C_6H_6 structure undergoes a deformation, characterized by a ruffling of the C_6 ring (up or down displacement of the C atoms along the z-axis), Figure 1. Also, an elongation of all the C–C bonds in the C_6H_6-Ti compound of up to 4% is observed, because of the charge donation from the C_6H_6 bonding e_1 states to the metal atom. The C_{6v} planar configuration may distort in two different ways towards a C_{2v} configuration, one characterized by a displacement along the z-axis of two *para* carbon atoms towards Ti, labeled as [4 + 2], the other one by displacement of the other four carbon atoms towards Ti, labeled as [2 + 4] configuration. In both cases, the distance along the z-axis between the Ti and the displaced C atoms is reduced from the C_{6v} value of 1.66 Å to 1.56 and 1.59 Å values of the [2 + 4] and [4 + 2] C_{2v} configurations, respectively. Energies reported in Figure 2 are relative to the C_{6v} structure with planar C_6H_6.

Figure 3 shows the electronic structure of the C_6H_6Ti (C_{2v} – [2 + 4]) complex. The Jahn-Teller distortion from the planar C_{6v} to the [2 + 4] distorted C_{2v} structures causes

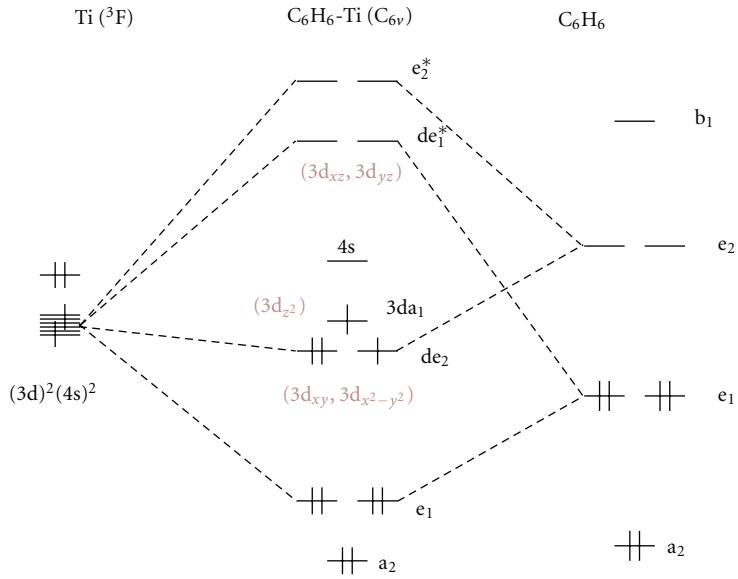

Figure 1: Orbital interaction diagram of the C_6H_6Ti -C_{6v} configuration.

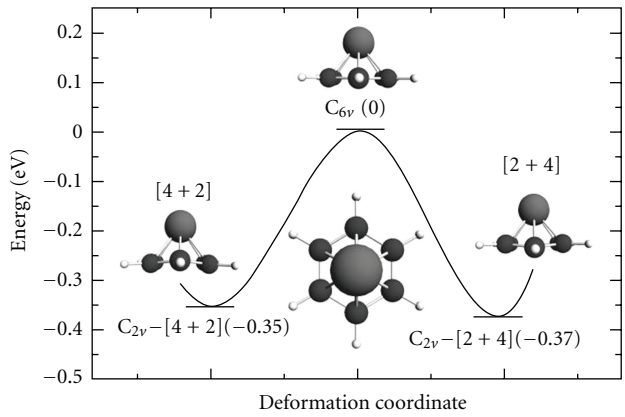

Figure 2: Energy diagram at DFT-OLYP level of the calculated C_6H_6-Ti triplet configurations. The smooth line is a pure schematic guide between the three configurations. Hydrogen, carbon, and titanium atoms are shown in white, dark grey, and light grey, respectively.

a splitting of the degenerate C_6H_6Ti de_2 levels (Figure 1) into the $8a_1$ and $3a_2$ states as shown in Figure 3. These now lie lower in energy than the Ti-$3d_{z^2}$ (he $9a_1$ in Figure 3) with $3da_1$ (Figure 1) parentage. In the corresponding [2 + 4] configuration of the benzene, the e_2 LUMO splits into an a_2 and an a_1 orbital, which stabilize the $8a_1$ (Ti-$3d_{x^2-y^2}$) and $3a_2$ (Ti-$3d_{xy}$) MOs by admixing in a bonding fashion. The x-axis is perpendicular to the direction of the 2 C atoms of the [2 + 4] structure (and again the 2 C atoms of the [4 + 2] structure). The triplet C_{2v} – [2 + 4] configuration is thus characterized by a doubly occupied $8a_1$-Ti-$3d_{x^2-y^2}$ state and singly occupied $9a_1$-Ti-$3d_{z^2}$ and $3a_2$-Ti-$3d_{xy}$ states. In the alternative C_{2v} – [4 + 2] Jahn-Teller configuration, the splitting of the e_2 is reversed, the $3a_2$-Ti-$3d_{xy}$ state lies lower in energy, while the Ti-$3d_{x^2-y^2}$ lies in higher position. Thus, the electron configuration in the distorted [4 + 2] geometry is characterized by a doubly occupied $3a_2$-Ti-$3d_{xy}$ state of the metal atom and a singly occupied Ti-$3d_{x^2-y^2}$. However, in both configurations, the $3d_{z^2}$ state is singly occupied ($9a_1$ state in both [2 + 4] and [4 + 2] configurations). In all cases the empty Ti-4s ($10a_1$) is present, which potentially could act as acceptor orbital for electrons from the approaching H_2.

3.2. H_2 Dissociative Adsorption on C_6H_6-Ti. Taking the triplet C_{2v} – [2 + 4] as the representative electronic ground state of the C_6H_6-Ti compound, we now turn to investigate the role played by the Ti addition in the adsorption of the four H_2 molecules on the C_6H_6-Ti compound reported by Yildirim and Ciraci [10]. The first H_2 addition proved to lead to dissociation of the corresponding hydrogen molecule, while an additional three molecules could be weakly bonded to the Ti atom on the SWNT surface. We therefore obtain here, for the C_6H_6-Ti compound, the same H_2 adsorption pattern observed in the (8, 0) Ti-SWNT studied in Reference [10].

Figure 4 shows the total energies of the $C_6H_6TiH_2$ complex as a function of the distance between the metal atom and the center of mass of the approaching H_2. All energies are relative to the value of the triplet curve at large distance, that is, the chosen energy zero is the sum of the energies of isolated ground state H_2 and ground state triplet C_6H_6Ti[2 + 4]. For each value of the constrained Ti-H_2 distance a full geometry optimization was carried out in both triplet and singlet states by relaxing to equilibrium all unconstrained degrees of freedom. The H_2 approach turns out to be with the center of mass on the z-axis and the H_2 bond axis perpendicular to the z-axis and in the direction of the two equivalent C atoms of the [2 + 4] configuration, which is the x-axis. Similar to the H_2 adsorption on a SWNT [10] we find the C_6H_6Ti-H_2 complex to be in a triplet ground state at large Ti-H_2 distances and to undergo a transition to the singlet at 1.72 Å. At variance with the barrierless dissociative adsorption of H_2 on the (8, 0) Ti-SWNT studied in Reference

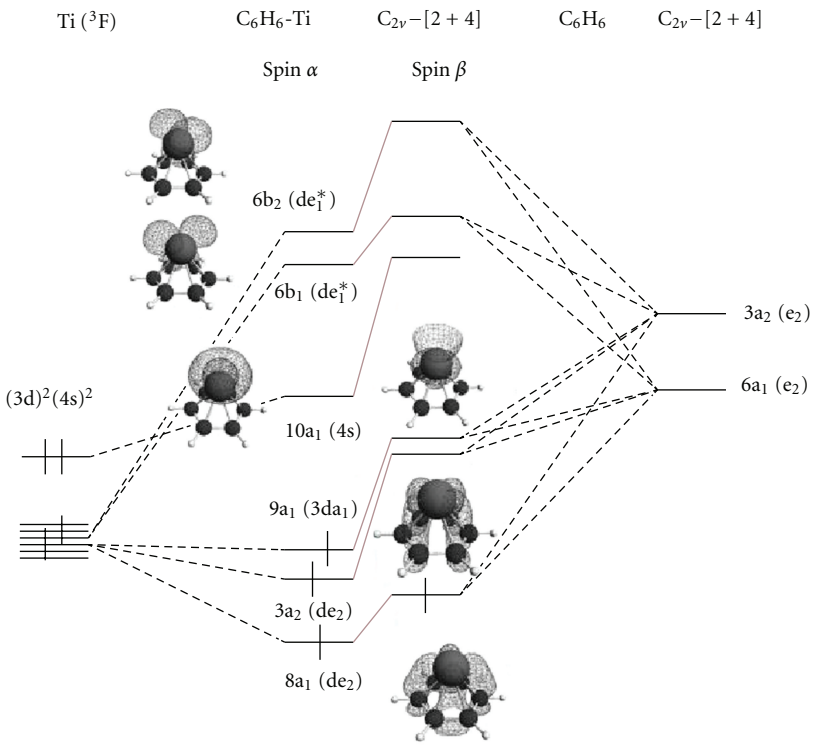

FIGURE 3: MO interaction diagram of the formation of C_6H_6Ti C_{2v} − [2 + 4] from Ti and C_6H_6. In parentheses the parentage of the levels from those of C_{6v} C_6H_6Ti (with planar C_6H_6), see Figure 1. Hydrogen, carbon, and titanium atoms are shown in white, dark grey, and light grey, respectively.

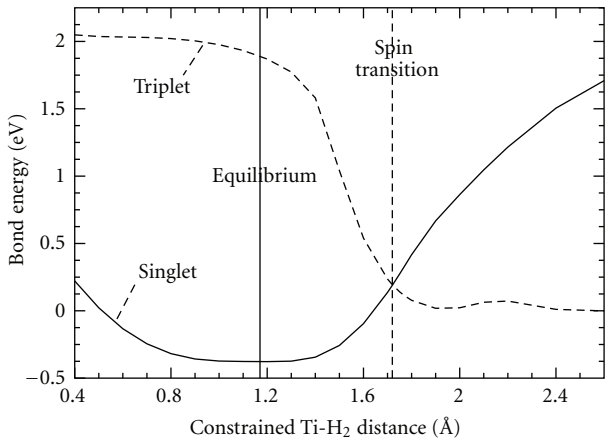

FIGURE 4: Total energies of the $C_6H_6Ti[2 + 4]$-H_2 complex for different constrained Ti-H_2 distances, measured from Ti to the center of mass of H_2. H_2 approaches perpendicular to the z-axis, lying along the x-axis (in the direction of the 2 C atoms of the [2 + 4] structure). The triplet and singlet states (dashed and straight line, resp.) are compared. Vertical lines indicate the equilibrium distance of 1.12 Å (straight line) and the transition point at 1.72 Å (dashed line). All energies are relative to the value of the triplet curve at large distance we indicated as zero.

[10], a finite barrier (0.17 eV) is computed here for the H_2 addition to C_6H_6Ti, given by the difference between the energy at the spin transition and the energy at the minimum of the triplet spin surface. The absence of a barrier for H_2 dissociation in the (8, 0) Ti-SWNT is likely to arise from a selective stabilization of the singlet state relative to the triplet in the Ti-SWNT compared to C_6H_6Ti. In Figure 4 this would result in the singlet curve joining smoothly the triplet one at Ti-H_2 distances lower than ∼2 Å.

The H_2 lowest unoccupied orbital (LUMO) $1\sigma_u$ has B_1 symmetry in C_{2v}, so it cannot mix with the de$_2$ orbitals (8a$_1$ and 3a$_2$ in Figure 3) or with the 3d$_{z^2}$ or 4s (both A_1), but it mixes very strongly with the e$_1^*$-derived Ti-3d$_{xz}$ (the 6b$_1$ of the C_6H_6Ti fragment). This orbital is a typical frontier orbital which is hybridized with the 4p$_x$ and thereby acquires a large amplitude towards the incoming H_2. The strong interaction of $1\sigma_u$ and 3d$_{xz}$ results in a low-lying stabilized strongly mixed $C_6H_6TiH_2$-6b$_1$ level (Tables 1 and 2 and Figure 5). As the H_2 molecule approaches the C_6H_6Ti compound, this level stabilizes so much that it becomes successively occupied with two (spin-paired) electrons, which may be pictured as coming from the originally singly occupied 9a$_1\alpha$ and next 3a$_2\alpha$ of $C_6H_6Ti[2 + 4]$ of Figure 3. This is a typical example of a bond-breaking reaction, where the initially empty strongly H–H-antibonding orbital becomes occupied. The stabilization of the $1\sigma_u$ which makes the mixing with 3d$_{xz}$ very strong is of course concomitant with the stretching of the H_2 molecule (the bond breaking). The whole process only requires a very low barrier of 0.17 eV.

The interaction of H_2 with a transition metal is often weak, because occupied metal orbitals have Pauli repulsion

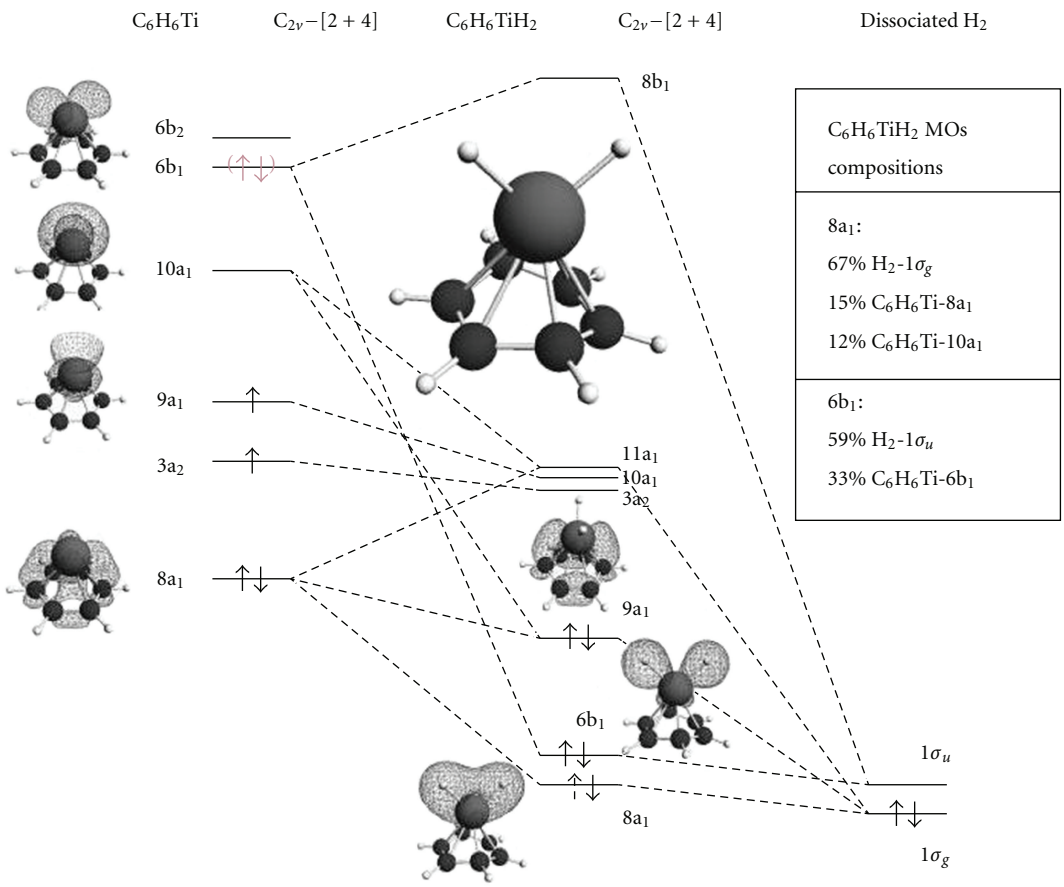

Figure 5: MO diagram for the C_6H_6Ti-H_2 dissociative interaction. Hydrogen, carbon, and titanium atoms are shown in white, dark grey, and light grey, respectively.

Table 1: $C_6H_6TiH_2$ MOs energies (eV). Orbital labels refer to Figure 5.

	d(Ti-H_2) (Å)		
	2.2 (↑/↓)	1.72 (↑↓)	1.17 (↑↓)
$C_6H_6TiH_2$-$6b_1$	−2.71/−1.55	−3.85	−5.64
$C_6H_6TiH_2$-$8a_1$	−11.50/−11.28	−6.53	−5.94

Table 2: $C_6H_6TiH_2$ MOs composition (%). Orbital labels refer to Figure 5.

		d(Ti-H_2) (Å)		
		2.2 (↑/↓)	1.72 (↑↓)	1.17 (↑↓)
$C_6H_6TiH_2$-$6b_1$	$1\sigma_u$	22/44	48	59
	$6b_1$-$3d_{xz}$	55/42	41	33
	$1\sigma_g$	89/91	74	67
$C_6H_6TiH_2$-$8a_1$	10_1-4s	3/3	8	12
	$9a_1$-$3d_{z^2}$	1/1	8	
	$8a_1$-$3d_{x^2-y^2}$			15

with the occupied $1\sigma_g$ orbital of H_2, preventing H_2 from coming so close that the interaction of a metal d orbital with the H_2 $1\sigma_u$ orbital can become strong. Typically another occupied metal d orbital then interacts only weakly with the high-lying $H_2 1\sigma_u$, resulting in weak backdonation. In the present case the coordinatively unsaturated Ti atom, with relatively few d electrons (as an early transition metal in the 3d series), offers a route to strong interaction and H_2 bond breaking. The $1\sigma_g$ mixes (allowed by symmetry) with the 4s and the $3d_{z^2}$ states ($9a_1$ and $10a_1$ of the C_6H_6Ti fragment) but not with the $3d_{x^2-y^2}$ ($8a_1$), see Table 2. The antibonding combination of $3d_{z^2}$ and $1\sigma_g$, embodying the Paul repulsion, is destabilized in the process and loses its electron to the downwards moving $6b_1$. The loss of the electron from the antibonding orbital implies disappearance of the Pauli repulsion, and the H_2 can approach unhindered to optimize the interaction of $1\sigma_u$ with $3d_{xz}$ in the now fully occupied $6b_1$, which leads to the bond breaking. At the same time, there is a low-lying bonding combination of the (mostly) $1\sigma_g$ orbital with the Ti-$3d_{z^2}$, resulting in the orbital $8a_1$, which remains fully occupied (with the original two electrons of $1\sigma_g$). This orbital is further stabilized by favorable mixing with the Ti 4s ($10a_1$) and the Ti-$3d_{x^2-y^2}$ (note the percentages of 12% and 15%, resp. in the $8a_1$, Table 2). This contributes to the force pulling H_2 to Ti. So ultimately the two electrons

of H_2 end up in the Ti-$1\sigma_g(H_2)$ bonding orbital $8a_1$ and out of the four Ti electrons two go into the Ti-$1\sigma_u(H_2)$ bonding orbital $6b_1$ (H–H bond breaking), while the two remaining ones reside in the largely nonbonding Ti-$3d_{x^2-y^2}$ ($9a_1$). The final resulting electron configuration has only doubly occupied orbitals, that is, it is a singlet state. The transition from the triplet to the singlet state occurs at a distance of 1.72 Å between the Ti atom and the incoming H_2 molecule.

Figure 5 shows the orbital interactions between the C_6H_6Ti complex and the adsorbed H_2 molecule in the singlet equilibrium geometry. For analysis the systems was divided into two fragments: the C_6H_6Ti C_{2v} – [2 + 4] complex described before and the hydrogen molecule with the H–H distance lengthened to the dissociated value (2.61 Å). At such a long H–H distance the $1\sigma_g$ (A_1 symmetry in C_{2v}) and $1\sigma_u$ (B_1 symmetry) orbitals have little bonding/antibonding character left and are almost degenerate. As described above, these two H_2-based orbitals enter the orbital energy diagram as the states $8a_1$ and $6b_1$, below the 3d orbitals, with a good deal of mixing of these H_2 orbitals and the metal orbitals. The internal caption in the figure shows the composition of the $C_6H_6TiH_2$ C_{2v} – [2 + 4] $8a_1$ and $6b_1$ MOs.

3.3. Adsorption of Two and Four H_2 Molecules. Turning now to the addition of two H_2 molecules, we observe that Figure 6 shows two adsorption patterns, one in which one of the H_2 molecules is dissociated (Figure 6(a)) and one in which purely molecular adsorptions are observed (Figure 6(b)). In the dissociative configuration (a) the distance between the centers of mass of the first and the second H_2 molecule and the Ti is predicted to be 0.76 and 1.81 Å, respectively, with a lengthened 0.84 Å bond for the second nondissociated molecule and a H–H distance of 3.22 Å for the dissociated one. The H–H distance in a free H_2 molecule is 0.74 Å. In the configuration (b), the two H_2 molecules were added in a position other than the on-top adsorption site of the Ti. The optimized geometry predicted a displacement between the center of mass of the two H_2 molecules and the Ti atom of 0.98 Å and 1.77 Å along the z-axis and the xy-plane, respectively. The adsorbed H_2 bond length was calculated to be 0.78 Å. The first configuration is energetically favored by 0.38 eV over the second.

Table 3 shows the composition of the MOs involved in the donation/backdonation bonding mechanisms. In the configuration (a), the system was divided again in two fragments: $C_6H_6TiH_2$ and the second undissociated H_2 molecule. In the configuration (b), the system was divided into a C_6H_6Ti and two H_2 fragments. In both configurations, the added H_2 molecules bind weakly to the Ti and do not dissociate with bonding energies of 0.10 and 0.20 eV per H_2 molecule, respectively.

In the configuration (a), the dissociation of the second H_2 molecule is hindered by the double occupancy of the $C_6H_6TiH_2$-$8a_1$ orbital, which prevents the second H_2 molecule from approaching the adsorption site by the Pauli repulsion (occupied-occupied orbital repulsion of $1\sigma_g$ with $8a_1$). Strong mixing of the high-lying H_2 $1\sigma_u$ with a suitable occupied metal fragment orbital is therefore blocked, and

Table 3: Compositions of the MOs involved in the H_2 donation/backdonation bonding mechanism for the adsorption of two H_2 molecules on the C_6H_6Ti complex.

$C_6H_6TiH_2$-H_2	C_6H_6Ti-$2H_2$
$6a_1$	$3b_1$
83% H_2-$1\sigma_g$	91% H_2-$1\sigma_g$ (x2)
7% $C_6H_6TiH_2$-$10a_1$	6% C_6H_6Ti-$6b_1$
$6b_1$	$6a_1$
87% $C_6H_6TiH_2$-$6b_1$	85% H_2-$1\sigma_g$ (x2)
10% H_2-$1\sigma_u$	4% C_6H_6Ti-$6a_1$
	$3b_2$
	88% C_6H_6Ti-$3a_2$
	10% H_2-$1\sigma_u$ (x2)

significant stabilizing mixing between the $1\sigma_g$ and the empty $10a_1$-$3d_{z^2}$ and the $11a_1$-4s is also prevented. Charge donation from the C_6H_6Ti complex to the $1\sigma_u$ of the second H_2 molecule is thus avoided, (which could take place in the first dissociative H_2 addition and caused the H–H bond breaking). The empty $10a_1$ and $11a_1$ orbitals, with large $3d_{z^2}$ and 4s character, do act to some extent as acceptor orbitals (cf. the 7% $10a_1$ mixing with the $1\sigma_g$ in Table 3), but bond breaking would require the antibonding $1\sigma_u$ orbital to be filled.

In the configuration (b), the dissociation of the two H_2 molecules does not occur since the orbital overlaps between the C_6H_6Ti and H_2 remain too weak in this configuration. For instance, the calculated overlap between $9a_1$ and $1\sigma_g$ was 0.114, while a 0.765 value was obtained for the C_6H_6Ti-H_2 dissociative adsorption described before. The two H_2 molecules should approach the C_6H_6Ti fragment more closely in order to build better overlaps but would then experience substantial repulsion. The first dissociation in configuration (a) occurs because the antibonding H_2 orbital $1\sigma_u$ gets filled through its strong interaction with the exposed Ti-$3d_{xz}$. In general, dissociation requires that electrons are dumped into the antibonding (bond-breaking) orbital. This does not occur in configuration (b) because of the repulsion between C_6H_6Ti-$8a_1$ and $1\sigma_g$'s. In addition, bond breaking requires occupation of the $1\sigma_u$ orbitals. In the depicted configuration the $1\sigma_u$ orbitals cannot, however, establish strong interactions with unoccupied $C_6H_6TiH_2$ orbitals and gain sufficient stabilization to bring about its occupation through the mechanism described above. A weak donation/backdonation mechanism is therefore responsible for the bonding between the Ti atom and the two H_2 molecules also in this second configuration. Note that the C_6H_6Ti-$6b_1$, $6a_1$ and $3a_2$ states indicated in the right panel of Table 3 consist mainly of the Ti-$3d_{xz}$, a lower lying C_6H_6-e_1 and the Ti-$3d_{xy}$/C-p_z states, respectively.

We next consider the adsorption of four H_2 molecules on the C_6H_6Ti complex. In this case, two stable four-H_2 adsorption patterns were computed (Figure 7). We denote these two different configurations as TiH_2 + $3H_2$ (Figure 7(a)) and Ti + $4H_2$ (Figure 7(b)). These equilibrium structures are clearly related to the corresponding geometries in the two-H_2 addition patterns (Figure 6). In both cases, no more than one

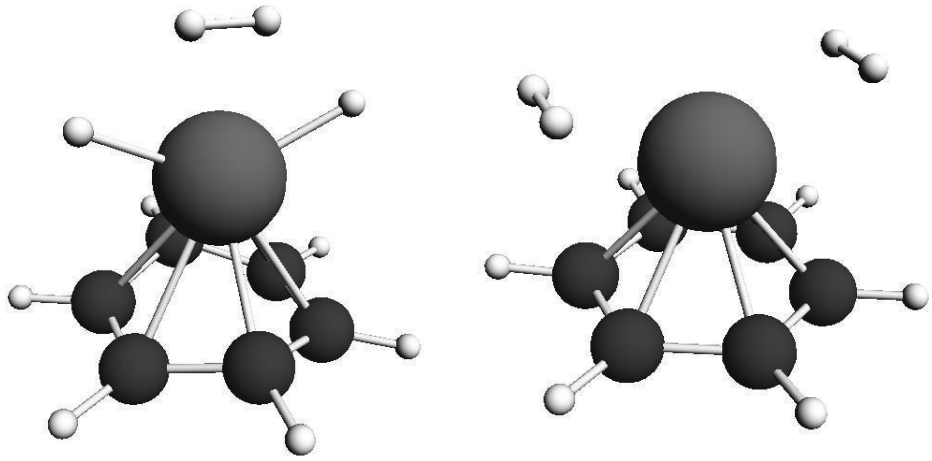

(a) (b)

Figure 6: Adsorption patterns of two H_2 molecules addition: (a) $C_6H_6Ti\ H_2$-H_2, (b) C_6H_6Ti -$2H_2$. Hydrogen, carbon, and titanium atoms are shown in white, dark grey, and light grey, respectively.

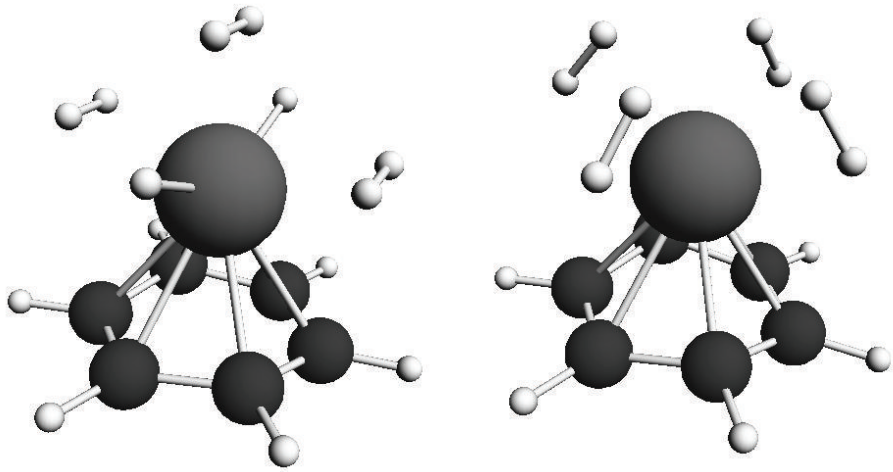

(a) (b)

Figure 7: The two most stable four-H_2 addition patterns: (a) TiH_2 + $3H_2$ and (b) Ti + $4H_2$. Hydrogen, carbon, and titanium atoms are shown in white, dark grey, and light grey, respectively.

H_2 molecule undergoes dissociative adsorption, and when dissociation occurs an additional undissociated molecule resides on top of the adsorption site. In the configurations of type (b), the on-top site is left vacant. Similar configurations were found to be stable when using SWNT support in place of C_6H_6 for the Ti catalyst [10]. The final optimized TiH_2 + $3H_2$ structure is 0.32 eV lower than Ti + $4H_2$. In the very symmetric Ti + $4H_2$ configuration, all the four molecules stay intact, with an average H–H bond distance and bond energy of 0.82 Å and 0.23 eV, respectively.

Table 4 shows a comparison between the benzene and SWNT supports. It is important to notice that the results presented in this paper agree with the hypothesis of Yildirim and Ciraci [10] about the characteristic properties of a Ti atom supported by a hexagonal-carbon-based framework and its hydrogen adsorption properties. Also, our orbital analysis substantiates the picture of the Ti–C–H_2 interaction proposed by the authors for the SWNT support. There are nonetheless important differences between the two supports. In the first instance the adsorption energy of the first dissociative H_2 addition is much reduced in the benzene support (from 0.83 eV to 0.37 eV). In addition, the dissociative addition is an activated process which suggests, according to the argument of Section 3.1, that the singlet state is stabilized in the SWNT compared to the benzene support. Furthermore, when four molecules are adsorbed, in the benzene-Ti system, one is dissociated, the others are not. In the SWNT none is dissociated. The very symmetric SWNT-Ti-$4H_2$ configuration was found to lie lower in energy by 0.10 eV than the SWNT-$TiH_2 3H_2$ [10]. It may therefore be argued that the yield of molecular H_2 adsorption in the C_6H_6-Ti system would be lower than in the SWNT (one need to recombine

Table 4: Comparison of SWNT and C_6H_6 supports for H_2 adsorption on Ti.

Support	C_6H_6	SWNT [10]
preferred configuration	$TiH_2 + 3H_2$	$Ti + 4H_2$
adsorption energy per H_2 molecule	0.23 eV	0.54 eV
first dissociative H_2 addition energy	0.37 eV	0.83 eV
$Ti + 4H_2$: H–H distance	0.82 Å	0.84 Å

one molecule when releasing hydrogen). Finally, the average Ti-H_2 adsorption energy decreases from 0.54 eV for the SWNT support to 0.23 eV for the C_6H_6. In conclusion, although the C_6H_6 support for the Ti addition qualitatively reproduces the dominant local contribution of the large gap $(8,0)$ SWNT, the different boundary conditions of the two materials, finite system in the case of C_6H_6, infinite periodic in the case of the SWNT, lead to sizable differences in the adsorption energies. The result is a favored $Ti + 4H_2$ configuration for the periodic SWNT support of the Ti atom and the more localized $TiH_2 + 3H_2$ as the favored pattern for C_6H_6. We stress that, in the $TiH_2 + 3H_2$ configuration, the first H_2 adsorption is dissociative, while the other three are not. From a material modelling viewpoint, the C_6H_6-Ti complex can be seen as an "almost converged" model system for the SWNT-Ti with respect to cluster size. Nevertheless, C_6H_6-Ti can store the same number of H_2 molecules per Ti atom, achieving a 6% weight percentage of stored hydrogen. Indeed, some electronic relationship between SWNT and C_6H_6 may be expected from the modern theory of the macroscopic polarization [30]. According to such theory, the quadratic spread of the manybody electronic wavefunction in condensed phase has an upper bound, in the presence of a finite gap E_g:

$$\lambda < \frac{\hbar^2}{2mE_g}, \tag{1}$$

where λ is the so called localization length [30], defined by a unitary operator based on a Berry phase in place of the position operator, and m is the electron mass. Qualitatively, (1) can be read as "the larger the gap, the more localized the electrons are". Indeed, $(8,0)$ SWNT is a large gap insulator nanotube, thus limiting the quadratic spread of the manybody electronic wavefunction. This means that, as normal for insulators, the interaction between Ti adatom and the SWNT may be expected to consist of a dominant local contribution from the C_6 hexagon surrounding the metal atom. When we isolate the carbon hexagon support of the Ti atom, the C_6H_6 is obtained by hydrogen passivation of the dangling bonds. Benzene can be therefore provide the simplest model system in which the local effects occurring in the large gap insulator $(8,0)$ SWNT may be represented.

4. Summary and Conclusions

We studied the adsorption of one, two, and four H_2 molecules on a single titanium atom supported on a benzene molecule. In all cases we found one H_2 molecule to adsorb dissociatively and the remaining one(s) to bind to the metal ion center through weak-charge transfer interaction. The dissociative addition was found to involve a transition from the triplet to the singlet energy surface, similar to what has been found in the adsorption of H_2 on a titanium atom supported on a $(8,0)$ SWNT. At variance with the latter, this was, however, found to be an activated process, with a barrier of 0.17 eV. The Ti-H_2-binding energy was estimated to be ~0.4 eV lower than in the SWNT. The main emphasis of this work has been on a detailed analysis of the orbital interactions responsible for the H_2 binding to Ti and for the dissociation of one H_2 molecule. Typically, the coordination of H_2 to a transition metal atom (or ion) is very weak, because the occupied $1\sigma_g$ orbital will have Pauli repulsion with occupied metal orbitals. This prevents H_2 from coming close and interacting strongly by way of its high-lying $1\sigma_u$, which could lead to breaking of the H–H bond. In the Ti-benzene system, however, the situation is different due to the small number of d electrons and due to fact that the interaction with the benzene "prepares" the Ti 3d orbitals for the interaction with H_2. Notably, the Pauli repulsion, which is embodied in the antibonding interaction of the occupied $1\sigma_g$ of H_2 with an occupied mostly $3d_{z^2}$ orbital, is relieved by the loss of the two electrons from the rising antibonding combination of the $1\sigma_g$ and $3d_{z^2}$. These electrons are transferred to an in-phase (bonding) combination of the (originally empty) Ti $3d_{xz}$ and H_2 $1\sigma_u$ orbitals, which comes down due to the stabilizing interaction. We also find that the empty Ti 4s orbital can interact favorably with H_2, which adds to the force pulling the H_2 in. In essence, Ti is specially favorable because the combination of the small number of four d electrons and the special orbital interactions with benzene lead to just the right electronic structure for easy dissociation of H_2. Our results elucidate the electronic structure reasons for the high potential of Ti on carbon supports as new and efficient materials for hydrogen storage.

Acknowledgments

This work was supported by the Netherlands Organization for Scientific Research through the ACTS Programme for Sustainable Hydrogen. Computer resources were provided by the Netherlands' Scientific Research Council (NWO) through a grant from Stichting Nationale Computerfaciliteiten (NCF). Support was also given by the WCU (World Class University) program through the Korea Science and Engineering Foundation funded by the Ministry of Education, Science and Technology of the Republic of Korea (Project no. R32-2008-000-10180-0).

References

[1] R. Coontz and B. Hanson, "Not so simple," *Science*, vol. 305, no. 5686, p. 957, 2004.

[2] A. Züttel, P. Wenger, P. Sudan, P. Mauron, and S.-I. Orimo, "Hydrogen density in nanostructured carbon, metals and complex materials," *Materials Science and Engineering B*, vol. 108, pp. 9–18, 2004.

[3] M. Felderhoff, C. Weidenthaler, R. Von Helmolt, and U. Eberle, "Hydrogen storage: the remaining scientific and technological challenges," *Physical Chemistry Chemical Physics*, vol. 9, no. 21, pp. 2643–2653, 2007.

[4] S. A. Shevlin and Z. X. Guo, "High-capacity room-temperature hydrogen storage in carbon nanotubes via defect-modulated titanium doping," *Journal of Physical Chemistry C*, vol. 112, no. 44, pp. 17456–17464, 2008.

[5] A. Bhattacharya, S. Bhattacharya, C. Majumder, and G. P. Das, "Transition-metal decoration enhanced room-temperature hydrogen storage in a defect-modulated graphene sheet," *Journal of Physical Chemistry C*, vol. 114, no. 22, pp. 10297–10301, 2010.

[6] H. Lee, M. C. Nguyen, and J. Ihm, "Titanium-functional group complexes for high-capacity hydrogen storage materials," *Solid State Communications*, vol. 146, no. 9-10, pp. 431–434, 2008.

[7] Y. Liu, L. Ren, Y. He, and H.-P. Cheng, "Titanium-decorated graphene for high-capacity hydrogen storage studied by density functional simulations," *Journal of Physics Condensed Matter*, vol. 22, no. 44, Article ID 445301, 2010.

[8] A. B. Phillips, B. S. Shivaram, and G. R. Mynenib, "Hydrogen absorption at room temperature in nanoscale titanium benzene complexes," *International Journal of Hydrogen Energy*, vol. 37, no. 2, pp. 1546–1550, 2011.

[9] P. F. Weck, T. J. D. Kumar, E. Kim, and N. Balakrishnan, "Computational study of hydrogen storage in organometallic compounds," *Journal of Chemical Physics*, vol. 126, no. 9, Article ID 094703, 2007.

[10] T. Yildirim and S. Ciraci, "Titanium-decorated carbon nanotubes as a potential high-capacity hydrogen storage medium," *Physical Review Letters*, vol. 94, no. 17, Article ID 175501, 2005.

[11] F. M. Bickelhaupt and E. J. Baerends, "Kohn-Sham density functional theory: predicting and understanding chemistry," *Reviews in Computational Chemistry*, vol. 15, pp. 1–86, 2000.

[12] ADF2005.01, SCM, Theoretical Chemistry, Vrije Universiteit Amsterdam, The Netherlands, http://www.scm.com/.

[13] E. J. Baerends, D. E. Ellis, and P. Ros, "Self-consistent molecular Hartree-Fock-Slater calculations I. The computational procedure," *Chemical Physics*, vol. 2, no. 1, pp. 41–51, 1973.

[14] C. Fonseca Guerra, J. G. Snijders, G. Te Velde, and E. J. Baerends, "Towards an order-N DFT method," *Theoretical Chemistry Accounts*, vol. 99, no. 6, pp. 391–403, 1998.

[15] N. C. Handy and A. J. Cohen, "Left-right correlation energy," *Molecular Physics*, vol. 99, pp. 403–412, 2001.

[16] C. Lee, W. Yang, and R. G. Parr, "Development of the Colle-Salvetti conelation energy formula into a functional of the electron density," *Physical Review B*, vol. 37, no. 2, pp. 785–789, 1988.

[17] M. Swart, A. R. Groenhof, A. W. Ehlers, and K. Lammertsma, "Validation of exchange-correlation functional for spin states of iron complexes," *Journal of Physical Chemistry A*, vol. 108, no. 25, pp. 5479–5483, 2004.

[18] A. J. C. W. M. Hoe and N. C. Handy, "Assessment of a new local exchange functional OPTX," *Chemical Physics Letters*, vol. 341, pp. 319–328, 2001.

[19] X. Xu and W. A. Goddard, "Assessment of Handy-Cohen optimized exchange density functional (OPTX)," *Journal of Physical Chemistry A*, vol. 108, no. 40, pp. 8495–8504, 2004.

[20] G. Hong, F. Schautz, and M. Dolg, "Ab initio study of metal-ring bonding in the bis(η^6- benzene)lanthanide and -actinide complexes $M(C_6H_6)_2$ (M = La, Ce, Nd, Gd, Tb, Lu, Th, U)," *Journal of the American Chemical Society*, vol. 121, no. 7, pp. 1502–1512, 1999.

[21] R. Pandey, B. K. Rao, P. Jena, and M. A. Blanco, "Electronic structure and properties of transition metal-benzene complexes," *Journal of the American Chemical Society*, vol. 123, no. 16, pp. 3799–3808, 2001.

[22] R. Pandey, B. K. Rao, P. Jena, and M. A. Blanco, *Journal of the American Chemical Society*, vol. 123, p. 7744, 2001.

[23] T. Kurikawa, H. Takeda, M. Hirano et al., "Electronic properties of organometallic metal-benzene complexes [Mn (benzene)m (M = Sc-Cu)]," *Organometallics*, vol. 18, no. 8, pp. 1430–1438, 1999.

[24] A. Ouhlal, A. Selmani, and A. Yelon, "Bonding in (η6-C6H6) M and (η6-C6H6) M+, M Ti, Cr, Ni, and Cu. A local spin density study," *Chemical Physics Letters*, vol. 243, no. 3-4, pp. 269–274, 1995.

[25] P. Chaquin, D. Costa, C. Lepetit, and M. Che, "Structure and bonding in a series of neutral and cationic transition metal-benzene η6 complexes [M(η6-C6H6)]n+ (M = Ti, V, Cr, Fe, Co, Ni, and Cu). Correlation of charge transfer with the bathochromic shift of the E1 ring vibration," *Journal of Physical Chemistry A*, vol. 105, no. 18, pp. 4541–4545, 2001.

[26] J. T. Lyon and L. Andrews, "Group 4 transition metal-benzene adducts: carbon ring deformation upon complexation," *Journal of Physical Chemistry A*, vol. 110, no. 25, pp. 7806–7815, 2006.

[27] R. Pandey, B. K. Rao, P. Jena, and J. M. Newsam, "Unique magnetic signature of transition metal atoms supported on benzene," *Chemical Physics Letters*, vol. 321, no. 1-2, pp. 142–150, 2000.

[28] K. Imura, H. Ohoyama, and T. Kasai, "Metal-ligand interaction of Ti-C_6H_6 complex size-selected by a 2-m long electrostatic hexapole field," *Chemical Physics Letters*, vol. 369, no. 1-2, pp. 55–59, 2003.

[29] J. T. Lyon and L. Andrews, "V, Nb, and Ta complexes with benzene in solid argon: an infrared spectroscopic and density functional study," *Journal of Physical Chemistry A*, vol. 109, no. 3, pp. 431–440, 2005.

[30] R. Resta, "Why are insulators insulating and metals conducting?" *Journal of Physics Condensed Matter*, vol. 14, no. 20, pp. R625–R656, 2002.

Hindawi Publishing Corporation
Journal of Nanotechnology
Volume 2012, Article ID 573287, 6 pages
doi:10.1155/2012/573287

Research Article

Reforming of Ethanol to Produce Hydrogen over $PtRuMg/ZrO_2$ Catalyst

Josh Y. Z. Chiou,[1] Chi-Han Wang,[1] Shih-Yi Yang,[1] Jia-Lin Bi,[1] Chia-Chieh Shen,[2,3,4] and Chen-Bin Wang[1]

[1] *Department of Chemical and Materials Engineering, Chung Cheng Institute of Technology, National Defense University, Tahsi, Taoyuan 33509, Taiwan*
[2] *Fuel Cell Center, Yuan Ze University, Taoyuan 32003, Taiwan*
[3] *Department of Mechanical Engineering, Yuan Ze University, Taoyuan 32003, Taiwan*
[4] *Graduate School of Renewable Energy and Engineering, Yuan Ze University, Taoyuan 32003, Taiwan*

Correspondence should be addressed to Chen-Bin Wang, chenbinwang@gmail.com

Received 15 March 2012; Accepted 24 April 2012

Academic Editor: Shrikrishna D. Sartale

Copyright © 2012 Josh Y. Z. Chiou et al. This is an open access article distributed under the Creative Commons Attribution License, which permits unrestricted use, distribution, and reproduction in any medium, provided the original work is properly cited.

A modified $PtRu/ZrO_2$ catalyst with Mg is evaluated for the oxidative steam reforming of ethanol (OSRE) and the steam reforming of ethanol (SRE). In order to understand the variation in the reaction mechanism on OSRE and SRE, further analysis of both fresh and used catalyst is concentrated on for TEM, TG, Raman, and TPR characterization. The results show that the OSRE reaction requires a higher temperature ($T_R \sim 390^\circ$C) to achieve 100% ethanol conversion than the SRE reaction ($T_R \sim 2500^\circ$C). The distribution of CO is minor for both reactions (< 5% for OSRE, < 1% for SRE). This demonstrates that the water gas shift (WGS) reaction is an important side-reaction in the reforming of ethanol to produce H_2 and CO_2. A comparison of the temperature of WGS (T_{WGS}) shows it is lower for the SRE reaction ($T_{WGS} \sim 250^\circ$C for SRE, ~340°C for OSRE).

1. Introduction

The prospect of global energy shortages as well as increasingly stringent emission regulations has stimulated interest in renewable energies. Production of hydrogen from renewable sources derived from agricultural or other waste streams offers the possibility of lower or even no net greenhouse gas emissions [1, 2]. Among the candidates for hydrogen production, ethanol produced by the fermentation of biomass offers many advantages, such as low toxicity, high biodegradability, and easy transport [3–5]; thus, the reforming of ethanol is seen as a promising method for hydrogen production from renewable resource [6, 7]. Hydrogen can be produced from ethanol through different reforming processes, for example, steam reforming of ethanol (SRE), partial oxidation of ethanol (POE), and oxidative steam reforming of ethanol (OSRE). Moreover, a high yield of hydrogen can be obtained from the SRE reaction [4–14].

The nature of the metal and its support strongly affect both stability and products distribution [5, 15]. In view of the ZrO_2-supported system, noble metal catalysts such as Pt and Ru are well known for their high catalytic activities, which have been extensively investigated. The size-selective capability of Pt/ZrO_2 catalysts on the catalytic decomposition of alcohol for the production of hydrogen was reported by Cuenya's group [7, 16]. However, this catalyst deactivated at high temperatures due to carbon deposition. De Lima et al. [17] reported that the side-products of acetaldehyde and ethane were favored on Pt/ZrO_2 in the SRE. Relatively low reaction temperatures around 100 to 200°C in the POE and OSRE over a Pt/ZrO_2 and $PtRu/ZrO_2$ catalysts were reported by our previous studies [18–21], and 300°C was reported by Mattos and Noronha [22] in the POE reaction. The main problem found when using these catalysts is deactivation by sintering and carbon deposition. The use of basic oxides as supports and the addition of metal species (Li, Na, K, and Cu, etc.) have

been found to improve catalytic performance and overcome the disadvantages [9, 23–25]. Recently, Carrero et al. [26] reported the effect of alkaline earth metals over Cu-Ni/SiO_2 catalysts where a high hydrogen selectivity was obtained with Mg, while the incorporation of Ca reduced coke formation.

Therefore, the main objective of this paper is to study PtRuMg/ZrO_2 catalyst for the SRE and OSRE reactions to produce hydrogen at a temperature lower than 300°C with higher ethanol conversion (X_{EtOH}), hydrogen yield (Y_{H_2}), and lower CO distribution. The expectation is that the catalytic activity and stability against the coke deposition of the PtRuMg/ZrO_2 catalyst on the reforming of ethanol could be enhanced. The characterization of fresh and used catalysts was analyzed by TEM, TG, Raman, and TPR characterization.

2. Experimental

2.1. Catalyst Preparation. A sol-gel method was used for the preparation of the ZrO_2 support using $Zr[O(CH_2)_3CH_3]_4$ (Strem) as the precursor. The PtRuMg/ZrO_2 catalyst was prepared by the method of sequent incipient wetness impregnation using H_2PtCl_6 and $RuCl_3$ as precursors (1.5 wt% for each component) first to disperse on the ZrO_2. After drying at 110°C and calcination at 400°C for 4 h, 1.0 wt% of $Mg(NO_3)_2 \cdot 6H_2O$ was incipient sequentially. After drying at 110°C, the prepared sample was crashed to 60 ~ 80 mesh and stored as fresh catalyst (labeled as PtRuMg/ZrO_2).

2.2. Catalyst Characterization. Transmission electron micrographs (TEMs) were taken on a PHILIPS (CM-200) microscope at an accelerated voltage of 200 kV. Thermal gravimetric analysis was carried out using a Seiko SSC5000 TG system. The rate of heating was maintained at 10°C·min^{-1}. The measurement was carried from RT to 1000°C under air flowing with a rate of 100 mL·min^{-1}. The measurements of the Raman spectroscopy were recorded using a Nicolet Almega XR Dispersive Raman spectrometer. The spectra were collected between 500 and 2000 cm^{-1}, using the beam of a diode laser (780 nm), with the sample exposed to the air under ambient conditions. Reduction behavior was studied by temperature-programmed reduction (TPR). A sample of about 50 mg was introduced a flow of 10% H_2/N_2 gas mixture at a flow rate of 10 mL·min^{-1}. During TPR, the temperature was increased at 7°C·min^{-1} from room temperature to 900°C.

2.3. Catalytic Activity Measurement. Catalytic activities of the prepared sample towards the SRE and OSRE reactions were tested in a fixed-bed flow reactor at atmospheric pressure. Catalyst in the amount of 100 mg was placed in a 4 mm i.d. quartz tubular reactor and held by glass-wool plugs. Before the reaction, the catalyst was activated by reduction with hydrogen at 300°C for 3 h. The gas hourly space velocity (GHSV) was maintained at 22,000 h^{-1}, and the H_2O/EtOH molar ratio was 13 (H_2O : EtOH = 80 : 20 by volume) for the SRE reaction; while the GHSV was maintained at 56,000 h^{-1}, the O_2/EtOH molar ratio was 0.26, and the H_2O/EtOH molar ratio was 4.86 for the OSRE reaction. A 5 h time-on-stream tests were maintained at each measured temperature. The analysis of the reactants and all reaction products was carried out online by gas chromatography, with columns of Porapak Q and Molecular Sieve 5A for separation. The evaluation of the catalytic activity depended on the conversion, products distribution, and the yield of hydrogen:

$$X_{EtOH} = \frac{(n_{EtOH\text{-}in} - n_{EtOH\text{-}out})}{n_{EtOH\text{-}in}} \times 100\%,$$
$$Y_{H_2} = \frac{n_{H_2\text{-}out}}{n_{EtOH\text{-}in}}, \quad (1)$$
$$S_i = \frac{nP_i}{n \sum P_i} \times 100\%,$$

where X_{EtOH} is the conversion of ethanol, Y_{H_2} is the yield of hydrogen, S_i is the distribution of different products, P_i is the different products, and n is the amounts of moles.

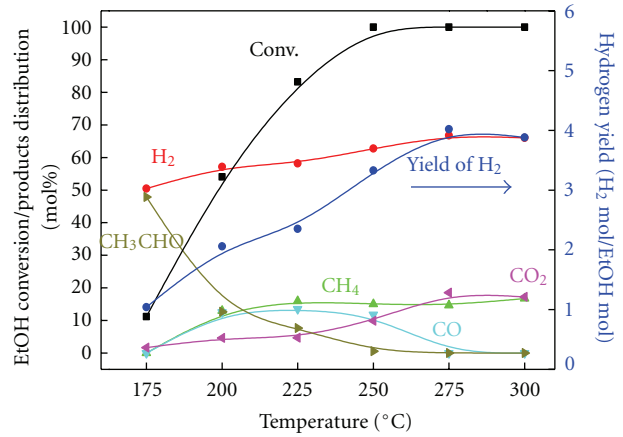

Figure 1: Catalytic performance in the SRE reaction over PtRuMg/ZrO_2 catalyst.

3. Results and Discussion

3.1. Catalytic Evaluation. Figure 1 illustrates the X_{EtOH}, products distribution (water excluded), and Y_{H_2} from SRE with an H_2O/EtOH molar ratio of 13 over the PtRuMg/ZrO_2 catalyst between 175 and 300°C. About 1 h to reach the steady state and the recorded date was 5 h time-on-stream tests at each reaction temperature. The concentration of hydrogen increased progressively with increases in temperature (T_R). The detailed proposed pathway was shown in the Scheme 1. Below 200°C, the main product besides hydrogen was acetaldehyde, thus indicating that it behaved as a dehydrogenation of ethanol, and then acetaldehyde decomposition into methane and CO with increasing temperature. This indicated that both platinum and ruthenium had a stronger

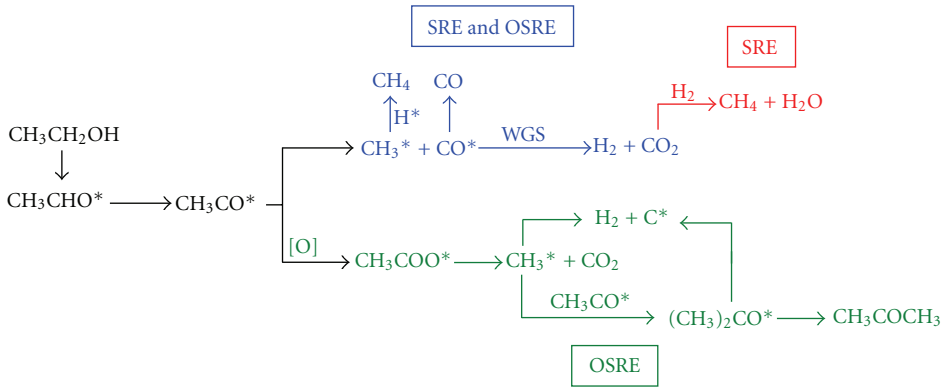

Scheme 1: Reaction routes of SRE and OSRE over PtRuMg/ZrO_2 catalyst.

capacity for breaking the C–C bond in the reforming of ethanol

$$C_2H_5OH \longrightarrow CH_3CHO + H_2$$
$$CH_3CHO \longrightarrow CH_4 + CO. \quad (2)$$

At higher temperatures ($T_R > 225^\circ C$), concentrations of CO_2 up to 18% accompanied the decreasing of CO to 0.2%. At the same time, the concentration of methane through the decomposition of acetaldehyde was significant. This indicated that the water-gas shift (WGS) reaction occurred at a lower temperature than that of the cobalt oxide [12] and the PtRu/ZrO_2 catalyst [20]. This showed that the addition of magnesium improved the reforming activities and enhanced the WGS reaction at lower temperatures

$$CO + H_2O \longrightarrow H_2 + CO_2. \quad (3)$$

When the T_R increased to 280°C, the amount of CH_4 side-product increased slightly to approach 16% and decreased the yield of hydrogen since the reversed water-gas shift reaction (RWGS) occurred. The maximum Y_{H_2} approached 4.0 around 275°C for the SRE reaction

$$CO_2 + 4H_2 \longrightarrow CH_4 + 2H_2O. \quad (4)$$

Figure 2 displays the X_{EtOH}, products distribution (water excluded), and Y_{H_2} from OSRE with an EtOH/H_2O/O_2 at a molar ratio of 1 : 4.86 : 0.26 over a PtRuMg/ZrO_2 catalyst between 250 and 420°C. As compared with the SRE reaction, there were significant differences in the different reactions. The SRE reaction preceded complete conversion of the ethanol at 250°C, while there was only 75% conversion at this temperature and full ethanol conversion exceeded 390°C for the OSRE reaction. The temperature for the decomposition of acetaldehyde (D_T) showed that the easy cracking promoted the formation of hydrogen. The D_T on the SRE reaction approached 200°C, and above 250°C for the OSRE reaction. The acetaldehyde disappeared at 275°C for the SRE reaction, and at 420°C for the OSRE reaction. A comparison of the temperature of WGS (T_{WGS}) showed that it was lower for the SRE reaction ($T_{WGS} \sim 250^\circ C$ for SRE, ~340°C for OSRE). The distribution of CO was

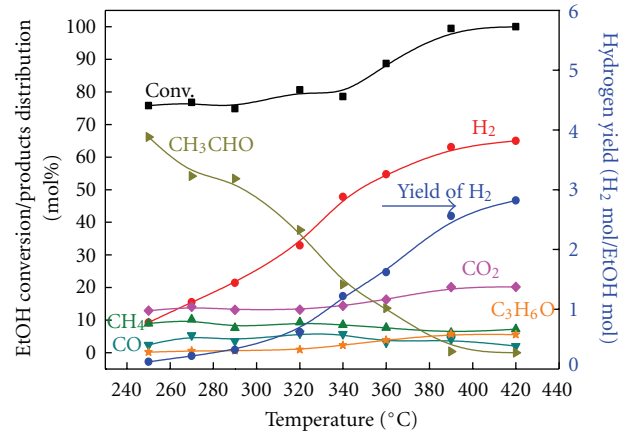

Figure 2: Catalytic performances in the OSRE reaction over PtRuMg/ZrO_2 catalyst.

minor for both reactions (<5% for OSRE, <0.5% for SRE). Besides the main products of H_2 and CO_2, the decreasing of acetaldehyde accompanied with the trace amounts of acetone was produced through the condensation of acetaldehyde (showed in the Scheme 1) at $T_R > 340^\circ C$. At a further temperature increase, the acetone was still detected. This clearly influenced the yield of hydrogen and also, possibly, the coke deposition. The maximum Y_{H_2} only approached 2.8 around 420°C for the OSRE reaction.

3.2. Characterization of Used Catalyst. The design of a stable and applicable catalyst is one of the most important issues in the production of hydrogen from ethanol. The significant deactivation reported for hydrogen production from ethanol reforming is usually attributed to carbon formation and sintering of active metals, which is strongly influenced by the nature of the support, catalyst, and reaction conditions (especially temperature and H_2O/EtOH/O_2 ratio) [9, 27–29]. In order to obtain more information about the behavior of the used catalyst, TEM, TG, Raman, and TPR characterizations were pursued for the samples after the SRE and OSRE catalytic tests.

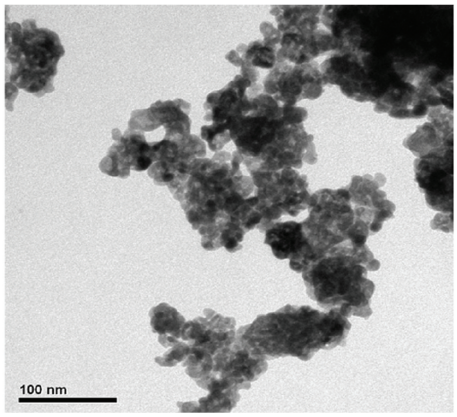

(a)

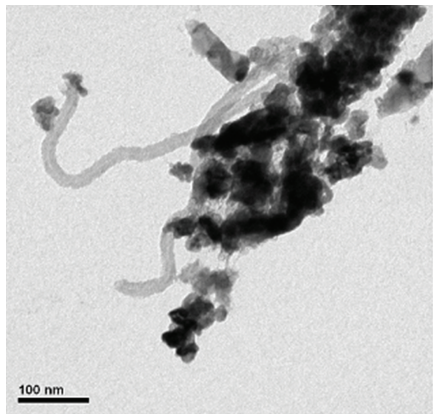

(b)

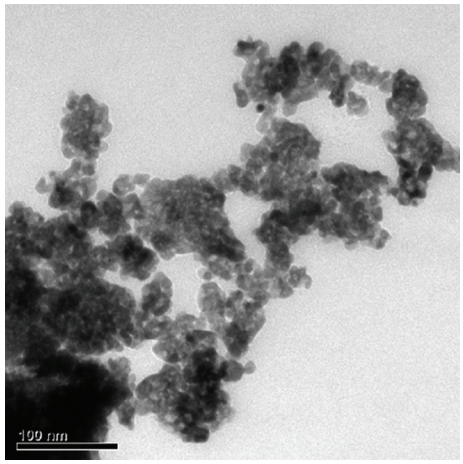

(c)

Figure 3: TEM images of fresh and used catalysts: (a) fresh, (b) after OSRE reaction, and (c) after SRE reaction.

Figure 3 shows the TEM micrographs of both fresh and used catalysts. A comparison with the fresh sample (see Figure 3(a)) showed an apparent deposition of coke on the used catalyst after the OSRE reaction (see Figure 3(b)). There was no obvious coke formation observed after the SRE reaction (see Figure 3(c)). The specific weight loss of combustion of

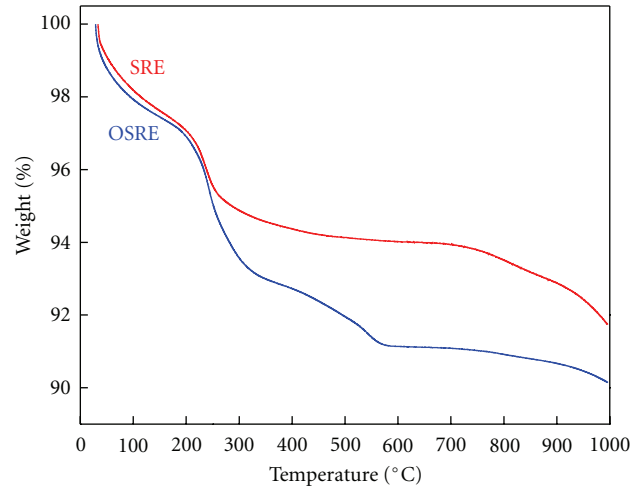

Figure 4: TG curves of used catalyst after SRE and OSRE reaction.

adsorbed C_1 species (200~300°C) and coke (400~600°C) on the catalyst surface was obtained from the TG results (see Figure 4). Since the addition of magnesium modified the catalyst becomes slightly base which may be adsorbed C_1 species after the reforming reaction. It was apparent that only after the OSRE reaction was the combustion of coke observed. Furthermore, the Raman spectra (see Figure 5) of the used catalyst after the SRE reaction differed from the OSRE reaction. There were two bands centered at 1320 (D-band) and 1590 (G-band) cm^{-1}, characteristic of poorly ordered carbon deposition [30], observed after the OSRE reaction but not after the SRE reaction. This result indicated that the coke formed through the OSRE reaction. Also, the evidence of coke formation can be demonstrated by the TPR analysis. Figure 6 shows the TPR profiles of the used catalyst after the SRE and OSRE reactions. Two reduction regions can be distinguished: one region for the adsorbed C_1 species (around 298°C) and the other region for coke (around 584°C), with the broad signal coming from the methanation of deposited carbon [8]

$$C + 2H_2 \longrightarrow CH_4. \quad (5)$$

From the characterization of the used catalyst, we observed a more pronounced coke formation in the OSRE reaction and confirmed that the designed $PtRuMg/ZrO_2$ catalyst was a suitable application on the SRE reaction.

4. Conclusions

A novel and high performance $PtRuMg/ZrO_2$ catalyst had been designed and applied on the SRE and OSRE reaction to produce hydrogen at low temperature. The results showed that the distribution of CO was minor for both reactions (<5% for OSRE, <1% for SRE). The OSRE reaction required a higher temperature ($T_R \sim 390°C$) to achieve 100% ethanol conversion than the SRE reaction ($T_R \sim 250°C$). Also the temperature of WGS accompanying the OSRE reaction was higher ($T_{WGS} \sim 340°C$) than that of the SRE reaction

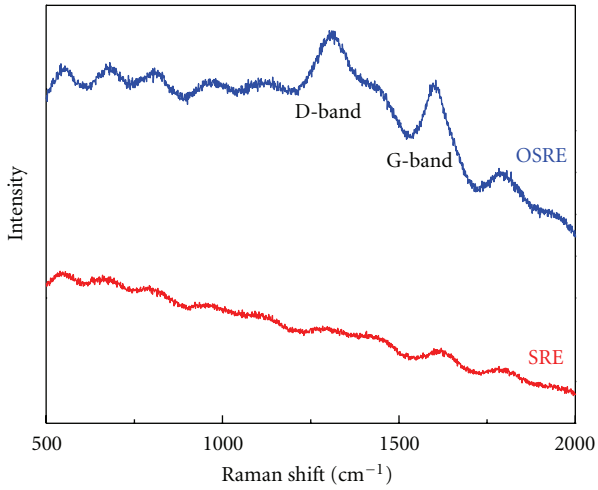

FIGURE 5: Raman spectra of used catalyst after SRE and OSRE reaction.

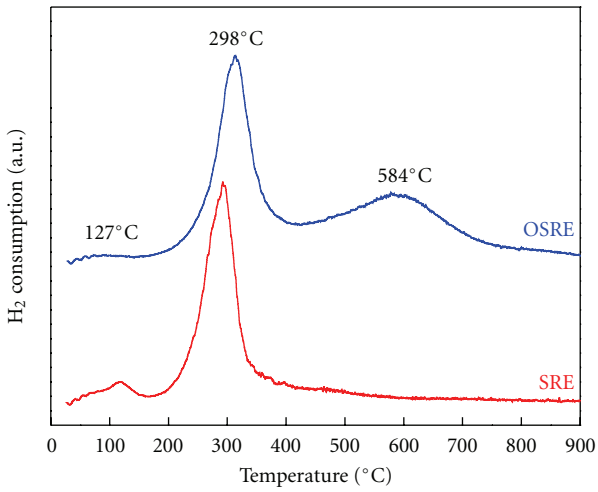

FIGURE 6: TPR profiles of used catalyst after SRE and OSRE reaction.

(T_{WGS} ~ 250°C). A more pronounced coke formation was observed in the OSRE reaction. In considering the catalytic stability against the coke deposition, application of PtRuMg/ZrO_2 catalyst on the SRE reaction is suitable.

Acknowledgment

The authors are pleased to acknowledge the financial support for this study by the National Science Council of the Republic of China under contract nos. of NSC 99-2113-M-606-001-MY3, and NSC 101-2623-E-155-001-ET.

References

[1] A. E. Farrell, R. J. Plevin, B. T. Turner, A. D. Jones, M. O'Hare, and D. M. Kammen, "Ethanol can contribute to energy and environmental goals," *Science*, vol. 311, no. 5760, pp. 506–508, 2006.

[2] B. E. Dale and D. Pimentel, "Two views on whether corn ethanol and, eventually, ethanol from cellulosic biomass will efficiently deliver national energy security," *Chemical & Engineering News*, vol. 85, no. 51, pp. 12–16, 2007.

[3] Y. Liu, T. Hayakawa, T. Tsunoda et al., "Steam reforming of methanol over Cu/CeO_2 catalysts studied in comparison with Cu/ZnO and Cu/Zn(Al)O catalysts," *Topics in Catalysis*, vol. 22, no. 3-4, pp. 205–213, 2003.

[4] P. D. Vaidya and A. E. Rodrigues, "Insight into steam reforming of ethanol to produce hydrogen for fuel cells," *Chemical Engineering Journal*, vol. 117, no. 1, pp. 39–49, 2006.

[5] A. Haryanto, S. Fernando, N. Murali, and S. Adhikari, "Current status of hydrogen production techniques by steam reforming of ethanol: a review," *Energy and Fuels*, vol. 19, no. 5, pp. 2098–2106, 2005.

[6] H. Muroyama, R. Nakase, T. Matsui, and K. Eguchi, "Ethanol steam reforming over Ni-based spinel oxide," *International Journal of Hydrogen Energy*, vol. 35, no. 4, pp. 1575–1581, 2010.

[7] M. Ni, D. Y. C. Leung, and M. K. H. Leung, "A review on reforming bio-ethanol for hydrogen production," *International Journal of Hydrogen Energy*, vol. 32, no. 15, pp. 3238–3247, 2007.

[8] J. Llorca, N. Homs, J. Sales, and P. R. de la Piscina, "Efficient production of hydrogen over supported cobalt catalysts from ethanol steam reforming," *Journal of Catalysis*, vol. 209, no. 2, pp. 306–317, 2002.

[9] A. N. Fatsikostas and X. E. Verykios, "Reaction network of steam reforming of ethanol over Ni-based catalysts," *Journal of Catalysis*, vol. 225, no. 2, pp. 439–452, 2004.

[10] P. K. Cheekatamarla and C. M. Finnerty, "Reforming catalysts for hydrogen generation in fuel cell applications," *Journal of Power Sources*, vol. 160, no. 1, pp. 490–499, 2006.

[11] F. Frusteri, S. Freni, L. Spadaro et al., "H_2 production for MC fuel cell by steam reforming of ethanol over MgO supported Pd, Rh, Ni and Co catalysts," *Catalysis Communications*, vol. 5, no. 10, pp. 611–615, 2004.

[12] C. B. Wang, C. C. Lee, J. L. Bi, J. Y. Siang, J. Y. Liu, and C. T. Yeh, "Study on the steam reforming of ethanol over cobalt oxides," *Catalysis Today*, vol. 146, no. 1-2, pp. 76–81, 2009.

[13] J. Y. Siang, C. C. Lee, C. H. Wang et al., "Hydrogen production from steam reforming of ethanol using a ceria-supported iridium catalyst: effect of different ceria supports," *International Journal of Hydrogen Energy*, vol. 35, no. 8, pp. 3456–3462, 2010.

[14] J. Y. Liu, C. C. Lee, C. H. Wang, C. T. Yeh, and C. B. Wang, "Application of nickel-lanthanum composite oxide on the steam reforming of ethanol to produce hydrogen," *International Journal of Hydrogen Energy*, vol. 35, no. 9, pp. 4069–4075, 2010.

[15] P. D. Vaidya and A. E. Rodrigues, "Kinetics of steam reforming of ethanol over a Ru/Al_2O_3 catalyst," *Industrial & Engineering Chemistry Research*, vol. 45, no. 19, pp. 6614–6618, 2006.

[16] J. R. Croy, S. Mostafa, J. Liu, Y. Sohn, H. Heinrich, and B. R. Cuenya, "Support dependence of MeOH decomposition over size-selected Pt nanoparticles," *Catalysis Letters*, vol. 119, no. 3-4, pp. 209–216, 2007.

[17] S. M. de Lima, A. M. Silva, I. O. da Cruz et al., "H_2 production through steam reforming of ethanol over Pt/ZrO_2, Pt/CeO_2 and Pt/$CeZrO_2$ catalysts," *Catalysis Today*, vol. 138, no. 3-4, pp. 162–168, 2008.

[18] J. L. Bi, S. N. Hsu, C. T. Yeh, and C. B. Wang, "Low-temperature mild partial oxidation of ethanol over supported

platinum catalysts," *Catalysis Today*, vol. 129, no. 3, pp. 330–335, 2008.

[19] S. N. Hsu, J. L. Bi, W. F. Wang, C. T. Yeh, and C. B. Wang, "Low-temperature partial oxidation of ethanol over supported platinum catalysts for hydrogen production," *International Journal of Hydrogen Energy*, vol. 33, no. 2, pp. 693–699, 2008.

[20] J. L. Bi, Y. Y. Hong, C. C. Lee, C. T. Yeh, and C. B. Wang, "Novel zirconia-supported catalysts for low-temperature oxidative steam reforming of ethanol," *Catalysis Today*, vol. 129, no. 3-4, pp. 322–329, 2007.

[21] C. H. Wang, K. F. Ho, and J. Y. Z. Chiou, "Oxidative steam reforming of ethanol over $PtRu/ZrO_2$ catalysts modified with sodium and magnesium," *Catalysis Communications*, vol. 12, no. 10, pp. 854–858, 2011.

[22] L. V. Mattos and F. B. Noronha, "Partial oxidation of ethanol on supported Pt catalysts," *Journal of Power Sources*, vol. 145, no. 1, pp. 10–15, 2005.

[23] A. J. Vizcaino, A. Carrero, and J. A. Calles, "Hydrogen production by ethanol steam reforming over Cu-Ni supported catalysts," *International Journal of Hydrogen Energy*, vol. 32, no. 10-11, pp. 1450–1461, 2007.

[24] F. Frusteri, S. Freni, V. Chiodo et al., "Steam reforming of bio-ethanol on alkali-doped Ni/MgO catalysts: hydrogen production for MC fuel cell," *Applied Catalysis A*, vol. 270, no. 1-2, pp. 1–7, 2004.

[25] J. Sun, X. P. Qiu, F. Wu, and W. T. Zhu, "H_2 from steamreforming of ethanol at low temperature over Ni/Y_2O_3, Ni/La_2O_3 and Ni/Al_2O_3 catalysts for fuel-cell application," *International Journal of Hydrogen Energy*, vol. 30, no. 4, pp. 437–445, 2005.

[26] A. Carrero, J. A. Calles, and A. J. Vizcaino, "Effect of Mg and Ca addition on coke deposition over $Cu\text{-}Ni/SiO_2$ catalysts for ethanol steam reforming," *Chemical Engineering Journal*, vol. 163, no. 3, pp. 395–402, 2010.

[27] A. N. Fatsikostas, D. I. Kondarides, and X. E. Verykios, "Production of hydrogen for fuel cells by reformation of biomass-derived ethanol," *Catalysis Today*, vol. 75, no. 1–4, pp. 145–155, 2002.

[28] L. F. de Mello, F. B. Noronha, and M. Schmal, "NO reduction with ethanol on $Pd\text{-}Mo/Al_2O_3$ catalysts," *Journal of Catalysis*, vol. 220, no. 2, pp. 358–371, 2003.

[29] M. A. Goula, S. K. Kontou, and P. E. Tsiakaras, "Hydrogen production by ethanol steam reforming over a commercial $Pd/\gamma\text{-}Al_2O_3$ catalyst," *Applied Catalysis B*, vol. 49, no. 2, pp. 135–144, 2004.

[30] P. Lespade, A. Marchand, M. Couzi, and F. Cruege, "Caracterisation de materiaux carbones par microspectrometrie Raman," *Carbon*, vol. 22, no. 4-5, pp. 375–385, 1984.

Hindawi Publishing Corporation
Journal of Nanotechnology
Volume 2012, Article ID 439531, 5 pages
doi:10.1155/2012/439531

Research Article

Nanotechnology Role for the Production of Clean Fuel E-85 and Petrochemical Raw Materials

Iskander K. Basily,[1] Amira L. Shafik,[1] Ali A. Sarhan,[1] and Mona B. Mohamed[2]

[1] *Department of Chemistry, Faculty of Science, Mansoura University, Mansoura 35516, Egypt*
[2] *NILES, Department of Biotechnology, Cairo University, Cairo 11562, Egypt*

Correspondence should be addressed to Iskander K. Basily, iskanderkamel2@hotmail.com

Received 21 January 2012; Revised 14 April 2012; Accepted 17 April 2012

Academic Editor: Vaishali R. Shinde

Copyright © 2012 Iskander K. Basily et al. This is an open access article distributed under the Creative Commons Attribution License, which permits unrestricted use, distribution, and reproduction in any medium, provided the original work is properly cited.

There have been a number of substantive technical changes that can be described as revolutionary process and evolutionary process. One of these approaches is the use of nanotechnology in the two-stage pyrolysis of petroleum residues of the heavy distillates separated from the Arabian crude oil. Two-stage catalytic pyrolysis technique proved to be an excellent method for the production of unsaturated hydrocarbons (which easily can be converted to alcohol, by addition of H_2O, for the production of E-85, i.e., clean fuel) regardless the type of feed stocks used. Basically, the catalysts are arranged into three large groups; amorphous and crystalline alumino-silicates, alkaline or alkaline earth alumino compounds, and different metal oxides on different catalyst carriers such as Zeolites. The high yield of ethylene (30–40%) brought by different catalysts at temperatures of 700–750°C appear to justify the intensive research work in this field.

1. Introduction

Upgrading of heavy ends for the manufacture of olefins is the main aim of the refineries today. Production of fuel-grade distillate from petroleum residues is a profitable operation for refineries provided that they have necessary technology available. Any processing to convert heavy ends into refined distillates should somewhere include a hydrogen addition step, heteroatom removal step. However, in the two-stage pyrolysis technique, the feed stock can be used without any pretreatment [1–8], regardless of the type of the feed stock used (contaminants are left as pyrolysis residue at the first stage) and the pyrolyzate as then contains high percentage of ethylene and propylene (≈37 wt. % unsaturated) using the normal catalyst. However, when we used the nanocatalyst in the two-stage pyrolysis technique, the unsaturated hydrocarbons reaches ≈85 wt. % in the pyrolyzate yield (i.e., the creative technology is the best protection against uncertainties of the future). Nowadays, scientists do their best to find new sources for clean energy (as the uses of alcohol as it is or as a blend with gasoline 15 vol. % to form E-85).

2. Aim of the Present Work

Obtain unsaturated hydrocarbons from petroleum residues with the help of different types of nanocatalyst and computer program to optimize the pyrolysis parameters of the two-stage reactor.

3. Experimental

An experimental study has been carried out of the effectiveness of some catalysts on the yield and product distribution of the two-stage pyrolysis process. Two topics are discussed.

The first topic is the effectiveness of CaO catalyst on the yield and product distribution of the two-stage pyrolysis of

gas-oil, with the intention of the producing ethylene and propylene.

The second topic deals with the two-stage catalytic pyrolysis of light distillates separated from Egyptian crude using nanocatalyst. These catalysts were prepared by different shapes.

Bimetallic colloids can be prepared by simultaneous reduction of two kinds of metal ions with or without the protecting agent or by successive reduction of one metal nuclei of the other.

4. Materials

(A) The feed-stock fraction is the gas-oil supplied by Cairo-Petroleum-Refining and used as it is without pretreatment.

(B) The (CaO) catalyst used has been supplied by "Union Carbide"—Tarrytown Technical Center—and composed of Ca^{++} (30-511) Lot number 3358-16, however, the gold nanocatalyst supported on the CaO catalyst and used as powder was supplied by "National Institute Laser Science" (NILES).

5. Procedure

The pyrolysis has been carried out using a batch-type apparatus. A quartz reactor tube (22 mm, 12 mm I'd) was placed horizontally through two separate electric furnaces, and the temperature was controlled by adjusting the electric current of the heaters. Quartz boat containing 0.2 gm of the feed-stock (Gas-Oil) with 1.5 gm of nickel sheet was inserted into the lower -temperature zone with the help of a quartz tube through which argon gas was allowed to flow. The cracked oil and gases produced at the first stage (200–400°C ±5°C) were carried to the second stage (325–500°C ±5°C) by the argon gas to undergo subsequent pyrolysis under the influence of the catalysts bed used.

A fixed catalyst bed was placed in the second stage by packing the catalyst in layers supported by a quartz wool plug. After a lapse of certain reaction time, the quartz boat is removed, cooled, and weighed to determine the amount of the pyrolyzed residue. The produced gases were collected in a gas burette. The optimum contact tine of the first stage from different experiments was found to be 15 min (the contact time of the feed-stock with the nickel catalyst in the first stage, low-temperature reaction zone). The second stage contact time varied (2.6–3.4 sec).

The pyrolyzate hydrocarbons were analyzed using Gas Chromatography (GC-mass): Agilent 6890 plus Gas chromatograph under the following conditions:

Detector: FID 250°C

Injector: split 1 : 20 250°C, 0.5 mL

Carrier: Ar 3 mL/min.

5°C/min

Oven: 50 → 200.

6. Result and Discussion

The influence of the first stage temperature (T_1) in the distribution of hydrocarbon pyrolyzate using gold (Au) nanoparticles as spheres supported on (Cao) catalyst has been illustrated in Figure 1, and the mathematical expressions for the yield of unsaturated hydrocarbons were given for each of the following:

$$\begin{aligned} Y \text{ ethylene} = {} & -4e^{-7}(T_1)^4 + 0.0005(T_1)^3 \\ & - 0.2(T_1)^2 + 34.367(T_1) - 2169.1, \\ Y \text{ propylene} = {} & -4e^{-9}(T_1)^5 + 6e^{-6}(T_1)^4 \\ & - 0.0034(T_1)^3 + 0.9037(T_1)^2 \\ & - 117.27(T_1) + 5916, \\ Y \text{ total-unsaturated} = {} & -5e^{-7}(T_1)^4 + 0.0005(T_1)^3 \\ & - 0.2225(T_1)^2 + 40.974(T_1) \\ & - 2677.3. \end{aligned} \tag{1}$$

The influence of the second stage temperature (T_2) on the distribution of hydrocarbon pyrolyzate using the gold (Au) nanoparticles as spheres supported on the CaO catalyst has been illustrated in Figure 2, and the mathematical expressions for the yield of unsaturated hydrocarbons were given for each of the following:

$$\begin{aligned} Y \text{ ethylene} = {} & 1e^{-6}(T_2)^4 - 0.0017(T_2)^3 \\ & + 0.9937(T_2)^2 - 253.68(T_2) + 24348, \\ Y \text{ propylene} = {} & -1e^{-6}(T_2)^3 + 0.0012(T_2)^2 \\ & - 0.4054(T_2) + 43.027, \\ Y \text{ total-unsaturated} = {} & 1e^{-6}(T_2)^4 - 0.0018(T_2)^3 \\ & + 1.0424(T_2)^2 - 279.97(T_2) + 26788. \end{aligned} \tag{2}$$

The influence of the first stage contact time (τ_1) on the distribution of hydrocarbon pyrolyzate using the gold (Au) nanoparticles as spheres supported on the CaO catalyst has been illustrated in Figure 3, and the mathematical expressions for the yield of unsaturated hydrocarbons were given for each of the following:

$$\begin{aligned} Y \text{ ethylene} = {} & -0.011(\tau_1)^4 + 0.615(\tau_1)^3 \\ & - 11.578(\tau_1)^2 + 87.74(\tau_1) - 175.55, \end{aligned}$$

$$
\begin{aligned}
Y \text{ propylene} &= 0.0116(\tau_1)^3 - 0.557(\tau_1)^2 \\
&\quad + 7.887(\tau_1) - 26.976, \\
Y \text{ total-unsaturated} &= -0.011(\tau_1)^4 + 0.6034(\tau_1)^3 \\
&\quad - 11.69(\tau_1)^2 + 92.239(\tau_1) - 193.94.
\end{aligned} \tag{3}
$$

The influence of the second stage contact time (τ_2) on the distribution of hydrocarbon pyrolyzate using the gold (Au) nanoparticles as spheres supported on the CaO catalyst has been illustrated in Figure 4, and the mathematical expressions for the yield of unsaturated hydrocarbons were given for each of the following:

$$
\begin{aligned}
Y \text{ ethylene} &= 7492.2(\tau_2)^4 - 90324(\tau_2)^3 \\
&\quad + 407054(\tau_2)^2 - 812743(\tau_2) \\
&\quad + 60662, \\
Y \text{ propylene} &= 111.09(\tau_2)^3 - 1057.5(\tau_2)^2 \\
&\quad + 3338(\tau_2) - 3491.6, \\
Y \text{ total-unsaturated} &= 9068.2(\tau_2)^4 - 109393(\tau_2)^3 \\
&\quad + 493322(\tau_2)^2 - 985682(\tau_2) \\
&\quad + 736288.
\end{aligned} \tag{4}
$$

The influence of the catalyst to oil (r) ratio on the distribution of hydrocarbons pyrolyzate using the gold (Au) nanoparticles as spheres supported on the CaO catalyst has been illustrated in Figure 5, and the mathematical expressions for the yield of unsaturated hydrocarbons were given for each of the following:

$$
\begin{aligned}
Y \text{ ethylene} &= -0.072(r)4 + 2.9078(r)^3 \\
&\quad - 39.63(r)^2 + 205.94(r) - 300.35, \\
Y \text{ propylene} &= -0.0089(r)^4 + 0.3664(r)^3 \\
&\quad - 4.9547(r)^2 + 25.432(r) - 34.671, \\
Y \text{ total unsaturated} &= -0.0769(r)^4 + 3.1102(r)^3 \\
&\quad - 42.123(r)^2 + 218.53(r) - 311.88.
\end{aligned} \tag{5}
$$

Studying the effect of shape of the gold (Au) between (rods, prisms, and spheres) [9–20] nanoparticles supported on CaO catalyst on the distribution of hydrocarbon pyrolyzate produced from two-stage catalytic pyrolysis of the feed stock fraction separated from Egyptian crude oil under the same optimum conditions at which the maximum yield of unsaturated hydrocarbons produced from two-stage catalytic pyrolysis of feed stock fraction using Au-nanoparticles; $T_1 = 200^\circ$C, $T_2 = 400^\circ$C, $\tau_1 = 10$ min., $\tau_2 = 3$ sec., cat/oil ratio (r) = 1 : 15, it was found that the rod shape nanoparticles have the highest catalytic activity than nanoprisms and nanospheres, that may be due to the presence of different crystalline facets (110) which is absent in nanoshheres and nanoprisms, this facet has higher catalytic properties than others and give the highest yield for total unsaturated hydrocarbons (85.22 wt. %), mainly ethylene (79.41 wt. %) and propylene (5.8 wt. %), while the total unsaturated hydrocarbons using nanoprisms yield 62.28 wt. %, mainly ethylene (51.75 wt. %), and propylene

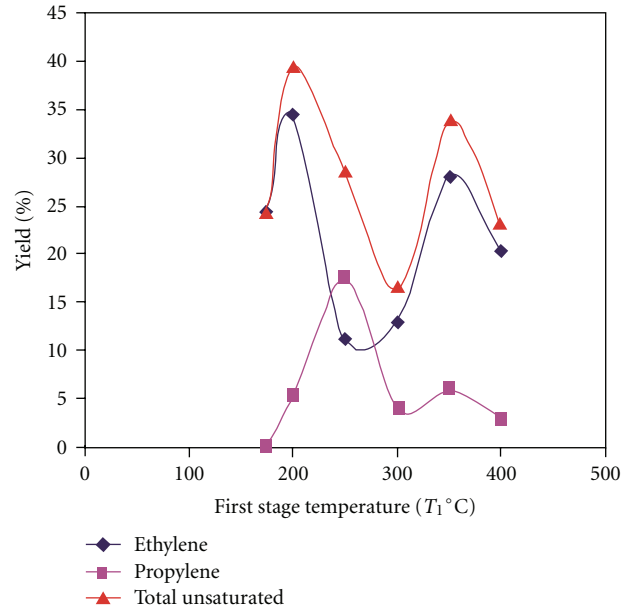

Figure 1: Influence of the first stage temperature (T_1) on the yield of unsaturated hydrocarbons.

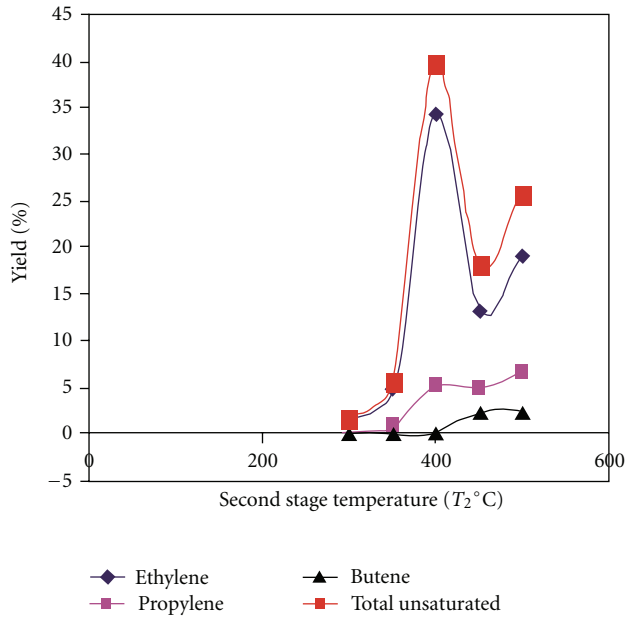

Figure 2: Influence of the second stage temperature (T_2) on the yield of unsaturated hydrocarbons.

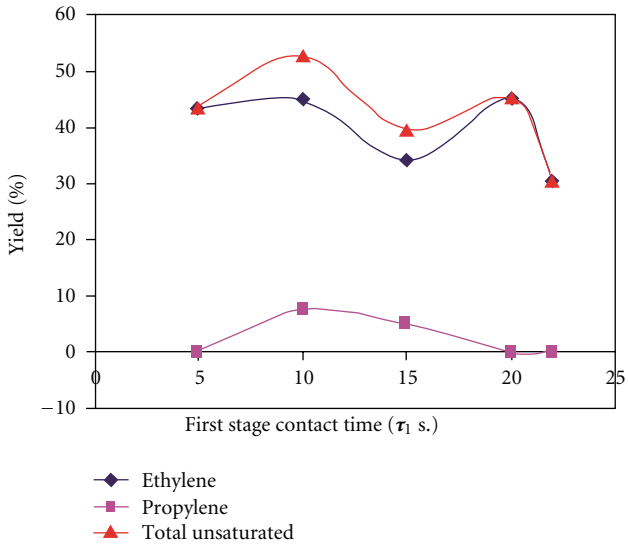

FIGURE 3: Influence of the first stage contact time (τ_1) on the yield of unsaturated hydrocarbons.

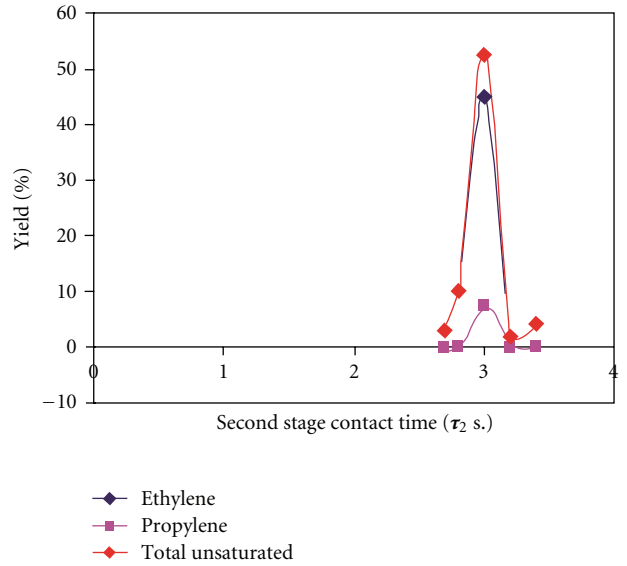

FIGURE 4: Influence of the second stage contact time (τ_2) on the yield of unsaturated hydrocarbons.

(10.53 wt. %). This confirms that the nanocatalyst with the rod shape is the optimum condition for ethylene production.

Studying the effect of using Pd-Au core-shell and alloy [17, 20–31], supported on the Cao catalyst on the distribution of the hydrocarbon pyrolyzate produced from two-stage catalytic pyrolysis of the feed stock fraction separated from Egyptian crude oil under the same last optimum conditions, with pear in mind that Palladium is used as a catalyst in hydrogenation reactions, when we use Pd-nanoparticles as a core in the catalytic pyrolysis, the total yield of unsaturated hydrocarbons will decrease and give yield (59.48 wt. %) total unsaturated hydrocarbons, mainly ethylene (51 wt. %), and propylene (8.48 wt. %), but the presence of palladium on the

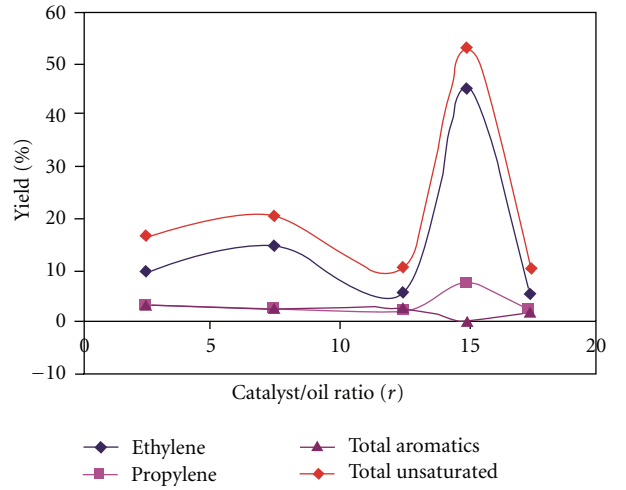

FIGURE 5: Influence of the catalyst/oil ratio on the yield of unsaturated hydrocarbons.

surface increases the rate of hydrogenation, contrary to down falling to the yield of the total unsaturated hydrocarbons to give 48.15 wt. %, mainly ethylene (40.2 wt. %), and propylene (7.95 wt. %), and increases the yield of ethane to reach 33.59 wt. % corresponding to 23.17 wt. % of ethane using Pd-Au core-shell.

7. Conclusion

It was found that the maximum yield of unsaturated hydrocarbons using the first catalyst (CaO) is about 54 wt. %, mainly hexene gives 29 wt. %, 12 wt. % ethylene, 12 wt. % aromatics, and ~1 wt. % propylene at the following conditions: T_1 = 250°C, T_2 = 400°C, τ_1 = 15 min, τ_2 = 3 sec and cat/oil ratio (r) 1 : 25, but by using the gold (Au) nanoparticles supported on the first catalyst, the maximum yield of unsaturated hydrocarbon is about 53 wt. %, mainly 45 wt. % ethylene and 8 wt. % propylene, only without aromatics at the following conditions: T_1 = 200°C, T_2 = 400°C, τ_1 = 10 min, τ_2 = 3 sec, and cat/oil (r) ratio 1 : 15, so Au-nanoparticles seem to be very selective to these reactions.

The Au nanocatalyst with rods shape gives the maximum yield of ethylene (which can be converted easily to ethyl alcohols which is used as E-85 clean fuel) from petroleum residues.

Acknowledgments

The authors would like to thank Professor Yehya Badr (Chairman of National institute of laser research) for financial support; they also thank Professor Ashraf El-Naggar for the support and discussions for the GC-mass spectrometer.

References

[1] I. K. Basily, S. T. El-Shaltawy, and B. S. Mostafa, "The catalytic pyrolysis of the Egyptian bitumen for industrial production raw material," *Journal of Analytical and Applied Pyrolysis*, vol. 76, no. 1-2, pp. 24–31, 2006.

[2] I. K. Basily and K. Thamer, "Pyrolysis products dependence on the nature of heavy hydrocarbon feedstock," *Applied Catalysis*, vol. 73, pp. 125–133, 1991.

[3] I. K. Basily and N. N. Ibraheam, "Two-stage pyrolysis of heavy residues: feedstock versus yield," *Fuel*, vol. 72, no. 2, pp. 161–164, 1993.

[4] M. Itoh, T. Suzuki, Y. Tsujimoto, K. I. Yoshii, Y. Takegami, and Y. Watanabe, "Two-stage pyrolysis of heavy oils. 3. Pyrolysis of tar-sand bitumens. Relation between ethylene yield and structural characteristics of heavy oils," *Fuel*, vol. 62, no. 1, pp. 98–102, 1983.

[5] I. K. Basily, E. Souaya, and N. N. Ibraheem, "Gas-liquid chromatographic determination of the gaseous products of the two-stage pyrolysis of heavy oils," *Microchemical Journal*, vol. 38, no. 3, pp. 283–294, 1988.

[6] I. K. Basily, E. Ahmed, and N. Nashed, "Factors affecting the yields produced from the two-stage pyrolysis of Egyptian bitumen," *Journal of Analytical and Applied Pyrolysis*, vol. 17, no. 2, pp. 153–167, 1990.

[7] I. K. Basily, "Metal-catalyzed two-stage pyrolysis 2. Role of different catalysts in the production and composition of ethylene/propylene-enriched gases," *Journal of Analytical and Applied Pyrolysis*, vol. 32, pp. 213–219, 1995.

[8] I. K. Basily, E. Ahmed, and N. N. Ibraheam, "Upgrading heavy ends into marketable products. New concepts and new catalysts for two-stage catalytic pyrolysis," *Journal of Analytical and Applied Pyrolysis*, vol. 32, pp. 221–232, 1995.

[9] I. Hussain, S. Graham, Z. Wang et al., "Size-controlled synthesis of near-monodisperse gold nanoparticles in the 1–4 nm range using polymeric stabilizers," *Journal of the American Chemical Society*, vol. 127, no. 47, pp. 16398–16399, 2005.

[10] J. H. Chen, J.-N. Lin, Y. M. Kang, W. Y. Yu, C. N. Kuo, and B. Z. Wan, "Preparation of nano-gold in zeolites for CO oxidation: effects of structures and number of ion exchange sites of zeolites," *Applied Catalysis A*, vol. 291, no. 1-2, pp. 162–169, 2005.

[11] J.-N. Lin and B.-Z. Wan, "Effects of preparation conditions on gold/Y-type zeolite for CO oxidation," *Applied Catalysis B*, vol. 41, no. 1-2, pp. 83–95, 2003.

[12] M. Tréguer-Delapierre, J. Majimel, S. Mornet, E. Duguet, and S. Ravaine, "Synthesis of non-spherical gold nanoparticles," *Gold Bulletin*, vol. 41, no. 2, pp. 195–207, 2008.

[13] G. C. Bond, C. Louis, and D. T. Thompson, *Catalysis by Gold*, vol. 6 of *Catalytic Science Series*, 2006.

[14] C. J. Murphy, T. K. Sau, A. M. Gole et al., "Anisotropic metal nanoparticles: synthesis, assembly, and optical applications," *The Journal of Physical Chemistry B*, vol. 109, no. 29, pp. 13857–13870, 2005.

[15] J. Perez-Juste, I. Pastariza-Santos, L. Liz-Marzan, and P. Mulvaney, "Gold nanorods: synthesis, characterization and applications," *Coordination Chemistry Reviews*, vol. 249, no. 17-18, pp. 1870–1901, 2005.

[16] S. Link and M. El-Sayed, "Shape and size dependence of radiative, non-radiative and photothermal properties of gold nanocrystals," *International Reviews in Physical Chemistry*, vol. 19, no. 3, pp. 409–453, 2000.

[17] M. S. Chen and D. W. Goodman, "Structure-activity relationships in supported Au catalysts," *Catalysis Today*, vol. 111, no. 1-2, pp. 22–33, 2006.

[18] R. Narayanan and M. A. El-Sayed, "Shape-dependent catalytic activity of platinum nanoparticles in colloidal solution," *Nano Letters*, vol. 4, no. 7, pp. 1343–1348, 2004.

[19] M. Ahmadpour and N. Mostoufi, "Catalyst wetting efficiency in trickle-bed reactors at high pressure," *Chemical Engineering Science*, vol. 50, no. 15, pp. 2377–2389, 1995.

[20] R. S. Sonawane and M. K. Dongare, "Sol-gel synthesis of Au/TiO_2 thin films for photocatalytic degradation of phenol in sunlight," *Journal of Molecular Catalysis A*, vol. 243, no. 1, pp. 68–76, 2006.

[21] M. Haruta and M. Date, "Advances in the catalysis of Au nanoparticles," *Applied Catalysis A*, vol. 222, no. 1-2, pp. 427–437, 2001.

[22] Y. Lizuka, T. Tode, T. Takao et al., "A kinetic and adsorption study of CO oxidation over unsupported fine gold powder and over gold supported on titanium dioxide," *Journal of Catalysis*, vol. 187, no. 1, pp. 50–58, 1999.

[23] M. M. Schubert, S. Hackenberg, A. C. Van Veen, M. Muhler, R. J. Behm, and V. Plzak, "CO oxidation over supported gold catalysts—"Inert" and "active" support materials and their role for the oxygen supply during reaction," *Journal of Catalysis*, vol. 197, no. 1, pp. 113–122, 2001.

[24] J. Chou, N. R. Franklin, S. H. Beack, T. M. Jaramillo, and E. W. McFarland, "Gas-phase catalysis by micelle derived Au nanoparticles on oxide supports," *Catalysis Letters*, vol. 95, no. 3–5, pp. 107–111, 2004.

[25] S. H. Overbury, L. Ortiz-Soto, H. G. Zhu, B. Lee, S. Dai, and M. D. Amiridis, "Comparison of Au catalysts supported on mesoporous titania and silica: investigation of Au particle size effects and metal-support interactions," *Catalysis Letters*, vol. 95, no. 3-4, pp. 99–106, 2004.

[26] B. Hammer and J. K. Norskov, "Why gold is the noblest of all the metals," *Nature*, vol. 376, no. 6537, pp. 238–240, 1995.

[27] V. Subramanian, E. E. Wolf, and P. V. Kamat, "Catalysis with TiO_2/gold nanocomposites. effect of metal particle size on the fermi level equilibration," *Journal of the American Chemical Society*, vol. 126, no. 15, pp. 4943–4950, 2004.

[28] C. Wang, C. Kan, J. Zhu et al., "Synthesis of high-yield gold nanoplates: fast growth assistant with binary surfactants," *Journal of Nanomaterials*, vol. 2010, Article ID 969030, 2010.

[29] J. P. Deng, C. Wu, C. H. Yang, and C. Y. Mou, "Pyrene-assisted synthesis of size-controlled gold nanoparticles in sodium dodecyl sulfate micelles," *Langmuir*, vol. 21, no. 19, pp. 8947–8951, 2005.

[30] S. Schimpf, M. Lucas, C. Mohr et al., "Supported gold nanoparticles: in-depth catalyst characterization and application in hydrogenation and oxidation reactions," *Catalysis Today*, vol. 72, no. 1-2, pp. 63–78, 2002.

[31] G. Walther, D. J. Mowbray, T. Jiang et al., "Oxidation of CO and H_2 by O_2 and N_2O on Au/TiO_2 catalysts in microreactors," *Journal of Catalysis*, vol. 260, no. 1, pp. 86–92, 2008.

Hindawi Publishing Corporation
Journal of Nanotechnology
Volume 2012, Article ID 568147, 8 pages
doi:10.1155/2012/568147

Research Article

Two-Electron Reaction without Structural Phase Transition in Nanoporous Cathode Material

Tomoyuki Matsuda[1] and Yutaka Moritomo[1,2]

[1] *Graduate School of Pure and Applied Science, University of Tsukuba, Tsukuba, Ibaraki 305-8571, Japan*
[2] *Tsukuba Research Center for Interdisciplinary Materials Science (TIMS), University of Tsukuba, Tsukuba, Ibaraki 305-8571, Japan*

Correspondence should be addressed to Yutaka Moritomo, moritomo@sakura.cc.tsukuba.ac.jp

Received 21 February 2012; Accepted 28 March 2012

Academic Editor: Vaishali R. Shinde

Copyright © 2012 T. Matsuda and Y. Moritomo. This is an open access article distributed under the Creative Commons Attribution License, which permits unrestricted use, distribution, and reproduction in any medium, provided the original work is properly cited.

We investigated the charge/discharge properties, valence states, and structural properties of a nanoporous cathode material $Li_xMn[Fe(CN)_6]_{0.83} \cdot 3.5H_2O$. The film-type electrode of $Li_xMn[Fe(CN)_6]_{0.83} \cdot 3.5H_2O$ exhibited a high charge capacity (= 128 mAh g^{-1}) and a good cyclability (87% of the initial value after 100 cycles) and is one of the promising candidates for Li-ion battery cathode. X-ray absorption spectra near the Fe and Mn K-edges revealed that the charge/discharge process is a two-electron reaction; that is, Mn^{II}–NC–Fe^{II}, Mn^{II}–NC–Fe^{III}, and Mn^{III}–NC–Fe^{III}. We further found that the crystal structure remains cubic throughout the charge/discharge process. The lattice constant slightly increased during the $[Fe^{II}(CN)_6]^{4-}/[Fe^{III}(CN)_6]^{3-}$ oxidization reaction while decreased during the Mn^{II}/Mn^{III} oxidization reaction. The two-electron reaction without structural phase transition is responsible for the high charge capacity and the good cyclability.

1. Introduction

Lithium ion batteries have aided the portable electronics revolution during the past two decades, and they are now being intensively pursued for transportation applications and the efficient storage and utilization of intermittent renewable energies like solar and wind. Therefore, next-generation electrode materials have been intensively explored in order to achieve a highly capacious, safe, environmentally-friendly, and low cost Li-ion secondary battery. Especially, the automotive industry requires low-cost and higher-capacious materials than the conventionally used transition metal oxides, for example, $LiCoO_2$ [1, 2]. $LiFePO_4$ with ordered-olivine structure is one of the most promising candidate cathode materials and is beginning to be applied commercially. The compound has one-dimensional tubes for Li insertion/extraction. Padhi et al. first reported that the charge capacity of $LiFePO_4$ was 100–110 mA h g^{-1} [3]. The Li insertion/extraction reaction in $LiFePO_4$ proceeds via the two-phase process, unless the particle size becomes below 40 nm [4]. In addition, the low electronic conductivity due to the ionic nature of the compound is considered to disturb high-speed charging/discharging. Therefore, other iron-based materials that exhibit reversible Li ion insertion/extraction reaction could be attractive electrode materials.

Prussian blue analogues [5–15], represented as $A_xM[M'(CN)_6]_y \cdot zH_2O$ (A is an alkali metal ion, and M and M' are transition metal ions), have nanoporous three-dimensional network structures. The film type of this series is studied as electrochromic materials [7]. Imanishi et al. firstly reported the charge/discharge properties of the Prussian blue analogues (M = V, Mn, Fe, Co, Ni, Cu, and M' = Fe) [12, 13], and the M = Cu compound exhibited a large capacity (140 mA h g^{-1}) even though its cyclability is very poor. On the other hand, Okubo et al. reported excellent cyclability in the M = Mn and M' = Fe compound even though its capacity is low (57 mA h g^{-1}) [14]. Recently, we realized a good cyclability with a high charge capacity in the film-type electrode of $Li_xMn[Fe(CN)_6]_{0.83} \cdot 3.5H_2O$ [15]. The film-type electrode does not contain a conductive material nor a binder polymer.

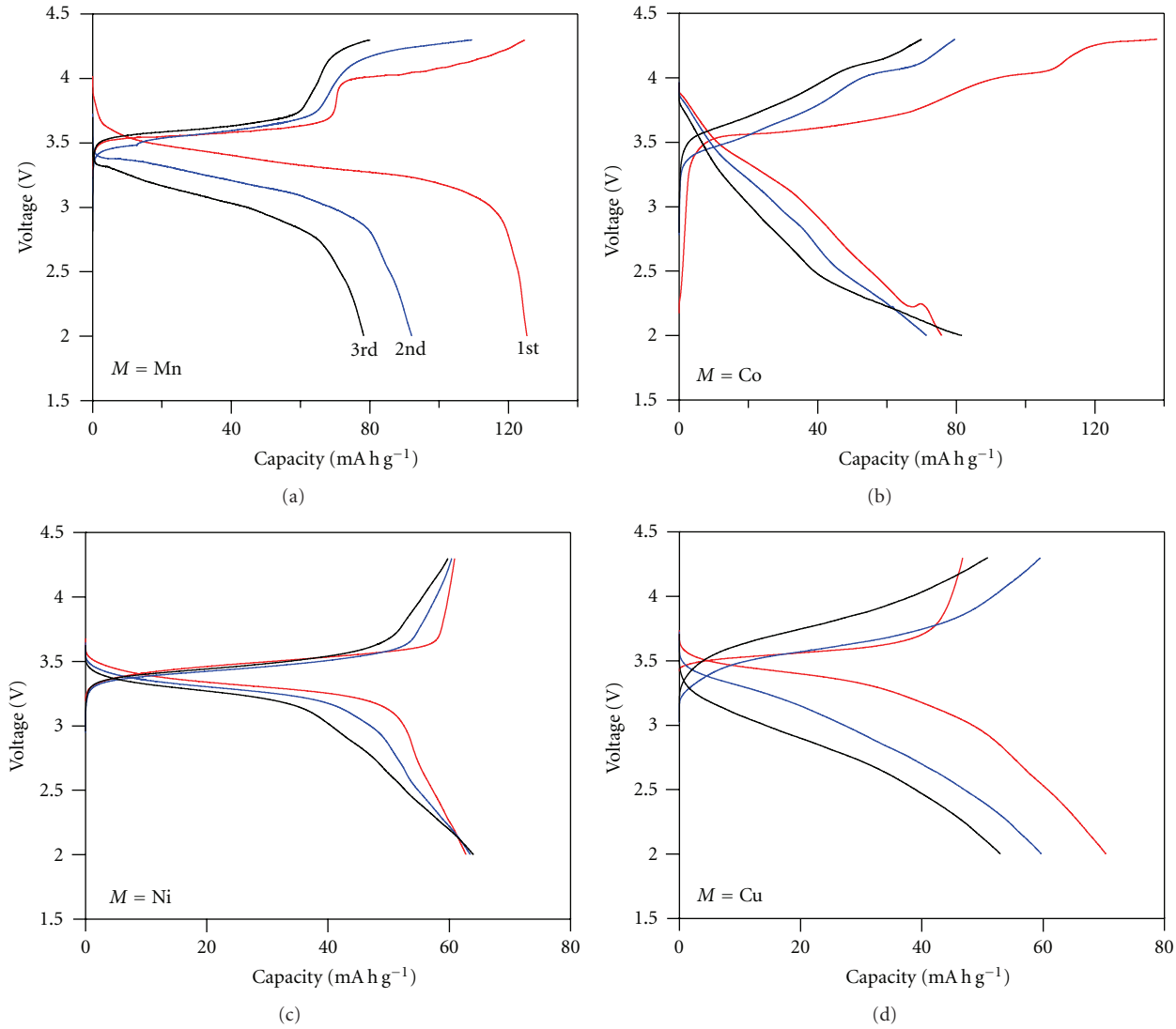

FIGURE 1: Charge/discharge curves of the paste-type electrode of $Na_xM[Fe(CN)_6]$ (M = Mn (a), Co (b), Ni (c), and Cu (d)) against the Li metal at the 1st (red), 2nd (blue), and 3rd (black) cycles.

In this paper, we present charge/discharge properties of the $Na_{4x-2}M[Fe(CN)_6]_x \cdot zH_2O$ (M = Mn, Co, Ni, and Cu) powder samples and a detailed electronic and structural properties of $Li_xMn[Fe(CN)_6]_{0.83} \cdot 3.5H_2O$ during the charge/discharge processes. The data clearly indicates that the two-electron reaction without structural phase transition is responsible for the high charge capacity and the good cyclability observed in $Li_xMn[Fe(CN)_6]_{0.83} \cdot 3.5H_2O$.

2. Experimental Section

2.1. Preparation of the Powder Samples. The powder form of $Na_{4x-2}M[Fe(CN)_6]_x \cdot zH_2O$ (M = Mn, Co, Ni, and Cu) was prepared by precipitation method. The aqueous solutions of NaCl (4 mol L dm^{-3}) and $MCl_2 \cdot zH_2O$ (5 mmol L dm^{-3}) were slowly added dropwise to a stirred solution of NaCl (4 mol L dm^{-3}) and $K_4[Fe(CN)_6]$ (5 mmol L dm^{-3}). The obtained powder precipitates were filtered and washed with water and then dried in air.

2.2. Preparation of the Thin Film. Thin film of $Na_{1.32}Mn[Fe(CN)_6]_{0.83} \cdot 3.5H_2O$ was electrochemically synthesized on an indium tin oxide (ITO) transparent electrode under potentiostatic conditions at −0.50 V versus a standard Ag/AgCl electrode in an aqueous solution containing 1.0 mmol L dm^{-3} $K_3[Fe(CN)_6]$, 1.5 mmol L dm^{-3} $MnCl_2 \cdot 6H_2O$, and 1.0 mol L dm^{-3} NaCl. Before the film growth, the surface of the ITO electrode was purified by electrolysis of water for 3–5 min. The obtained film was transparent with a thickness of around 1 μm. Chemical compositions of the films were determined by the inductively coupled plasma (ICP) method and CHN organic elementary analysis (Perkin-Elmer 2400 CHN Elemental Analyzer). The Li^+ was substituted for Na^+ by performing the

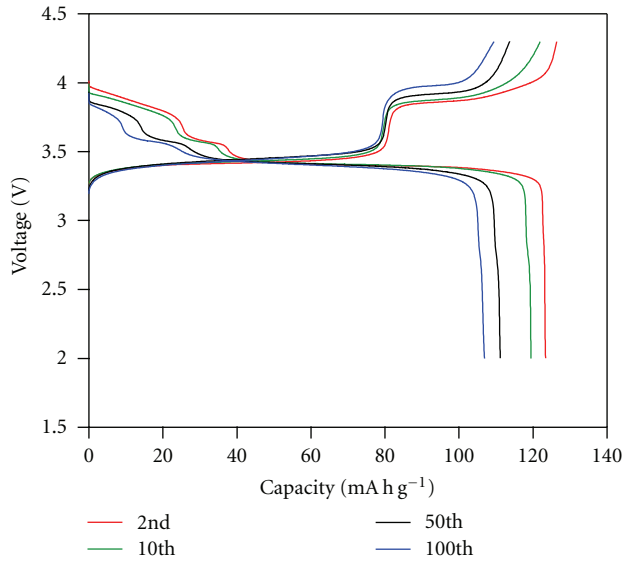

FIGURE 2: Charge/discharge curves of the film-type electrode of $Li_xMn[Fe(CN)_6]_{0.83} \cdot 3.5H_2O$ against the Li metal at the 2nd, 10th, 50th, and 100th cycles at a constant current density of 56 mA g^{-1}.

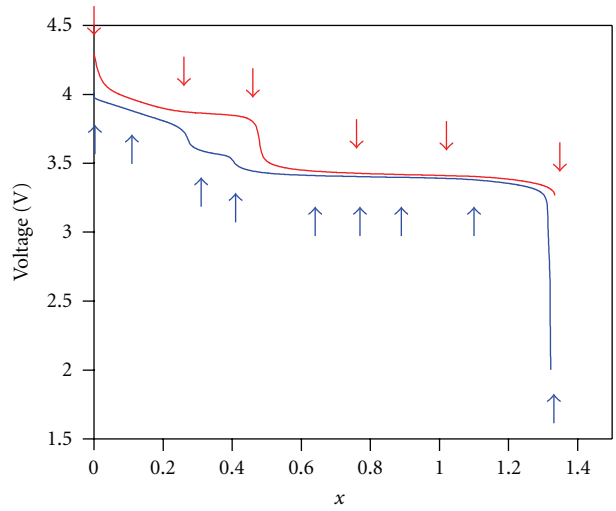

FIGURE 3: Voltage versus composition curves for charge (red) and discharge (blue) process of film-type electrode of $Li_xMn[Fe(CN)_6]_{0.83} \cdot 3.5H_2O$ at the 2nd cycle. The arrows indicate the compositions for the XAS and XRD measurements.

charge/discharge cycles of the thin film against Li. Thus, we obtained thin films of $Li_xMn[Fe(CN)_6]_{0.83} \cdot 3.5H_2O$.

2.3. Electrochemical Measurements. To measure the charge/discharge curves, the powder samples were ground with 20 wt% acetylene black and 5 wt% PTFE into a paste. The paste was coated on a stainless steel mesh and used as the cathode. Hereafter, we call this type of electrode a paste-type electrode. The thin film was used as prepared (film-type electrode). The lithium metal was used as the reference and counter electrode, and the cutoff voltage was from 2.0 to 4.3 V. The electrolyte was ethylene carbonate (EC)/diethyl carbonate (DEC) solution containing 1 mol dm^{-1} $LiClO_4$.

2.4. X-Ray Absorption Measurements. The valence states of the Fe and Mn sites were determined by the *ex situ* X-ray absorption spectra (XAS) around the Mn and Fe K-edge. The XAS measurements were conducted at the beamline 7C of KEK-PF. The XAS spectra were recorded by a Lytle detector in a fluorescent yield mode with an Si(111) double-crystal monochromator at 300 K. The background subtraction and normalization were done using ATHENA program [16].

2.5. Powder X-Ray Diffraction Measurements. The *ex situ* powder X-ray diffraction (XRD) patterns were measured at the beamline 8A of KEK-PF equipped with an imaging plate detector. The charged/discharged samples were washed with

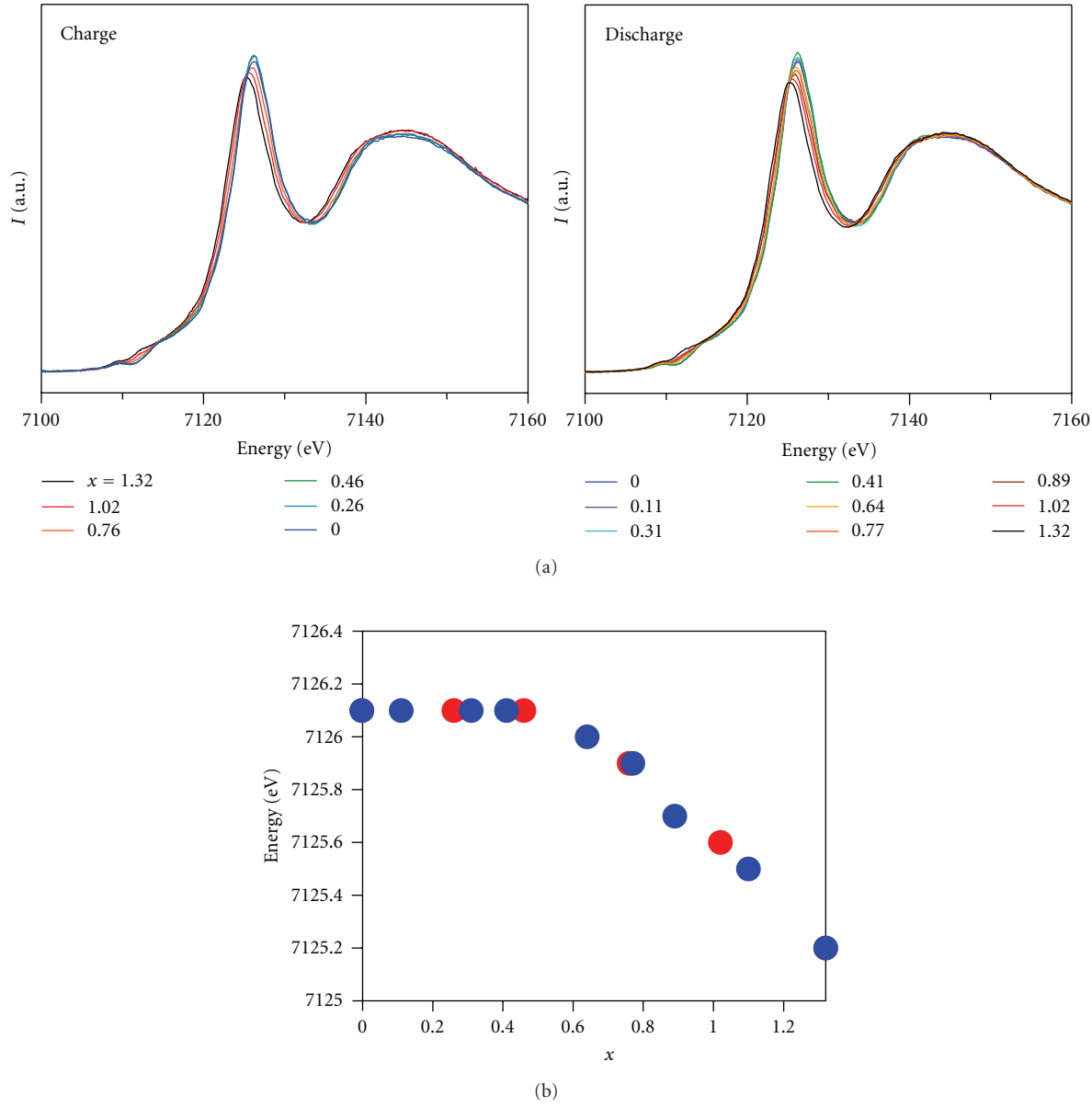

FIGURE 4: (a) Fe K-edge XAS spectra for the charge (left) and discharge (right) processes of film-type electrode of $Li_xMn[Fe(CN)_6]_{0.83} \cdot 3.5H_2O$. (b) Peak energy ($E(x)$) against x for the charge (red) and discharge (blue) processes.

DEC and were carefully removed from the ITO glasses. The obtained powders were sealed in 300 μm glass capillaries. XRD patterns were measured at 300 K and the exposure time was 5 min. Wavelength of the X-ray was 0.77516 Å. The lattice constants of each compounds were refined by the RIETAN-FP program [17].

3. Results

3.1. Charge/Discharge Property of the Paste-Type Electrode. Figure 1 shows the charge-discharge curves for the paste-type electrodes of $Na_{4x-2}M[Fe(CN)_6]_x \cdot zH_2O$ (M = Mn, Co, Ni, and Cu). The charge capacity of the 1st cycle for M = Mn, Co, Ni, and Cu was 125, 138, 61, 47 mA h g^{-1}, respectively, while the discharge capacity of the 1st cycle for M = Mn, Co, Ni, and Cu was 125, 76, 63, and 71 mA h g^{-1}, respectively. The charge/discharge capacity of M = Mn is nearly twice as large as the M = Ni and Cu. This suggests that the two-electron reaction occurs in M = Mn, while the one-electron reaction occurs in M = Ni, and Cu. The charge capacity of M = Co is also twice as large as M = Ni and Cu, while discharge capacity is almost the half of the charge capacity. This suggests that M = Co shows irreversible two-electron reaction. Thus observed behaviors are almost same as the reported $M[Fe(CN)_6]_{2/3} \cdot zH_2O$ type compounds [12, 13]. The cyclability was far from excellent for every

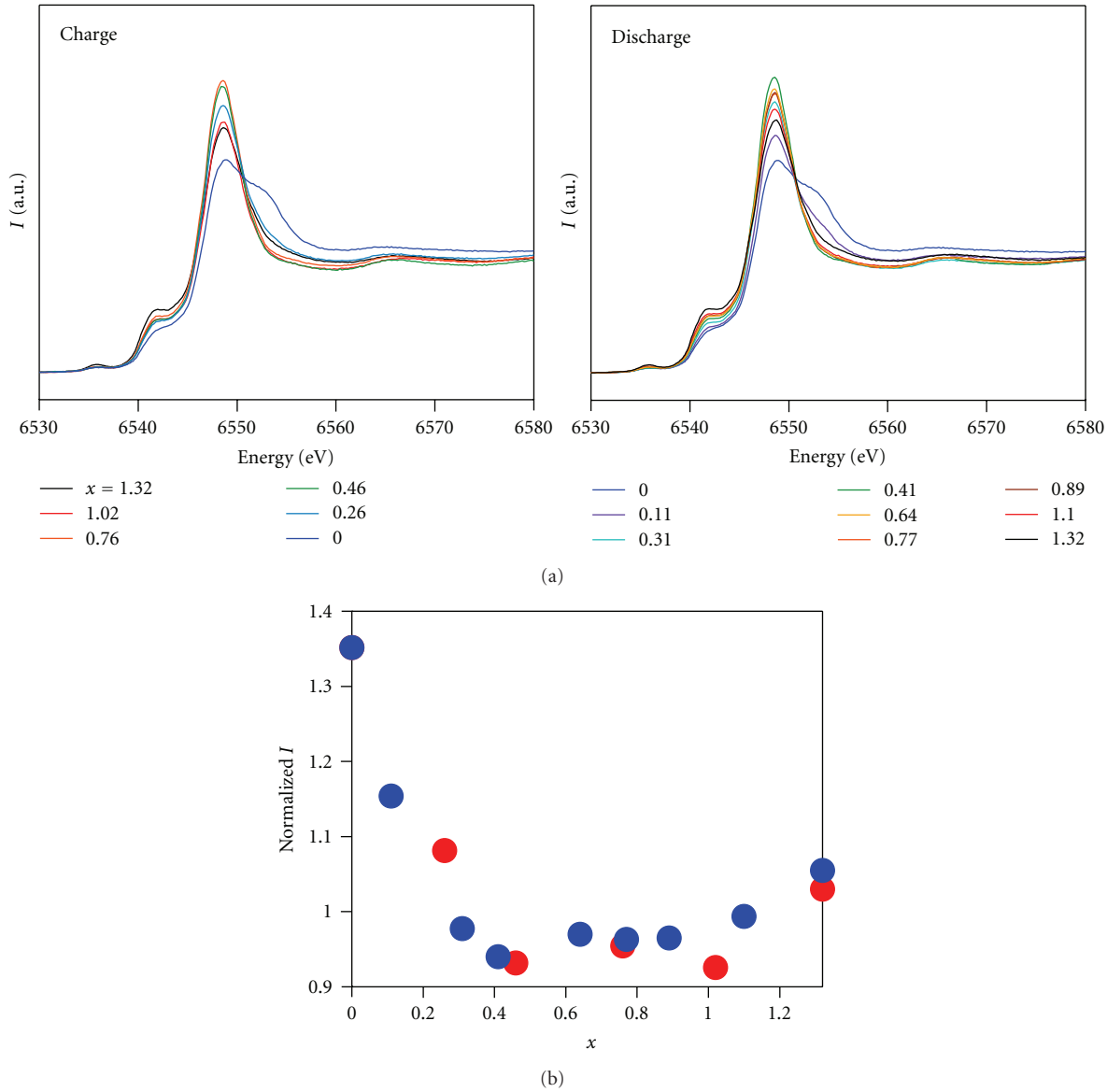

FIGURE 5: (a) Mn K-edge XAS spectra for the charge (left) and discharge (right) processes of film-type electrode of $Li_xMn[Fe(CN)_6]_{0.83} \cdot 3.5H_2O$. (b) Normalized intensity ($I(x)$) against x for the charge (red) and discharge (blue) processes.

compound. In other words, the paste-type electrodes of $Na_{4x-2}M[Fe(CN)_6]_x \cdot zH_2O$ powders are not good candidates for the Li-ion battery cathodes.

3.2. Charge/Discharge Property of the Film-Type Electrode. Figure 2 shows the charge/discharge curves of the film-type electrode of $Li_xMn[Fe(CN)_6]_{0.83} \cdot 3.5H_2O$ at the 2nd, 10th, 50th, and 100th cycles. In the charge process, electrochemical reaction takes place at 3.4 and 3.9 V, and the charge capacity reaches 128 mA h g^{-1}. The 3.4 and 3.9 plateaus correspond to the $[Fe^{II}(CN)_6]^{4-}/[Fe^{III}(CN)_6]^{3-}$ and Mn^{2+}/Mn^{3+} reactions, respectively (*vide infra*). In the discharge process, electrochemical reaction takes place at 3.9, 3.6, and 3.4 V. After 100 charge/discharge cycles, the charge capacity remains high (87% of the initial value). We emphasize that the thin-film electrode shows a prominent color change from brown to colorless in the discharge process. The color charge can be used as a battery power indicator without electricity consumption. We call such a battery as color battery.

3.3. Variation of the Valence States. Figure 3 shows the charge/discharge curve of the film-type electrode of $Li_xMn[Fe(CN)_6]_{0.83} \cdot 3.5H_2O$ at the 2nd cycle. We electrochemically controlled the Li ion concentration (x) as indicated by the arrows. Figure 4(a) shows the Fe K-edge XAS spectra of charge/discharge process. The absorption peak energies (E) in the Fe K-edge spectra show clear blue shift with decrease in x (Figure 4(b)). The blue shift is ascribed to the oxidization of Fe (low-spin Fe^{II} → low-spin Fe^{III})

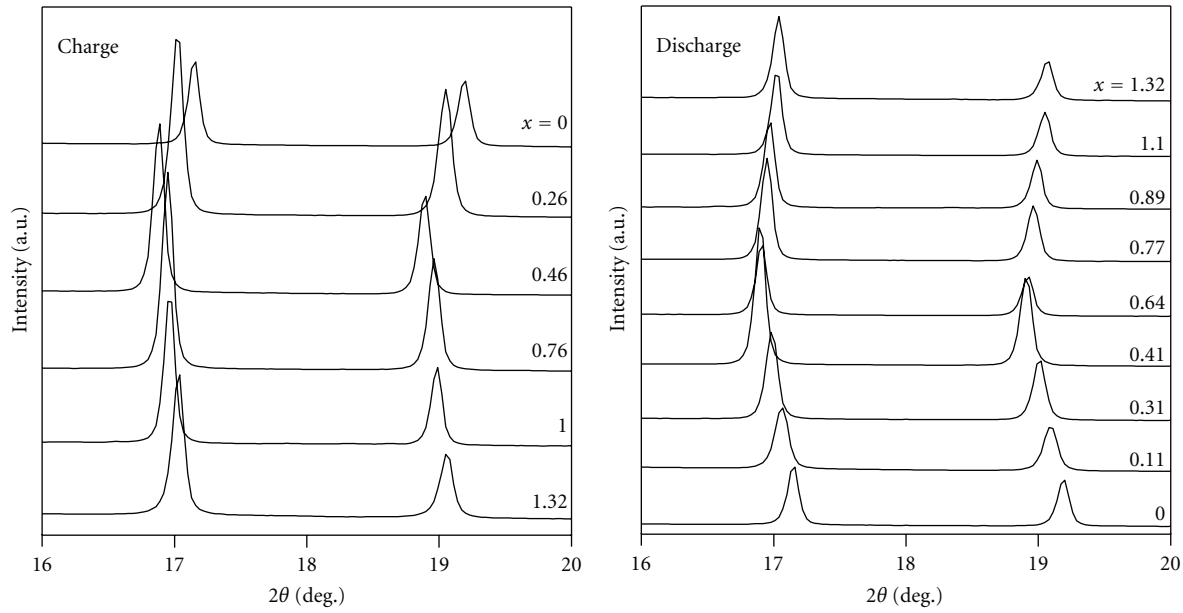

Figure 6: XRD patterns for the charge (left) and discharge (right) processes of film-type electrode of $Li_xMn[Fe(CN)_6]_{0.83} \cdot 3.5H_2O$.

[10, 11]. We emphasize that the blue shift saturates below $x = 0.46$ (0.41) in the charge (discharge) process. Figure 5(a) shows the Mn K-edge XAS spectra of charge/discharge process. The shoulder peak appeared around 6553 eV in the small-x region. This new peak is ascribed to the oxidization of Mn (high spin $Mn^{II} \rightarrow$ high-spin Mn^{III}) [10]. These data indicated that the oxidization of Fe takes place in the large-x region, while the oxidization of Mn takes place in the small-x region.

3.4. Variation of the Structure. Figure 6 shows the magnified XRD patterns during charge/discharge process. The lattice structure remains the face-centered cubic (Fm-$3m$; $Z = 4$) throughout the charge/discharge process. In the charge process, the reflection shifts to the lower-angle side above $x = 0.76$ while shifts to the lower-angle side below $x = 0.46$. In the discharge process, the reflection shifts to the lower-angle side below $x = 0.41$ while shifts to the higher-angle side above $x = 0.64$.

4. Discussion

Now, let us evaluate the molar ratios, that is, $Fe^{III}/(Fe^{II}+Fe^{III})$ and $Mn^{III}/(Mn^{II}+Mn^{III})$, against x based on the XAS spectra. Figure 4(b) shows peak energies ($E(x)$) in the Fe K-edge spectra against x. We note that the $E(x)$ is nearly constant below $x \sim 0.5$, suggesting that all the Fe sites are trivalent in this region. We ascribed the $E(x)$ values at $x = 1.32$ and at $x = 0.0$ is to the Fe^{II} and Fe^{III} state. With assuming a linear relation between $E(x)$ and the molar ratio, we obtained the formula $Fe^{III}/(Fe^{II} + Fe^{III}) = (E(x) - E(1.32))/(E(0.0) - E(1.32))$. Figure 5(b) shows the normalized intensity ($I(x)$) at 6553.2 eV, which is ascribed to the Mn^{III}, in the Mn K-edge spectra against x. We note that the $I(x)$ is nearly constant above $x \sim 0.5$, suggesting that all the Mn sites remains divalent in this region. On the basis of the chemical formula and charge neutrality, we assumed the molar ratio of Mn^{III} at $x = 0.0$ is 0.49. With assuming a linear relation between $I(x)$ and the molar ratio, we obtained the formula $Mn^{III}/(Mn^{II} + Mn^{III}) = 0.49 \times (I(x) - I(0.76))/(I(0.0) - I(0.76))$.

Figures 7(a) and 7(b) show the molar ratios of the Fe^{III} and Mn^{III} against x, respectively. These data clearly indicate that the charge/discharge process of the film-type electrode consists of the two reactions, that is, Mn^{II}/Mn^{III} and Fe^{II}/Fe^{III} reactions. The Mn^{II}/Mn^{III} reaction takes place in the small-x region ($x < 0.49$: indicated by vertical broken line in Figure 7), while the Fe^{II}/Fe^{III} reaction takes place in the large-x region ($x > 0.49$). The first and second plateaus in the charge process (see Figure 3) are ascribed to the oxidization of Mn^{II} and $[Fe^{II}(CN)_6]^{4-}$, respectively. On the contrary, the first, second, and third plateaus in the discharge process are due to the reduction of Mn^{III}, Mn^{III}, and $[Fe^{III}(CN)_6]^{3-}$, respectively.

Figure 7(c) shows the lattice constant against x. The lattice constants were refined by the Rietveld analyses. In the Mn^{II}/Mn^{III} redox region, the lattice constant increases with x. The increase is ascribed to the larger ionic radius of Mn^{II}. In the Fe^{II}/Fe^{III} region, the lattice constant decreases with x. The decrease is ascribed to the smaller size of $[Fe^{II}(CN)_6]^{4-}$ as compared with that of $[Fe^{III}(CN)_6]^{3-}$. Figure 8 shows the schematic illustration [18] of the crystal structure during the whole charge/discharge process.

5. Conclusions

In summary, we investigated the charge/discharge properties, electronic states, and structural properties of the film-type electrode of $Li_xMn[Fe(CN)_6]_{0.83} \cdot 3.5H_2O$. The film-type

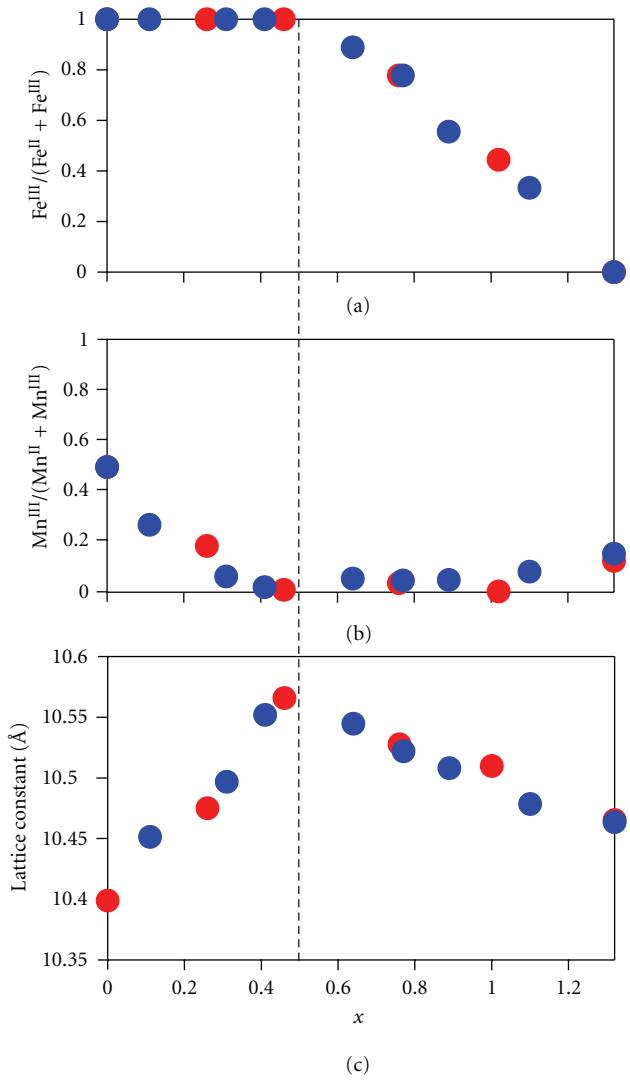

FIGURE 7: (a) Molar ratios of the Fe^{III}, (b) molar ratios of the Mn^{III} (b), and (c) lattice constants for the charge (red) and discharge (blue) processes of $Li_xMn[Fe(CN)_6]_{0.83} \cdot 3.5H_2O$.

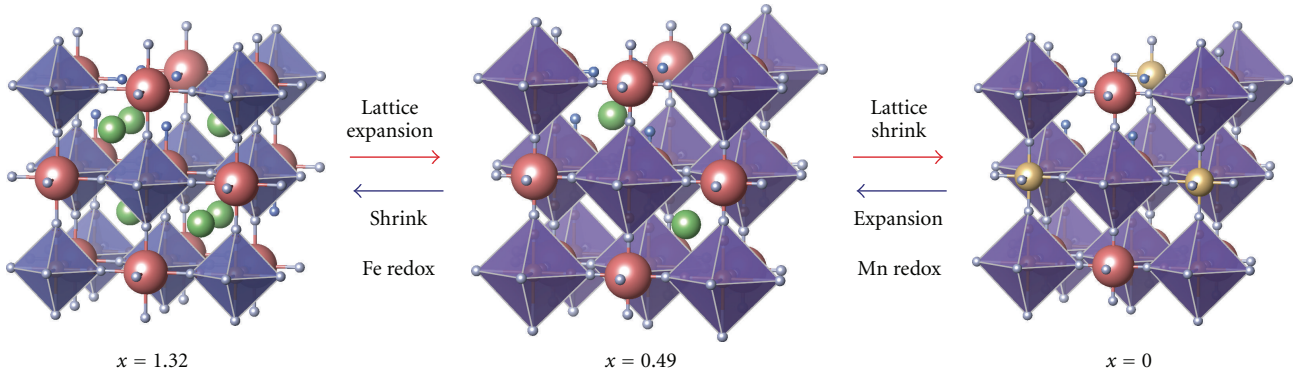

FIGURE 8: Schematic illustrations of crystal structures of $Li_xMn[Fe(CN)_6]_{0.83} \cdot 3.5H_2O$ thin film. Blue and purple polyhedra represent $[Fe^{II}(CN)_6]$, and $[Fe^{II}(CN)_6]$ units, respectively, and red and yellow spheres represent Mn^{II} and Mn^{III}, respectively. The green, white, and blue spheres are Li, N, and O, respectively.

electrode shows a large capacity and a good cyclability and is a candidate for Li-ion battery cathode. The XAS clearly indicated the two-electron redox process of Fe and Mn. Nevertheless, the crystal structure remains cubic in the whole charge/discharge process. We ascribed the good charge/discharge property to the two-electron process without structural phase transition.

Acknowledgments

This paper was supported by a Grant-in-Aid (21244052) for Scientific Research from the Ministry of Education, Culture, Sports, Science and Technology. Elementary analysis was performed at Chemical Analysis Division, Research Facility Center for Science and Engineering, University of Tsukuba. The X-ray powder diffraction and X-ray absorption experiments were performed under the approval of the Photon Factory Program Advisory Committee (Proposal no. 2010G502 and 2011G501).

References

[1] M. Armand and J. M. Tarascon, "Building better batteries," *Nature*, vol. 451, no. 7179, pp. 652–657, 2008.

[2] H. Nishide and K. Oyaizu, "Toward flexible batteries," *Science*, vol. 319, no. 5864, pp. 737–738, 2008.

[3] A. K. Padhi, K. S. Nanjundaswamy, and J. B. Goodenough, "Phospho-olivines as positive-electrode materials for rechargeable lithium batteries," *Journal of the Electrochemical Society*, vol. 144, no. 4, pp. 1188–1194, 1997.

[4] P. Gibot, M. Casas-Cabanas, L. Laffont et al., "Room-temperature single-phase Liinsertion/extraction in nanoscale Li_xFePO_4," *Nature Materials*, vol. 7, no. 9, pp. 741–747, 2008.

[5] M. Verdaguer, A. Bleuzen, V. Marvaud et al., "Molecules to build solids: high T_c molecule-based magnets by design and recent revival of cyano complexes chemistry," *Coordination Chemistry Reviews*, vol. 190-192, pp. 1023–1047, 1999.

[6] A. Ludi and H. U. Güdel, "Structural chemistry of polynuclear transition metal cyanides," *Structure and Bonding*, vol. 14, pp. 1–21, 1973.

[7] K. Itaya, T. Ataka, and S. Toshima, "Spectroelectrochemistry and electrochemical preparation method of Prussian Blue modified electrodes," *Journal of the American Chemical Society*, vol. 104, no. 18, pp. 4767–4772, 1982.

[8] T. Matsuda, J. Kim, and Y. Moritomo, "Symmetry switch of cobalt ferrocyanide framework by alkaline cation exchange," *Journal of the American Chemical Society*, vol. 132, no. 35, pp. 12206–12207, 2010.

[9] Y. Moritomo, Y. Kurihara, T. Matsuda, and J. E. Kim, "Structural phase diagram of Mn–Fe cyanide against cation concentration," *Journal of the Physical Society of Japan*, vol. 80, no. 10, Article ID 103601, 2011.

[10] T. Yokoyama, H. Tokoro, S. I. Ohkoshi, K. Hashimoto, K. Okamoto, and T. Ohta, "Photoinduced phase transition of $RbMnFe(CN)_6$ studied by x-ray-absorption fine structure spectroscopy," *Physical Review B*, vol. 66, no. 18, Article ID 184111, 2002.

[11] A. Omura, Y. Kurihara, T. Matsuda, H. Tanida, T. Uruga, and Y. Moritomo, "Cation extraction process in bilayer cyanide film as investigated by depth-resolved X-ray absorption spectroscopy," *Japanese Journal of Applied Physics*, vol. 50, no. 12, Article ID 125802, 2011.

[12] N. Imanishi, T. Morikawa, J. Kondo et al., "Lithium intercalation behavior into iron cyanide complex as positive electrode of lithium secondary battery," *Journal of Power Sources*, vol. 79, no. 2, pp. 215–219, 1999.

[13] N. Imanishi, T. Morikawa, J. Kondo et al., "Lithium intercalation behavior of iron cyanometallates," *Journal of Power Sources*, vol. 81-82, pp. 530–534, 1999.

[14] M. Okubo, D. Asakura, Y. Mizuno et al., "Switching redox-active sites by valence tautomerism in prussian blue analogues $A_xMn_y[Fe(CN)_6] \cdot nH_2O$ (A: K, Rb): Robust frameworks for reversible Li storage," *Journal of Physical Chemistry Letters*, vol. 1, no. 14, pp. 2063–2071, 2010.

[15] T. Matsuda and Y. Moritomo, "Thin film electrode of Prussian blue analogue for Li-ion battery," *Applied Physics Express*, vol. 4, no. 4, Article ID 047101, 2011.

[16] B. Ravel and M. Newville, "ATHENA, ARTEMIS, HEPHAESTUS: Data analysis for X-ray absorption spectroscopy using IFEFFIT," *Journal of Synchrotron Radiation*, vol. 12, no. 4, pp. 537–541, 2005.

[17] F. Izumi and K. Momma, "Three-dimensional visualization in powder diffraction," *Solid State Phenomena*, vol. 130, pp. 15–20, 2007.

[18] K. Momma and F. Izumi, "VESTA 3 for three-dimensional visualization of crystal, volumetric and morphology data," *Journal of Applied Crystallography*, vol. 44, no. 6, pp. 1272–1276, 2011.